Effect of stress field and mechanical deformation on permeability and fracture self-sealing: Progress Report on the Stress Path Permeameter experiment conducted on Callovo-Oxfordian Claystone

Minerals and Waste Programme
Commissioned Report CR/10/151

Effect of stress field and mechanical deformation on permeability and fracture self-sealing: Progress Report on the Stress Path Permeameter experiment conducted on Callovo-Oxfordian Claystone

R.J. Cuss and J.F. Harrington

Keyworth, Nottingham   British Geological Survey 2010

BRITISH GEOLOGICAL SURVEY

The full range of our publications is available from BGS shops at Nottingham, Edinburgh, London and Cardiff (Welsh publications only) see contact details below or shop online at www.geologyshop.com

The London Information Office also maintains a reference collection of BGS publications, including maps, for consultation.

We publish an annual catalogue of our maps and other publications; this catalogue is available online or from any of the BGS shops.

The British Geological Survey carries out the geological survey of Great Britain and Northern Ireland (the latter as an agency service for the government of Northern Ireland), and of the surrounding continental shelf, as well as basic research projects. It also undertakes programmes of technical aid in geology in developing countries.

The British Geological Survey is a component body of the Natural Environment Research Council.

British Geological Survey offices

BGS Central Enquiries Desk

Tel 0115 936 3143   Fax 0115 936 3276
email enquires@bgs.ac.uk

Kingsley Dunham Centre, Keyworth, Nottingham NG12 5GG

Tel 0115 936 3241   Fax 0115 936 3488
email sales@bgs.ac.uk

Murchison House, West Mains Road, Edinburgh EH9 3LA

Tel 0131 667 1000   Fax 0131 668 2683
email scotsales@bgs.ac.uk

London Information Office at the Natural History Museum (Earth Galleries), Exhibition Road, South Kensington, London SW7 2DE

Tel 020 7589 4090   Fax 020 7584 8270
Tel 020 7942 5344/45   email bgslondon@bgs.ac.uk

Columbus House, Greenmeadow Springs, Tongwynlais, Cardiff CF15 7NE

Tel 029 2052 1962   Fax 029 2052 1963

Forde House, Park Five Business Centre, Harrier Way, Sowton EX2 7HU

Tel 01392 445271   Fax 01392 445371

Maclean Building, Crowmarsh Gifford, Wallingford OX10 8BB

Tel 01491 838800   Fax 01491 692345

Geological Survey of Northern Ireland, Colby House, Stranmillis Court, Belfast BT9 5BF

Tel 028 9038 8462   Fax 028 9038 8461

www.bgs.ac.uk/gsni/

Parent Body

Natural Environment Research Council, Polaris House, North Star Avenue, Swindon SN2 1EU

Tel 01793 411500   Fax 01793 411501
www.nerc.ac.uk

Website www.bgs.ac.uk
Shop online at www.geologyshop.com

Foreword

This report is the product of a study by the British Geological Survey (BGS) undertaken on behalf of the French radioactive waste management company Agence Nationale pour la Gestion des Déchets Radioactifs (Andra) and the European Union 7th Framework Euratom Programme under the auspices of the Fate of repository Gases (FORGE) project, to examine the effect of the stress path on the hydraulic and gas transport properties of the Callovo-Oxfordian claystone.

Acknowledgements

Contents

FIGURES

TABLES

Executive summary

This report describes in detail the stress-path permeameter (SPP) apparatus and the first test conducted on Callovo-Oxfordian (CoX) claystone from the Bure underground research laboratory (URL) in France. Funding for this study has been provided by the French radioactive waste management operator, Andra, the European Union (FORGE Project) and the British Geological Survey through its well-founded laboratory programme and the Geosphere Containment project (part of the BGS core strategic programme).

The results from the first test conducted using the SPP show that the CoX has a very pronounced time-dependent component of deformation. This has implications for the following tests conducted on CoX as part of the FORGE project, but also has implications when comparing tests on CoX that have been deformed at a much faster rate.

Test SPP_CoX-1 was conducted with water as a test permeant at constant pore pressure along a pre-defined stress-path. Volumetric deformation was observed during 16 steps along the stress path, with considerable time-dependent deformation and anisotropy seen in radial strain. The sixteenth stage saw the sample fail through the formation of a fracture after the sample had experienced constant stress conditions for 5.5 days; this emphasises the observed time dependent deformation.

Test SPP-CoX-1 will be used to determine the stress-path steps of test SPP-CoX-2. This much more detailed test will follow 5 or 6 steps up to ultimate failure and will include a full hydraulic test, a gas injection test to determine the gas entry pressure, and constant pore-pressure flow tests to examine the changes in permeability along the stress-path. At all times throughout the test radial and axial deformation will be monitored.

1 Introduction

The objective of the experimental programme is to examine the impact of changing effective stress (e.g. caused by the construction of a disposal/storage facility) and to investigate its affects on the sealing characteristics of the Callovo-Oxfordian (CoX) claystone. As such, there is a need to understand the roles of the stress tensor, the stress path and associated mechanical deformation in determining permeability changes affecting the sealing efficiency of the claystone. Under certain stress conditions, mudrock deformation will result in dilation (net volume increase) or contraction (net volume decrease). The boundary between these conditions is referred to as the dilatancy boundary and this plots as a point in the mean stress (p) versus deviatoric stress (q) space, or a line when specific volume (v) is used as a third axis. Critical state mechanics shows that complex deformation can be described by a series of yield surfaces in the $p' - q' - v$ parametric space. Calibration of this model can be undertaken by taking samples of mudrock along predefined stress paths extending to the yield surfaces while measuring the resulting changes in permeability (both aqueous and gaseous). The main output of the research will be to enhance process understating in Engineering Disturbed Zone (EDZ) mudrock environments, through the critical examination and subsequent validity of key geomechanical relationships applied to mudrock deformation and its role in the temporal evolution of permeability during the operational and post closure repository phases.

The primary purpose of this experimental study is to provide quantitative data examining the mechanisms governing gas migration and the evolution of permeability during deformation. The primary objectives of this experimental study are to measure the evolution of permeability (both hydraulic and gas) of the Callovo-Oxfordian claystone subject to complex changes in stress and porewater pressure. If time permits, each stress path will be conducted twice; once with water and once with gas as the permeant, in order to gain insight into the fundamental processes governing fluid flow in the Callovo-Oxfordian Clay along complex stress paths.

1.1 DEFORMATION AND CRITICAL STATE CONCEPTS

Roscoe et al. (1958), proposed the critical state theory of soils, which provides a unified model of behaviour where stress states and volume states are interrelated. Gerogiannopoulos & Brown later modified this theory in 1978, to account for the brittle or work-softening behaviour of rocks. Shah (1997) also showed that further modification is required to the classical critical state model to account for the tensile strength of rocks, as soils are assumed to have zero tensile strength.

The *state* of shale subject to a simple stress field is defined by its position in the effective stress (p') – differential stress (q') – void ratio (v) parametric space. A change in state can be represented as a *path* within the $p' - q' - v$ space. The projection of this change in the $p' - q'$ space is referred to as the *stress path*. The deformation path can be used to describe fully the deformation history of the rock and can be used to infer certain aspects of the deformation, such as whether it is drained or undrained, etc. Thus a complex deformation history can be represented and described by critical state theory.

A model is proposed where an isotropic soil yields, i.e. passes from purely elastic to elastoplastic behaviour, at a critical specific volume ($v_c = 1 + e_c$). Yielding or shear slipping is considered to occur as a combination of effective stress ($\sigma'_1, \sigma'_2, \sigma'_3$) and specific volume ($v_c$) coinciding with a state boundary surface. Experimentation has shown that when sheared, a deforming rock will tend towards criticality, a state where large shear distortions will occur without any further changes in p', q', or v (Roscoe & Burland, 1968a; Schofield & Wroth, 1968). The critical state line (CSL) is the locus of all possible critical states in the $p' - q' - v$ parametric space. Figure 1-1 shows a soil yield surface, which can be split into three distinct surfaces: the tension, Hvorslev,

and Roscoe surfaces. The normal consolidation (NCL) and critical state (CSL) lines bound these surfaces, which are geometrically and, to a degree, physically equivalent to a Mohr-Coulomb type failure surface for porous rocks (Jones *et al.*, 1987; Loe *et al.*, 1992).
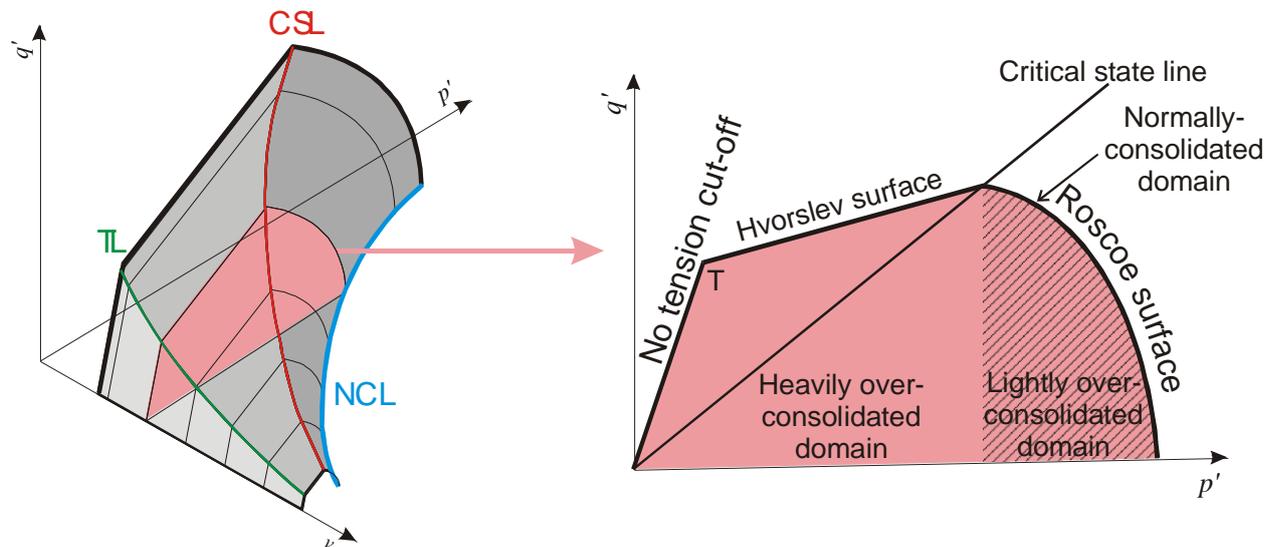
Figure 1-1 The critical state model of soil mechanics, showing the relationship of the tension line (TL), normal consolidation line (NCL) and critical state line (CSL). These lines bound the Hvorslev and Roscoe surfaces in the p' - q' space.

During consolidation under isotropic stress the volume change path will move along the NCL, which is in the plane of zero deviatoric stress (i.e. when stress in all directions is equal). The volumetric strain during consolidation is considered to have elastic (recoverable) and plastic (non-recoverable) components (Scholfied & Wroth, 1968). Figure 1-2b-d shows the paths a material would take in drained (reducing volume path $C{\rightarrow}D$) and undrained (constant volume path $C{\rightarrow}U$) tests. Yield occurs at U_1, D_1, U_2, D_2, U_3, and D_3; in the p' - q' - v space this line represents the CSL. On unloading, deformed sediments will only recover the elastic component of deformation; plastic deformation by definition is non-recoverable. The path then follows the rebound-reconsolidation line (RRL), also known as the swelling line.

1.1.1 Critical state theory and real sediments

There are many examples within the literature of studies on soils and clays that demonstrate the validity of critical state theory and the use of the Cam-clay derived models; including: Adams & Wulfsohn (1997), Cotecchia & Chandler (2000), Diaz-Rodriguez *et al.* (1992), Kirby (1994) Kirby & O'Sullivan (1997), Maâtouk *et al.* (1995), Mitchell (1970), Petley (1999), Tavenas & Leroueil (1977), and Wheeler & Sivakumar (1995). Kirby & O'Sullivan (1997) clearly show how successfully the modified Cam-clay critical state model, with only five material property parameters (M, λ, k, E and η[1]), reproduces non-linear soil deformation behaviour in four dimensions.

The simplistic model of critical state theory is complicated in rocks by features that are generally absent in soils. The concepts of, and relationships between, consolidation and shear are quantitatively valid for clays, fine carbonates, and sands where grain size and angularity do not cause dilatation during shear. For coarse angular grained clastic sediments the critical state concept must be modified to incorporate hardening associated with dilatant shear. Pore volume

---

[1] E is the elastic modulus and η is the Poisson's ratio of the soil

increase is minimal if high porosities are maintained, and as structure becomes more densely packed the dilatation effects become more pronounced. Yield surface form is unaltered, although deformation paths for dilatant materials will be more complex. Shear deformation is complicated at low stresses by elastic stiffness created by intergranular bonding. Studies show a consistent deformation style irrespective of sediment type and strength (Jones, 1994; Vaughan, 1985). Chalk shows a marked behaviour change with increased stress that is more complex than the ideal critical state behaviour; similar features have been observed in bonded mudrocks, carbonates, and sand (Jones, 1994).
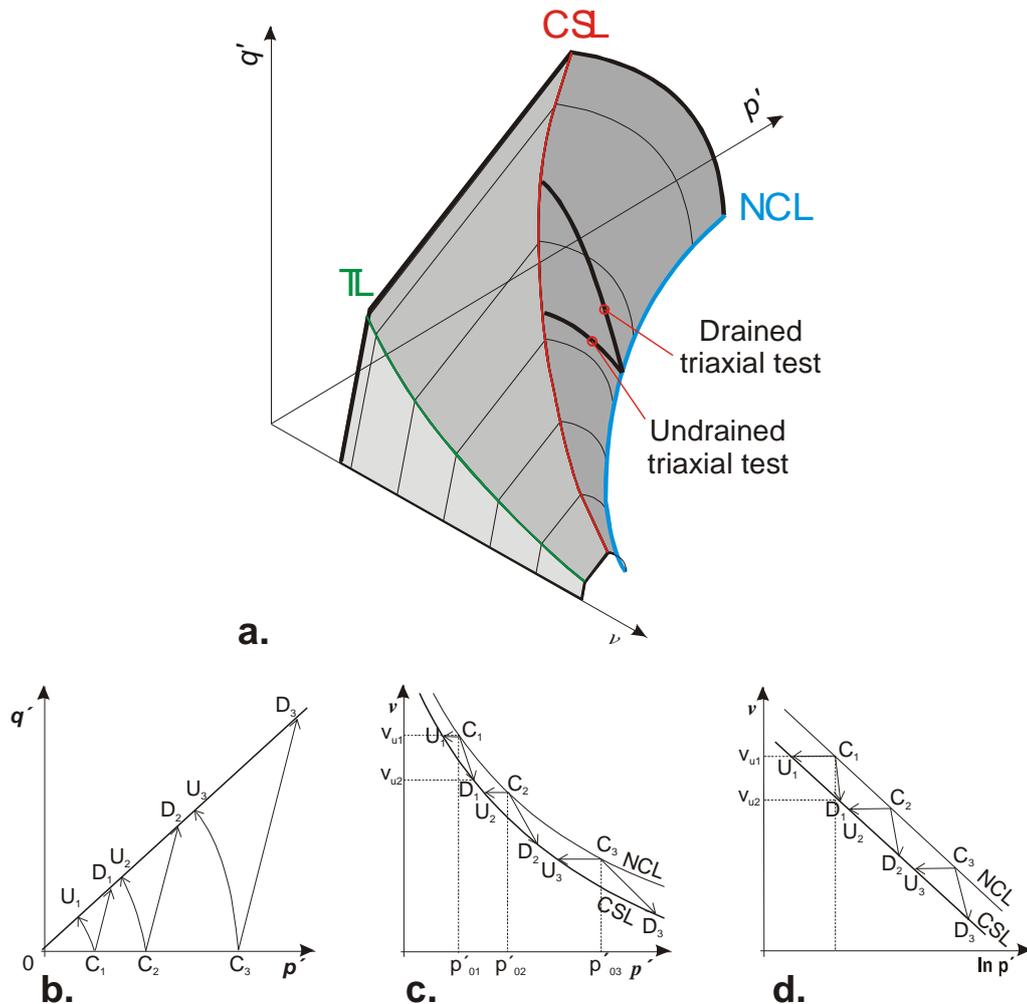
Figure 1-2 The critical state model of soil mechanics in detail. a) The state boundary surface for a particulate sediment (after Atkinson & Bransby, 1978). b-d) p' - q' - v plots of triaxial test results for drained (D) and undrained (U) tests. The stress path for all tests tends towards the critical state line where critical state deformation continues.

At low consolidation stresses, mudstones and sandstones reach the state boundary in an intact bonded condition. Stresses beyond the state boundary can be supported until interception of the peak strength envelope occurs resulting in shear failure. A stress drop is experienced from peak strength to residual strength, as the newly formed shear fracture can no longer support loads above the state boundary. These observations have been shown experimentally in sandstones and mudrocks (Leddra et al., 1993; Leddra et al., 1992; Petley et al., 1992).

What occurs at intermediate and high consolidation stresses is difficult to observe in many rock types as pervasive disaggregation renders test material an incohesive powder. Dissagregation

means materials cannot support stresses above the CSL. At the critical state, shear deformation is pervasive and accompanied by grain sliding and rotation.

The critical state concept and yield surface provide a powerful and effective framework in which all aspects of porous sediment deformation and evolution can be described and interrelated. Complex burial and stress-porosity histories can be described using this concept.

1.1.2 Modification of the critical state model

The critical state model described above, incorporating Hvorslev and Roscoe surfaces, has been shown to inadequately model certain geomaterials, especially in the Hvorslev region (Byerlee, 1967; Cuss, 1999; Hudson and Harrison, 1997; Maltman, 1994a; Ohnaka, 1973; Schofield, 1998; Wong et al., 1997). This is primarily due to the complications introduced by lithification and general rock-forming processes. Some researchers have chosen to replace the state boundary surfaces by more general failure criteria, which may be either theoretical (mathematically derived) or empirical (experimentally derived). It can be argued that the empirical approach is more appropriate and useful, however calibration demands accurate deformation data under known conditions that may not exist or be prohibitively expensive to obtain.

Many failure criteria exist that can be used to modify the critical state model. On the "dry side", the Grittith-type, modified Griffith-type (McLintock & Walsh, 1962), Hoek-Brown (Hoek & Brown, 1980), Mohr-Coulomb, non-linear Mohr-Coulomb, or Khan empirical failure (Wong et al., 1997) can be used to modify the no-tension and Hvorslev regions. Fewer options are available for the "wet side". The empirical elliptical cap model of DiMaggio & Sandler (1971) has been successfully applied to porous sandstone by Teng-fong Wong and co-workers (Wong et al., 1997; Zhu et al., 1997; Zhu and Wong, 1997a; Zhu and Wong, 1997b) and by others (Cuss, 1999; Cuss & Rutter, 2003).

1.1.3 Critical state model for argillaceous materials

Figure 1-3 summarises the features observed for shale deformation in terms of the critical state model and the dilatancy boundary. This data is presented in the p' - q' space, but could easily be expanded into the p' - q' - v critical state space.

Within the domain below the state boundary surface, permeability and porosity reduction is essentially independent of deviatoric stress (Zhu & Wong, 1997b). Prior to yield, porosity reduction will be elastic as pore space reduces as grains elastically deform. Porosity will also reduce as pre-existing damage (i.e. fractures) elastically close.

On the dry side, stresses above the idealised Hvorslev-type surface are achievable due to the strength of lithified shale. Brittle failure occurs at a deviator given by a brittle failure criterion, e.g. the Hoek-Brown failure criterion, and deformation progresses towards the idealised Hvorslev-type surface, which corresponds to the residual strength envelope. Considerable dilatancy is observed during this stage of deformation as a shear fracture is formed in shale. The further 'left' of the dilatancy boundary, i.e. at low effective mean stresses, the more dilatant deformation is. Critical state mechanics shows that further deformation progresses towards the critical state where deformation is isovolumetric. During this progression, shale work hardens as the further granulation of material within the shear band becomes more difficult to disaggregate. Dilatancy hardening may also be present under undrained conditions. The reduction in porosity along the fracture leads to a significant reduction in permeability (a self sealing process). Permeability will reach a minimum at the critical state.

On the wet side, deformation always results in contractancy of the bulk material. This leads to a reduction in porosity by the processes of compaction/consolidation and cataclasis. Intracrystalline plasticity may also contribute to a lowering of porosity. This results in a reduction in permeability, which further reduces as deformation progresses up the Roscoe-type surface towards the critical state. The further 'right' of the dilatancy boundary, i.e. at high

effective mean stresses, the more contractive deformation is and the higher the degree of permeability reduction. The extreme case is the stress path that coincides with the NCL. Here plastic volumetric strains are largest and the decline in permeability is most marked.
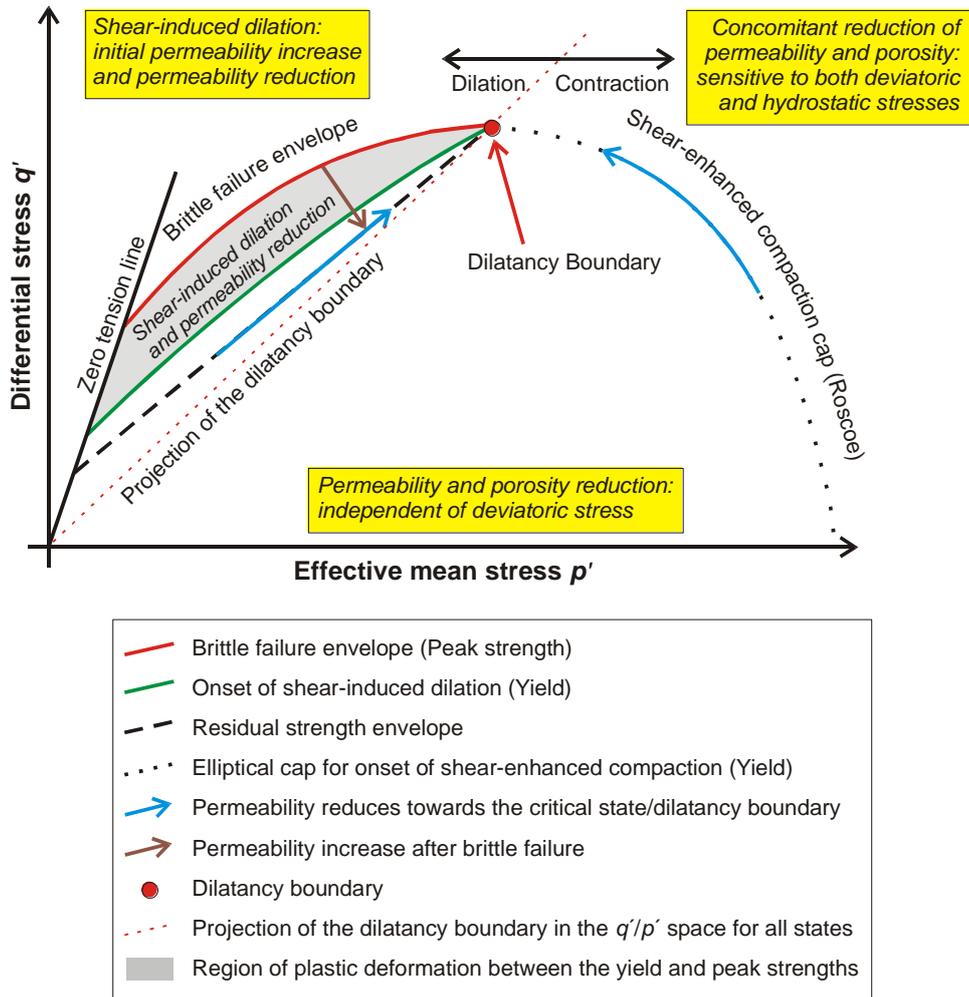
Figure 1-3 The role of the dilatancy boundary in shale sealing as shown in the p′ - q′ space. Modified from Zhu & Wong (1997b).

A thorough knowledge of the dilatancy boundary is required in order to predict the likely mode of deformation and forecast the effect of deformation on the capacity of the rock to impede fluid movement.

It can be seen that the disposal of waste in a geological repository is favourable under "wet" conditions. As long as pore pressure is not raised, which would lower effective mean stress, induced deformation under these conditions will result in a more effective self-sealing of discontinuities such as faults and fractures. The construction of a waste site will inevitably alter the local stress field, and as rocks at depth can be viewed as approaching a state of limiting equilibrium[2], deformation and yield are likely. Since permeability enhancement by dilation can be ruled out in "wet side" sediments, deformation and yield of these host materials will pose no special problems in the context of fluid flow and radionuclide transport.

---

[2] In many regions, the upper crust is subject to shear stresses approaching the frictional strength of favourably orientated faults (Engelder, T. (1993). *Stress regimes in the lithosphere*: Princeton, NJ, United States, Princeton Univ. Press, 457 pp.). This results in a state of limiting equilibrium within the crust with everywhere at the point of failure according to Byerlee's rule.

Lithified shale at shallow depths is over-consolidated, and thus deformation will tend to be on the "dry side". There seems little doubt that shales that lie substantially to the left of the dilatancy boundary, will be subject to strong dilation and permeability enhancement during repository development or disturbance by external factors such as seismicity. Self-sealing may no longer be effective in rocks which are heavily over-consolidated and prone to shear-dilatancy.

1.2   DEFORMATION AND TRANSPORT PROPERTIES

The following section briefly summarises the evidence for transport property change during deformation. Considerable work has been conducted on the porosity and permeability evolution of sediments with simple hydrostatic load, i.e. simulating increasing burial depth. Many studies have also been conducted on how permeability changes during the triaxial deformation of samples.

The permeability of any one formation is variable because it can change with corresponding changes in boundary conditions, for example stress or deformation (Heiland, 2003a). Therefore, a thorough knowledge is required of how permeability changes with stress and orientation.

In the case of underground waste disposal, the permeability of the rock mass surrounding the repository should be as small as possible. As the deformation induced during the construction of the EDZ is known to enhance permeability, research has tended to focus on looking at permeability variations associated with EDZ development. In the case of argillaceous rocks, we are interested in both the onset of dilatancy and the way in which fractures alter the hydromechanical behaviour of the EDZ.

Considerable work has also been conducted on permeability evolution by the hydrocarbons industry. As many rocks obey the law of effective stress, the lowering of reservoir pore pressures during reservoir depletion results in an increased effective stress. If a sufficient change in stress occurs, the reservoir rocks can start to compact, and this in turn will reduce permeability. Usually it is assumed that the rock mass is subject to uniaxial strain conditions during reservoir depletion, which means that only vertical compaction occurs due to increasing effective vertical stresses, and that lateral deformation is zero (Schutjens *et al.*, 1997). However, stress measurements have shown that a reservoir can undergo different stress paths, depending on the boundary conditions, geometry and the poroelastic properties of the rock (Heiland, 2003a).

The permeability of rocks has been widely reported under hydrostatic stress conditions (e.g. Zoback and Byerlee 1975a; Walsh and Brace 1984; Morrow *et al.*, 1984; David *et al.*, 1994; Dewhurst *et al.*, 1999a; Dewhurst *et al.*, 1999b; Katsube, 2000; Katsube *et al.*, 1996a; Katsube *et al.*, 1998; Kwon *et al.*, 2001; Neuzil *et al.*, 1984) in order to establish the relationship between effective stress and permeability for different rock types. However, in the field, rocks are normally subjected to an inhomogeneous stress-field, where the vertical stress (determined by the weight of the overburden) exceeds the two horizontal stresses (Holt 1990). This has led to investigations of the sensitivity of matrix permeability to non-hydrostatic stress conditions, especially in sandstones (e.g. Keaney *et al.*, 1998; Zhu and Wong, 1994; Zhu and Wong, 1997).

Volumetric deformation of shale on the 'dry side' (brittle field) is complex. Figure 1-4 shows the volumetric strain for a sample of North Sea shale (from Remvik & Skalle, 1993). As the sample contracts in the elastic phase, the pore pressure increases. At or around the onset of yield (point of initiation of permanent deformation), contraction behaviour stabilises, and by the peak strength, shale has initiated dilatant deformation. In undrained conditions, a pore pressure maximum is observed. Plastic volumetric strain starts to dilate around the peak of the total volumetric strain curve; this increase in microcrack porosity explains why the pore pressure decreases.
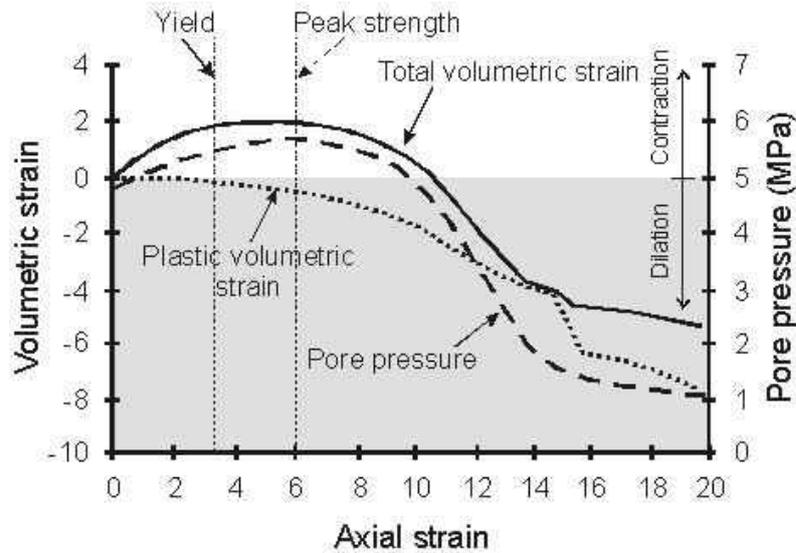
Figure 1-4 Total and plastic volumetric strain for North Sea shale during 'dry' deformation (modified from Remvik & Skalle, 1993).
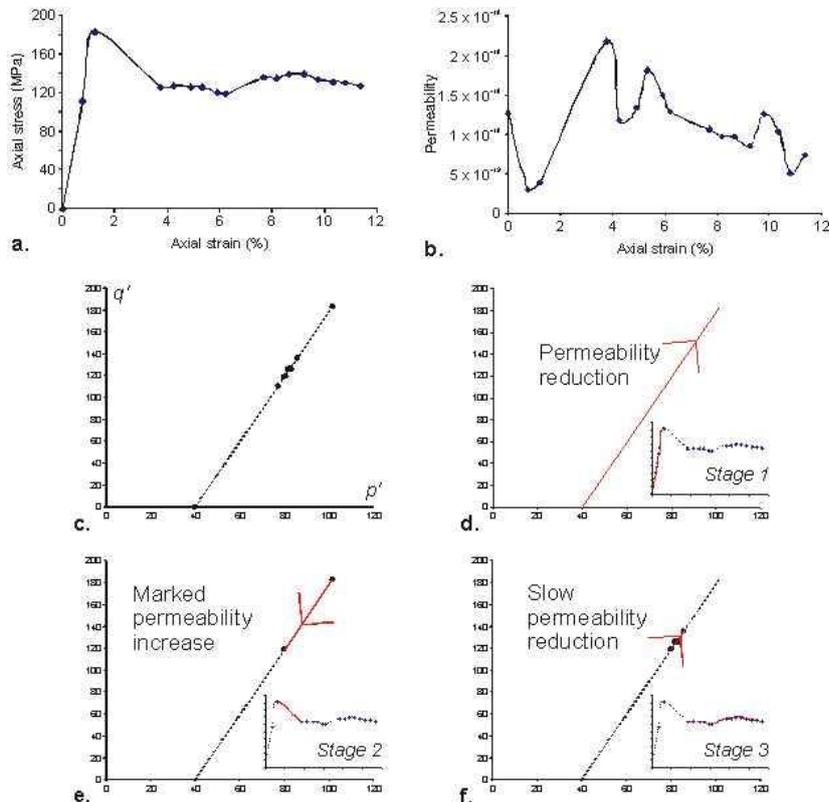
Figure 1-5 Evolution of permeability in Tennessee sandstone during brittle fracture: a) stress-strain result, b) permeability-strain result, c) the stress path taken during deformation, note that a straight line is the result as the pore-pressure is kept constant, d) – f) permeability observations during the different stages of brittle deformation. Data from Keaney *et al.* (1998).

The work of Keaney *et al.* (1998) illustrates the complex evolution of porosity and permeability (Figure 1-5) during brittle fracturing in a drained system. During the elastic stage of deformation, porosity and permeability decrease due to the elastic closure of pre-existing fractures and the poroelastic response. At about 1% axial strain, dilatant volume increase is initiated as new fractures are formed. After about 1.5% axial strain, the net volume of the sample is less than when first tested. At the peak stress level, deformation is concentrated into a fracture by the

14

process of shear localisation. During the stress drop, permeability is markedly increased as the stress level equilibrates to the residual strength of the material. As deformation continues at the residual strength, the permeability reduces. Porosity continues to increase slowly. Strain hardening and experimental artefacts may contribute to this observation, but it is clear that permeability does decrease as the localised fracture develops.

These observations show that permeability both decreases and increases in the brittle regime. This can be explained microstructurally by observing what happens at the different stages of shear localisation. Several workers have described the microstructural evolution of different sandstone types during deformation (Cuss, 1999; Cuss *et al*., 2003; Menéndez *et al*., 1996). With the application of axial load within the elastic region, porosity closes preferentially in the axial direction, resulting in the formation of axial impingement fractures between point contacts. Porosity increases and tortuosity decreases as these fractures open, resulting in an increase in material permeability. Damage concentrates into a band angled at 30° to the axial load. Further deformation is concentrated within the shear band; no deformation is observed away from this feature. As strain increases at the residual strength, the central shear zone broadens and the gouge material becomes finer grained. The reduction in grain size and associated compaction within the shear band creates an effective barrier, reducing the bulk permeability of the test sample, as described by Keaney *et al*. (1998). Although this work, and work by Zhu & Wong (1997), has been conducted on sandstones, it represents the best data available for permeability changes during deformation.

1.3   STRESS PATHS DURING TUNNELLING

The construction of a gallery within pre-stressed rock will result in some form of stress concentration that will in turn result in deformation. The transient nature of tunnel construction will play a significant role in that deformation, as will the method of construction. Tunnel construction is slow compared to the transient (creep) properties of rock, so the way in which the gallery face progresses will influence subsequent deformation. As deformation at the face will occur, other physical properties, such as pore pressure, will also change before the face is completed. Hence it is vital to consider the transient changes in stress during construction and analyse how these influence deformation. Stress path modelling of tunnels has become common practice. This requires careful stress path experiments as well as stress path analysis of models. A comprehensive review of stress paths and tunnels is given by Barla (1999).

Finite element analysis of an elasto-plastic medium was conducted by Ng and Lo (1985) in order to determine the stress path at three typical points around a tunnel. These points corresponded to the tunnel roof or crown, the sidewall, and a point half way between the two. This enables a continuous stress path to be determined for the entire tunnel, with 45° between estimates. Figure 1-6 shows the result of this study, with a $K_0 = 0.75$ condition and the excavation process simulated by reducing the initial stresses. The study shows that the tunnel wall has a significant stress path history. Steiner (1992) showed that the shape of the tunnel plays a significant role on the resulting stress-path.

Bellwald (1990) and Aristorenas (1992) examined the effective stress path around a tunnel by means of theoretical considerations and showed there are two clear phases of the stress path:

1. The first is created during the tunnel excavation,

2. The second phase occurs after excavation and is a drained phase when the negative excess pore pressure dissipates.

The construction of a tunnel into material that may undergo swelling will alter the stress path and needs to be incorporated into coupled models. This was addressed by Anagnostou (1991), who interpreted the time-dependent development of swelling strain as a consequence of the dissipation of negative pore pressure. Tunnel geometry change will occur slowly and will change the stress path as plastic deformation occurs.
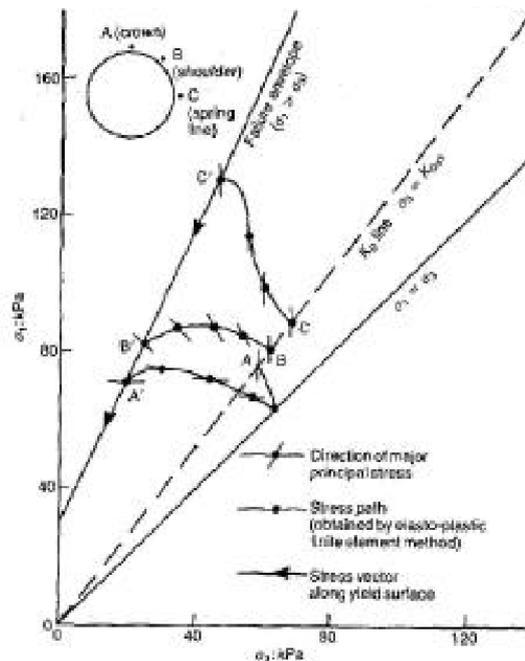
Figure 1-6 Stress paths for typical elements in soil due to tunnelling (Ng and Lo 1985; taken from Barla, 1999).

1.3.1   Stress paths during face advancement: 3-D Elastic Stress Paths

The work of Barla and co-workers at the Politecnico di Torino, Italy (G. Barla, M. Barla, M. Bonini) gives a useful account of stress paths created by an advancing excavation in rock (Barla, 1998; Barla, 1999; Bonini *et al.*, 2001; Barla, 2001; Barla and Barla, 2001). This work was carried out by numerical analysis using finite difference element modelling (Flac and Flac3D: Itasca, 1996) and boundary element modelling (Examine3D: Rocsicience, 1998). The study modelled stress paths at the sidewalls (S) and at the crown/invert (C).

The stress states at points C and S depend on the depth of cover and the stress ratio (minimum to maximum principal stress ratio, K_0) prior to excavation. The tunnel face advances during excavation and continues to completion of excavation. The Torino study considered two different stress conditions, depending on the K_0 ratio. For each case, two-dimensional and three-dimensional analyses were performed and the results compared with the closed form solutions available.

The numerical results (Figure 1-7) show a significant difference between the stresses computed for three-dimensional and two-dimensional conditions, with clear implications for understanding the stress path around the tunnel. It is evident that the stress history, particularly near the tunnel face, can only be properly described by simulating three-dimensional conditions (Bonini *et al.*, 2001).

16

a).

b).
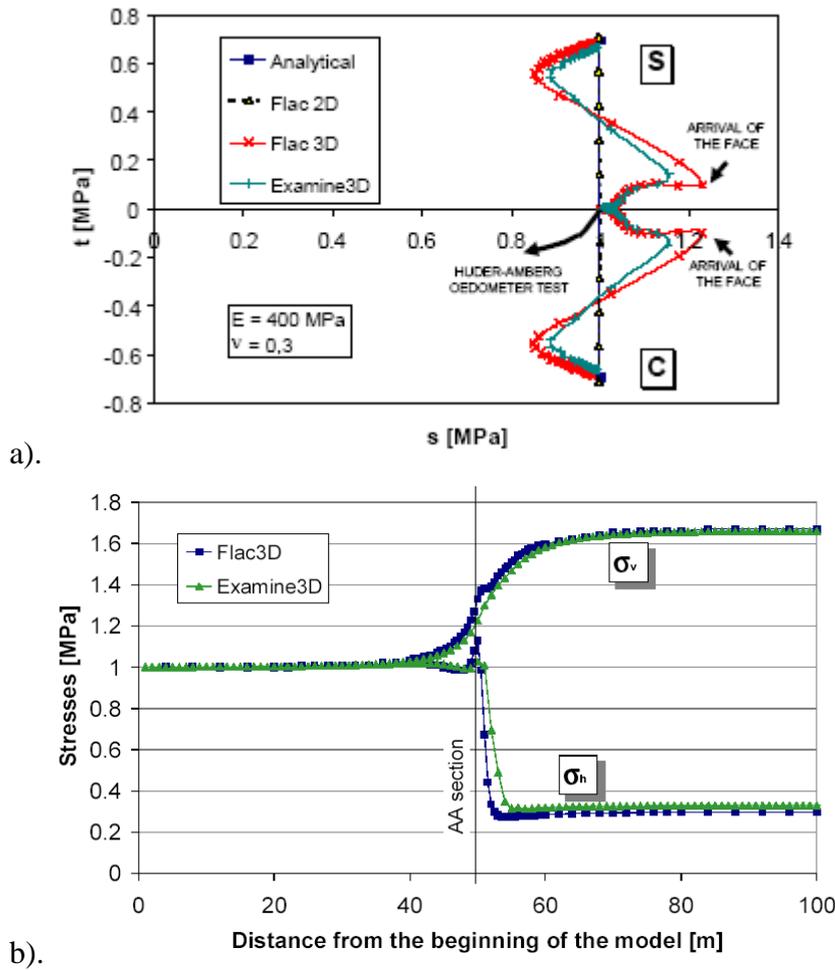
Figure 1-7 (a) Stress paths for points S (sidewalls) and C (crown/invert) for the elastic $K_0 = 1$ analyses. (b) Vertical and horizontal stresses at point S in the sidewalls for the 3D elastic $K_0 = 1$ analysis (from Bonini *et al.*, 2001).

1.3.2 Stress paths during face advancement: 3-D elastoplastic stress paths

Barla *et al.* (Barla, 1998; Barla, 1999; Bonini *et al.*, 2001; Barla, 2001; Barla and Barla, 2001) modelled the system as elastoplastic with strain-softening. A limit value (ε_1) for the axial strain (ε) was defined below which the peak strength parameters (τ_o = cohesion, ϕ = friction angle) apply. For values of ε greater than ε_1, the strength parameters are taken to change linearly down to the residual strength parameters (c_r, ϕ_r), which hold true for ε greater than the limit value ε_2 (Barla, 1999).

During the simulation, strength is exceeded and plastic deformation occurs around the tunnel. When $K_0 = 1$, the stress initially increases and then decreases strongly with distance from the beginning of the model at both points S and C, as shown for S in Figure 1-8. The decrease in stress initiates when the excavation face is still 5 to 6 metres away from the monitored section, A-A. This analysis shows that a plastic zone is created around the tunnel during excavation. When the deformation resulting from the stresses changes from elastic to plastic behaviour, both the vertical and horizontal stresses decrease to a small value and determine the decrease of *s*. This occurs as soon as the plastic zone gets through the A-A section. After this point, there is very little change in the state of stress.
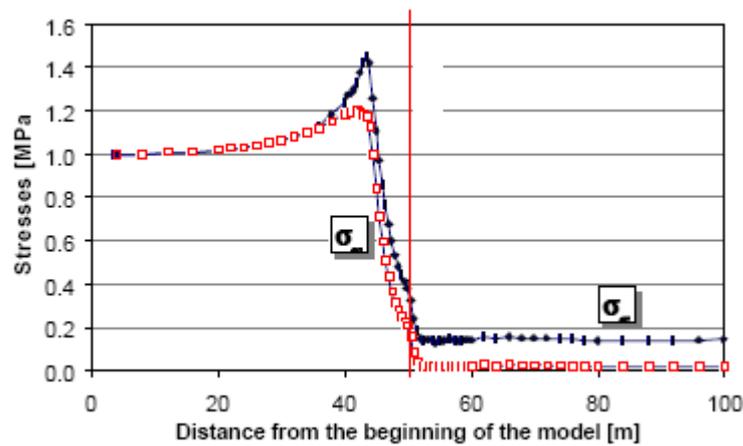
Figure 1-8 Stresses at point S (sidewall) for the 3D elastoplastic $K_0 = 1$ analysis (from Barla, 1999).

1.3.3   Conclusions of stress-paths

The work summarised above shows that stress paths are highly complex during the construction of a repository tunnel. Wall rock will undergo large changes in stress as the tunnel advances, and with the addition of time-dependent deformation, further stress path changes will occur while the tunnel is open. Long-term convergence will result in a further modification of the stress-path. Therefore, it is essential to understand the effect the changing stress path has on the physical and transport properties of the Callovo-Oxfordian claystone.

1.4   CONCLUSIONS OF PREVIOUS WORK

This brief introduction has shown that changes in stress during the construction of a repository will occur and the likely effect this would have on the transport properties of Callovo-Oxfordian claystone. It is clear that permeability will vary depending on the stress path, and the description of the observations in terms of the critical state model will allow quantitative and qualitative predictions to be made.

2 Experimental geometry

2.1 TEST MATERIAL

The composition of the Callovo-Oxfordian claystone (150-160 Ma) can be divided in to three main constituents; clay, silt and carbonate. Wenk *et al.* (2008) reports these constituents (at the Bure site) as follows; clay 25-55 wt%, 23-44% carbonates and 20-31% silt (essentially quartz + feldspar). Clay minerals are reported to include illite and illite-smectite with subordinate kaolinite and chlorite. In the upper half of the formation the illite-smectite is disordered and contains 50-70% smectite interlayers, whilst in the lower half the illite-smectite is ordered (R=1 type) with lower contents (20-40%) of smectite interlayers (Wenk *et al.*, 2008). Beds can contain common organic matter.

Other authors report compositions similar to these. Wileveau & Bernier (2008) quote values for quartz (18%), calcite (25%), clay minerals (55%; illite-smectite ~65%, illite 30%) and kaolinite and chlorite (2%) with subordinate feldspars, pyrite and iron oxides (2%). Esteban *et al.* (2006) report 35-60% clay minerals with the remaining shared by calcite and silt. Gaucher *et al.* (2004) includes highly detailed mineralogical and chemical compositions of the sequence which are again in broad agreement with the above compositions.

The claystone was deposited under marine basin conditions during a period in which the Paris Basin was variously linked to the Atlantic and Tethyan Oceans, as well as to the London Basin and North Sea (Rousset & Clauer, 2003). Clay sedimentation is therefore considered to have two primary inputs; continental and oceanic. The claystone is over- and underlain by Oxfordian and Bathonian shelf limestones. It is primarily clayey at its base, then becomes increasingly silty and then increasingly calcareous at its top (Gaucher *et al.*, 2004). A maximum clay content zone within the clayey base has been identified; this is interpreted to mark the inflection point (and interval of maximum flooding) from a lower transgressive sequence to an upper regressive sequence (Gaucher *et al.*, 2004).

Upon receipt of the preserved T1-cell core barrels at BGS, the material was catalogued and stored under refrigerated conditions of 4°C (to minimise biological and chemical degradation) ready for future testing. The production of samples 75mm length and 56mm diameter was proved problematic. The core material is delivered with a rubber material around the CoX sample, surrounded by a cement material with a plastic outer jacketing material, as seen in Figure 2-1a. Each T1-cell contains approximately 300mm of core, enough for three finished samples. The core barrel was cut into three (approximately 100mm length) using a dry-cut diamond encrusted bladed saw (see Figure 2-1b). The dry-cutting of the core barrels proved problematic as the blade tends to bind and snag in the hard cement material used to pack the barrel. This results in damage to the sample material, as seen in Figure 2-1c. In order to reduce this problem the packing material was removed prior to cutting to 100m length samples.

The core material was sub-sampled to 56mm diameter and approximately 75mm length using a combination of dry core-drilling (with gas flushing and vacuum removal of fines, as shown in Figure 2-1d) and diamond slicing. Core drilling was also problematic as the samples contained a number of weaknesses (micro-fractures and fossils) that resulted in the samples splitting along their length, as seen in Figure 2-2. One sample was successfully cored and was finished by trimming on a lathe to get a good even surface finish and the sample ends were ground flat and parallel to minimise "end-effects" during testing. The specimen was accurately measured using a digital micrometer and weighed. Off-cuts from the coring process were weighed and oven dried to obtain an estimate of moisture content. The dimensions and provisional geotechnical properties of the specimen are given in Table 2-1.

Figure 2-1 Sample preparation. (a) The core samples are delivered with the CoX material encased in a thin rubber material, surrounded by a cement material, and the outside of the core barrel is a plastic material. (b) The 300mm length core barrel was sub-sampled into 100mm length by dry cutting using a diamond encrusted blade. (c) Damage caused to the CoX core as the dry cutting blade "sticks" while cutting the hard cement packing material. (d) Dry diamond coring of a 100mm length of CoX core material. (e) Finished sample of CoX.

Figure 2-2 A sample of CoX that split lengthwise while being diamond cored. As can be seen, the core split revealing a fossil within the core (see right). Two samples split lengthwise during sample preparation.

The initial test specimen, designated SPP_CoX-1, was cut perpendicular to the bedding, and was taken from drilling core EST30340, dated 30/10/08 from location OH2, T cell T1.1112, drilling interval 30.17m to 30.49m. The torque applied to the axial confining system of the T1-cell was around 18 Nm.

	Units	Value
Sample reference		SPP_CoX-1
Average length	mm	76.63 ± 0.02
Average diameter	mm	55.50 ± 0.01
Volume	m^3	1.854×10^{-4}
Average weight	g	455.6
Density	g.cc^{-1}	2.458
Grain density	g.cc^{-1}	2.7
Moisture weight	g	24.6
Moisture content	%	5.7
Dry weight	g	431
Dry density	g.cc^{-1}	2.33
Void ratio		0.166
Porosity	%	14.2
Saturation	%	93

Table 2-1 Provisional dimensions and basic properties of the Callovo-Oxfordian claystone test material (sample SPP_CoX-1) from pre-test measurements of water content from off-cut material adjacent to the core. An assumed specific gravity for the mineral phases of 2.70 Mg.m-3 (Zhang *et al.* 2007) was used in these calculations.

2.2 BASIC PHYSICAL PROPERTIES

The starting sample was measured five times for length and four times for diameter. The sample was weighed, which allowed bulk density to be determined. Table 2-1 shows the preliminary pre-test physical properties of the specimens based on the moisture content of the off-cuts and a grain density of 2.70 Mg m^{-3} (Zhang *et al.*, 2007). The provisional data presented in Table 2-1 is in fairly good agreement with the generic values quoted by Zhang *et al*.

2.3 EXPERIMENTAL SET-UP

The stress-path permeameter (SPP) is an evolution of the elastimeter apparatus that has been shown to perform well (Horseman et al., 2005). A schematic of the SPP is shown in Figure 2-3, along with a photo in Figure 2-4. The SPP comprises 6 main components:

1) The specimen, surrounded by a modified flexible Hoek sleeve (Figure 2-5b) and main pressure vessel body.

2) Three dash pots (Figure 2-5c) that are mounted along the radial mid-plane of the sample which directly measure the radial strain of the sample. The dash pots are pressure balanced in order to reduce the force imposed upon the sample and to make sure the push-rods are not simply pushed out of the pressure vessel.

3) An axial load system comprising of an Enerpac single acting hydraulic ram (see Figure 2-4) pressurised by an ISCO-500 series D syringe pump. This is connected via an axial strain jig to a Global Digital Systems optical encoder for measuring linear displacement accurate to 0.003 mm. Miniture load cells are located at the piston ends to measure stress at the sample ends.

4) A confining pressure system using an ISCO-500 series D syringe pump allowing radial strain measurements to be calculated through volume change.

5) A pore pressure system comprising two ISCO-100 series D syringe pumps to create pore fluid pressure and monitor back pressure. The injection media can be either water or gas (usually Helium).

6) A state-of-the-art custom designed data acquisition system facilitating the remote monitoring and control of all experimental parameters.

A cylindrical rock specimen is positioned between two stainless steel platens and jacketed in a flexible Hoek sleeve to exclude the confining fluid (Figure 2-5b). The inlet and outlet zones for water flow to and from the specimen are provided by stainless-steel discs, nominally 20 mm in diameter and 3 mm depth. Guard rings of 6mm thickness and 2 mm depth are located on the outer diameter of the platens, allowing pore pressure to be measured in two locations on the faces of the sample.

The stainless steel load platens are in direct contact with the sample transmitting the axial force generated by the Enerpac ram directly to the specimen. Each platen has two ports facilitating flushing of the system and the removal of residual air prior to testing. Retaining collars and axial tie-rods lock the system components together to provide a rigid test rig, these are pre-tensioned at 300 Nm.

Axial displacement is measured using the GDS optical encoder connected to stainless steel push rods terminating a short distance behind the load-bearing face of each platen to minimise compliance effects. Data from the optical encoder is processed through a multiplexer to provide a continuous measure of axial strain. The confining system provides an indirect measurement of radial strain by monitoring changes in volume while porewater displacement is monitored via the backpressure system.

Three pressure balanced dash-pots (Figure 2-5c) are located around the radial mid-plane of the specimen. Brass push-rods are in direct contact with the outer diameter of the Hoek sleeve. Three 10×10 mm brass plates are cemented to the outer edge of the Hoek sleeve (Figure 2-5b) in order to reduce the force the push-rods impose on the sample surface. The push rods extend to the outside of the pressure vessel, where high precision LVDTs are used to measure the displacement of the sample diameter.

Each ISCO pump controller has an RS232 serial port that allows volume and pressure data to be transmitted to an equivalent port of a 32-bit personal computer. A state-of-the-art data acquisition system was developed using National Instruments LabVIEW™ software. The system allows both remote access to test parameters and control of all ISCO pumps via a LAN based telemetry link. The software prompts the pump controller and multiplexer unit to transmit data to the computer at pre-set time intervals. Data can be downloaded at any time without physical access to the laboratory, minimising thermal variations due to personnel working in the laboratory environment.
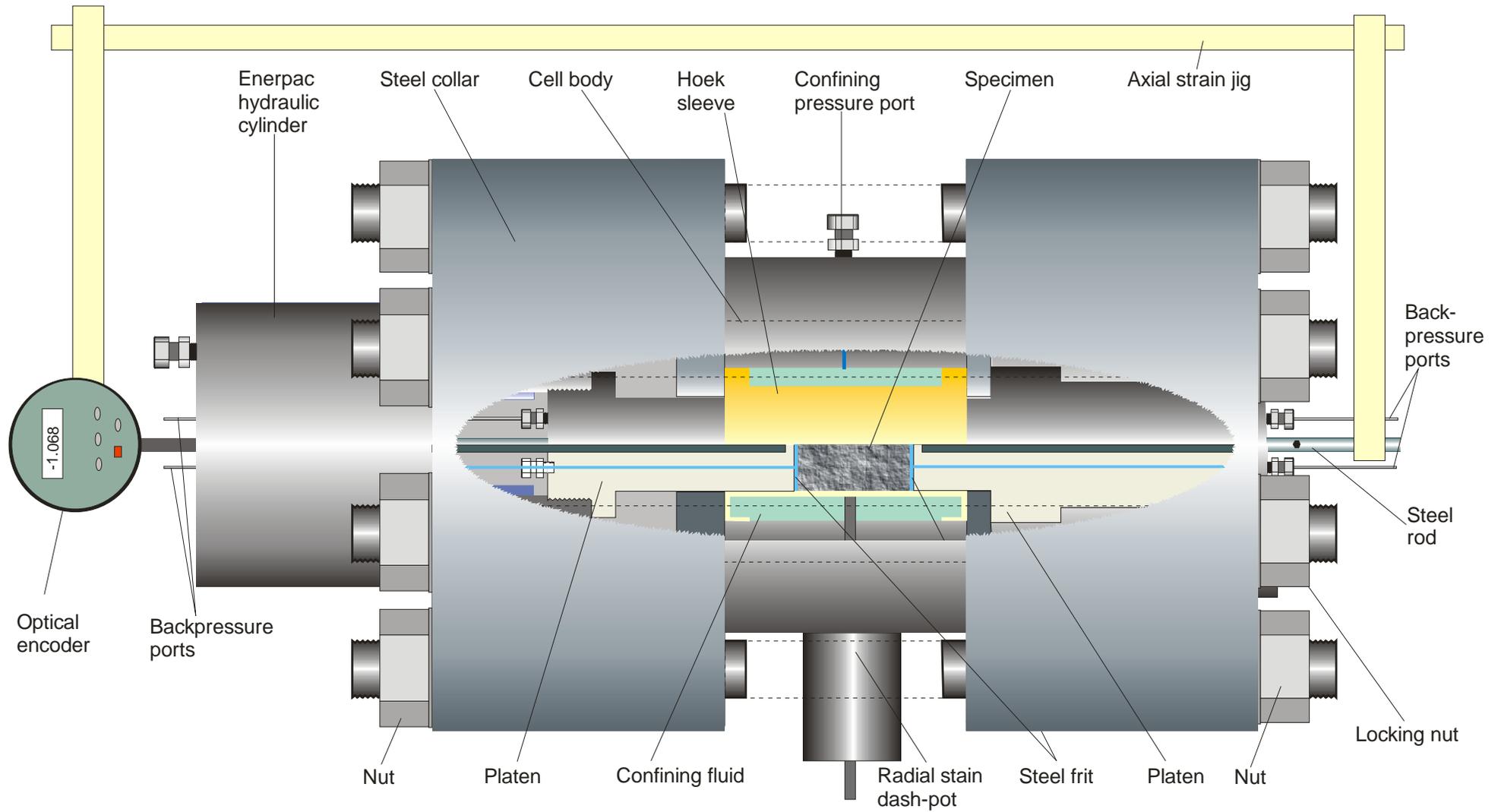
Figure 2-3 Schematic of the Stress Path Permeameter (SPP).
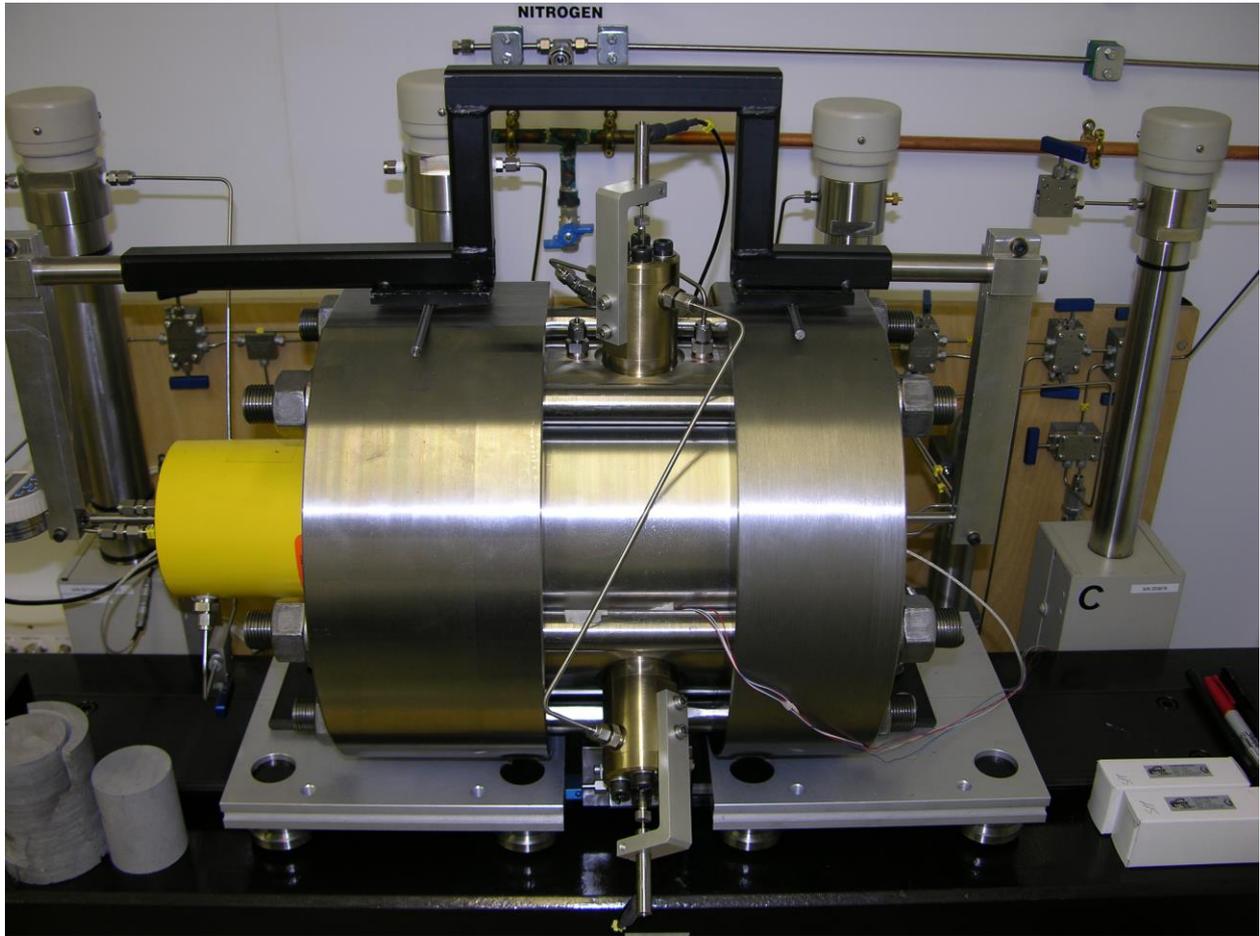
Figure 2-4 Photo of the SPP apparatus. The hydraulic ram (yellow) can be seen, along with the dash-pots used to measure radial deformation of the jacketed samples.

2.3.1 Measured parameters

The SPP logging software directly records the following parameters every 2 minutes:

- SPP injection circuit pump (pressure, flow and volume)
- SPP back-pressure circuit pump (pressure, flow and volume)
- SPP axial load pump (pressure, flow and volume)
- SPP confining pressure pump (pressure, flow and volume)
- Load cell on the injection platen
- Load cell on the back-pressure platen
- Radial displacement of the sample mid-plane (Radial 1, Radial 2 & Radial 3)
- Axial displacement of the sample
- Temperature (vessel, laboratory low level and laboratory high level)

From the measured parameters, the following calculated parameters can be determined:

- Axial strain of the sample
- Radial strain of the sample
- Volumetric strain of the sample
    - From direct measurements on the sample
    - From displacement of confining fluid
- Permeability and storage capacity
- Stress state

25

In addition to these parameters, physical properties can be recorded prior to testing and on test completion.
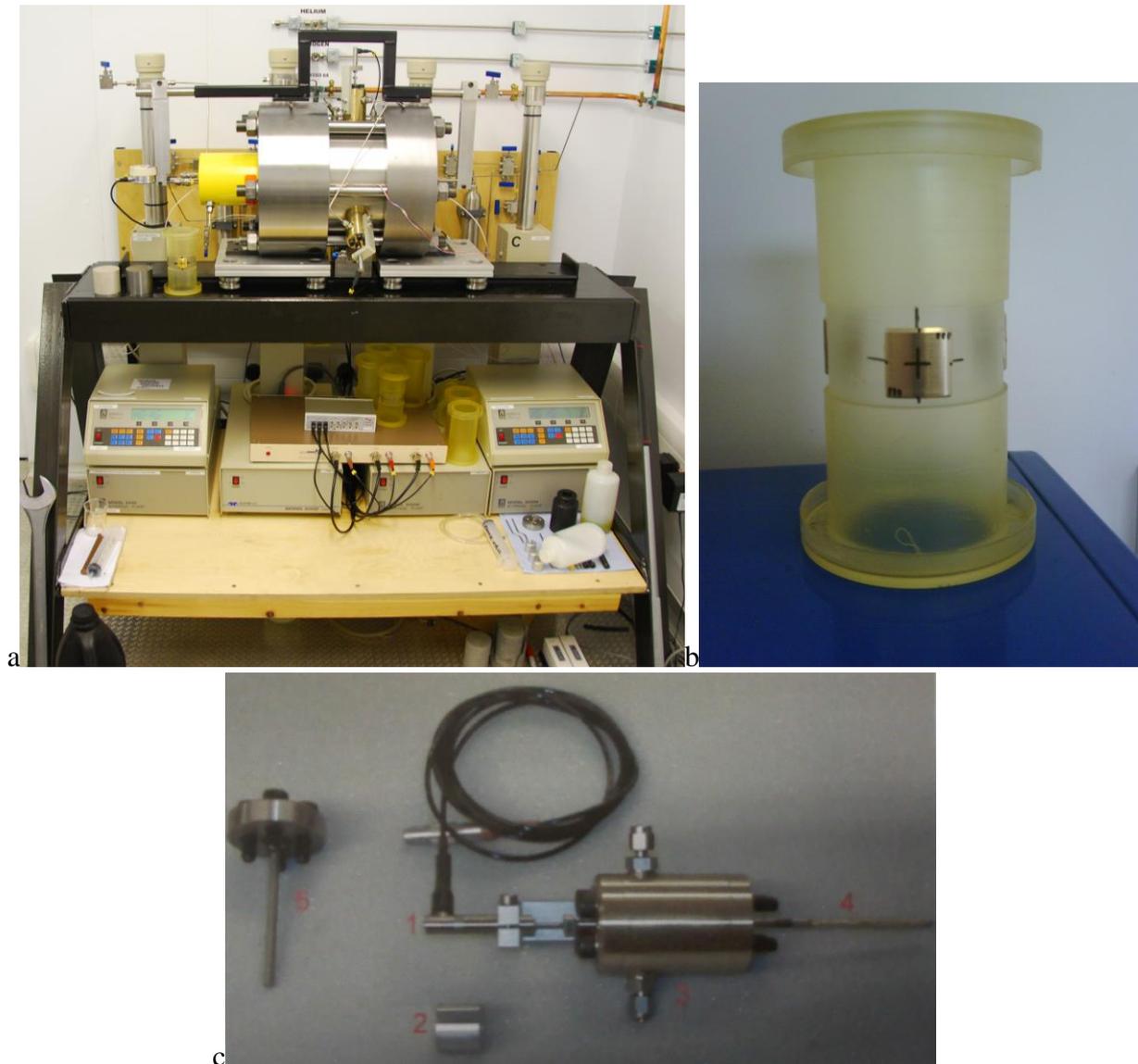
Figure 2-5 Components of the SPP. (a) The complete apparatus, showing the pressure vessel, pressure distribution board, four ISCO pumps [confining pressure, axial load, injection and back pressure], and optical encoder box. (b) Modified Hoek sleve with brass additions that are in direct contact with the arms of the dash-pot arrangement. (c) Pressure balanced dash-pot system. The dashpot arm [4] is in direct contact with the outside of the sample jacket. The movement of this arm is recorded by a high-precision LVDT [1]. The dashpot is pressure balanced through the pressure ports marked [3].

2.4   CALIBRATION AND DATA ACQUISITION

A thorough set of calibration tests were undertaken in order to prove the new SPP apparatus and to calibrate its systems, as described in Table 2-2.

Confining, injection, backpressure and axial loading syringe pumps were calibrated using a Druck PTX610 pressure transmitter. Linear regression of data was undertaken to provide calibration values. In order to determine the axial load applied to the specimen through the surface of the platen at any given pump pressure, it is essential to accurately calibrate the ISCO

pump used to pressurise the Enerpac ram. To minimise residual error between calibrated and measured values a second order polynomial fit was applied to the data. Calibration values were then multiplied by the ratio of surface areas between the ram piston and platen.

2.4.1 Testing for compliance in apparatus

In order to try to assess the degree to which compliance of the apparatus might be affecting the results, the deformation of "standard" metal bars were measured within the apparatus under a series of applied axial and radial stresses (tests SPP_Cal07 & SPP_Cal09). Two materials were selected; 1) magnesium alloy, which is a relatively soft metal, and 2) tungsten, which is a very compliant metal. The magnesium alloy material was tested by the National Physics Laboratory to give accurate elastic constants for the reference material. The use of pure tungsten meant that reference elastic constants could be used.
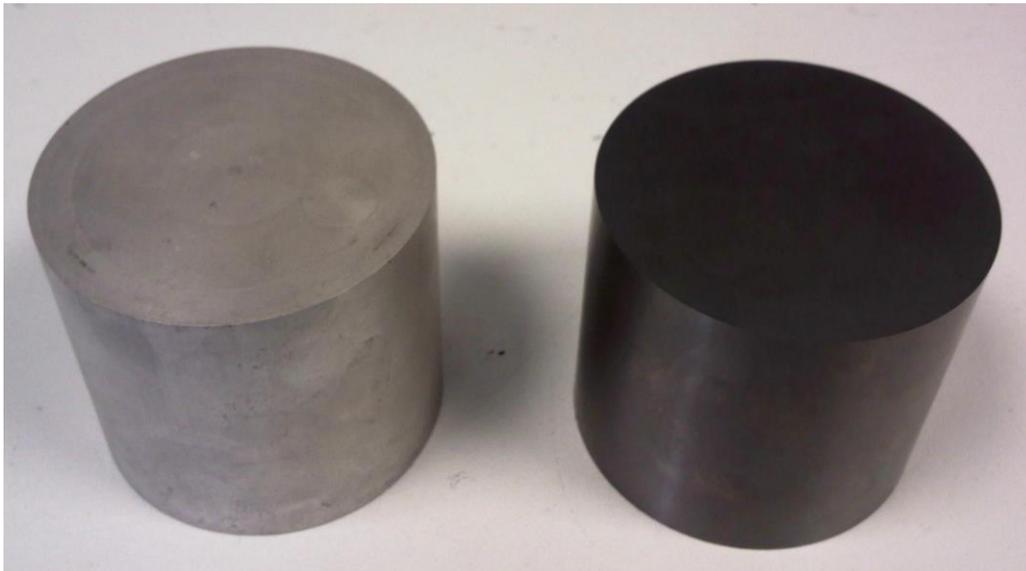
Figure 2-6 Calibration dummy samples; Magnesium alloy (left) and Tungsten (right).

The magnesium alloy test bar measured 50 mm in length and 56 mm in diameter; Its Young's modulus and Poisson's ratio was certified as 41.97 GPa and 0.29 respectively. The tungsten test bar measured 50.01 ± 0.01 mm in length and 56 ± 0.06 mm in diameter; Its Young's modulus and Poisson's ratio was assumed to be 411 GPa and 0.29 respectively. The test bars were subjected to a series of increasing and then decreasing axial stresses at a range constant confining pressures (1, 5, 10, 20 and 30 MPa). Care was taken not to overload the samples and differential axial loading was limited to 25 MPa. Axial and radial displacements were observed during the pressure cycles and the results are given in Table 2-3. These results show that the apparatus is stiff, especially when one considers the likely strength and deformability of Callovo-Oxfordian claystone. Therefore the deformation of the experimental apparatus can be considered negligible compared with the expected deformation of the test material.

Test number	Date	Sam^p	Description
SPP_Cal01	11/11/08	Mg	General testing of components • Confining pressure of 4 MPa; Axial load of 4.5 – 48 MPa
SPP_Cal02	11/11/08	Mg	Compliance test at 200 lb.force • Confining pressure of 1 MPa; Axial load of 2 – 24 – 2 MPa
SPP_Cal03	10/12/08	Mg	Compliance test at 300 Nm • Confining pressure of 1 MPa; Axial load of 2 – 48 – 2 MPa
SPP_Cal04	16/12/08	Mg	Compliance test at 300 Nm • Confining pressure of 1 MPa; Axial load of 2 MPa • Confining pressure of 46 MPa; Axial load of 48 MPa • Confining pressure of 1 MPa; Axial load of 48 MPa
SPP_Cal05	12/1/09	Mg	Compliance test at 300 Nm • Confining pressure of 2 MPa; Axial load of 2.5 MPa • Confining pressure of 2 MPa; Axial load of 2.5 – 48 MPa
SPP_Cal06	21/7/09	Mg	Compliance test at 300 Nm • Confining pressure of 1–40 MPa; Axial load of 20 – 48 – 10 MPa
SPP_Cal07	16/10/09	Mg	Test of compliance: • Confining pressure of 1 MPa; Axial load of 3.8 – 28.5 – 3.8 MPa • Axial load of 11 MPa; Confining pressure of 1 – 5 – 1 MPa
SPP_Cal08	13/11/09	Mg	Test of radial dash pots: • Confining pressure of 1 MPa; Axial load of 1.5 – 20 – 1.5 MPa • Confining pressure of 5 MPa; Axial load of 6 – 22 – 6 MPa • Confining pressure of 10 MPa; Axial load of 12 – 35 – 12 MPa
SPP_Cal09	16/11/09	Mg	Test of radial dash pots: • Confining pressure of 10 MPa; Axial load of 12 – 35 – 12 MPa • Confining pressure of 20 MPa; Axial load of 24 – 45 – 24 MPa • Confining pressure of 30 MPa; Axial load of 34 – 46 – 34 MPa • Confining pressure of 30 MPa; Axial load of 33 – 47 – 33 MPa
SPP_Cal10	16/11/09	Mg	Repeated loading cycles • Confining pressure of 10 MPa; Axial load of 11–35–11 MPa × 3
SPP_Cal11	17/11/09	Mg	Check of LVDTs • Confining pressure of 20 MPa; Axial load of 24 – 45 – 24 MPa • Confining pressure of 30 MPa; Axial load of 33 – 47 – 33 MPa
SPP_Cal12	18/1/10	Mg	Compliance test • Confining pressure of 1 MPa; Axial load of 1.5 – 20 – 1.5 MPa • Confining pressure of 5 MPa; Axial load of 6 – 25 – 6 MPa • Confining pressure of 10 MPa; Axial load of 12 – 35 – 12 MPa • Confining pressure of 20 MPa; Axial load of 24 – 45 – 24 MPa • Confining pressure of 30 MPa; Axial load of 34 – 46 – 34 MPa
SPP_Cal13	9/2/10	Mg	Pressure cycle test at 10 MPa. • Confining pressure of 10 MPa; Axial load of 12–35–12 MPa × 3
SPP_Cal14	2/3/10	Wg	Compliance test with Tungsten • Confining pressure of 1 MPa; Axial load of 1.5 – 20 – 1.5 MPa • Confining pressure of 5 MPa; Axial load of 6 – 25 – 6 MPa • Confining pressure of 5 MPa; Axial load of 12 – 35 – 12 MPa • Confining pressure of 5 MPa; Axial load of 24 – 45 – 24 MPa • Confining pressure of 10 MPa; Axial load of 12 – 35 – 12 MPa • Confining pressure of 20 MPa; Axial load of 24 – 45 – 24 MPa • Confining pressure of 30 MPa; Axial load of 34 – 46 – 34 MPa • Confining pressure of 10 MPa; Axial load of 12–35–12 MPa × 4
SPP_Cal15	4/5/10	/	Pump calibration (injection & back pressure)
SPP_Cal16	5/5/10	/	Pump calibration (axial load)
SPP_Cal17	5/5/10	/	Pump calibration (confining pressure)
SPP_Cal18	Tba	/	Guard-ring pressure transducer calibration

Table 2-2 List of calibration tests undertaken to prove and calibrate the SPP apparatus.

Confining pressure (MPa)	Axial load (MPa)	Axial displacement (micron)	Radial displacement (micron)	Calculated axial displacement (microns)	Calculated radial displacement (microns)
Magnesium alloy					
1	1.5 – 20 – 1.5	43 (10)	7 (1.3)	22	6.4
5	6 – 25 - 6	34 (6)	5 (0)	22.6	6.6
10	12 – 35 – 12	43 (8)	6 (1)	27.4	7.9
20	24 – 45 – 24	36 (8)	3 (0)	25.0	7.3
30	34 – 46 – 34	15 (4)	1 (0)	14.3	4.1
10	12 – 35 – 12	36 (-1)	4.5 (-1)	27.4	8.9
10	12 – 35 – 12	50 (11)	6.6 (-1.4)	27.4	8.9
10	12 – 35 – 12	46 (9)	5.6 (2.1)	27.4	8.9
Tungsten					
1	1.5 – 20 – 1.5	15 (-3)	23.6 (8.4)	22.5	7.3
5	6 – 25 - 6	10 (-2)	12.7 (2.7)	23.1	7.5
5	12 – 35 – 12	8 (0)	12.4 (2.5)	27.9	9.1
5	24 – 45 – 24	3 (1)	10.8 (0.7)	25.5	8.3
10	12 – 35 – 12	6 (-2)	13.8 (0.1)	27.9	9.1
20	24 – 45 – 24	2 (-1)	17.4 (-0.3)	25.5	8.3
30	34 – 46 – 34	1 (1)	25.5 (-0.2)	14.6	4.7
10	12 – 35 – 12	5 (-1)	14.2 (1.4)	27.9	9.1
10	12 – 35 – 12	4 (4)	13.1 (0.6)	27.9	9.1
10	12 – 35 – 12	4.5 (0.5)	12.1 (0.4)	27.9	9.1
10	12 – 35 – 12	2 (0.5)	11.9 (0.3)	27.9	9.1

Table 2-3 Results for compliance testing experiments with aluminium alloy bar and tungsten bar (parenthesis report values of hysteresis).

3 Planned experimental programme

The experiment will be conducted with a control on axial load, confining pressure and pore pressure. The resultant strains will be monitored on the platen ends and at three locations around the sample centre. The sample is able to undergo volumetric deformation and is only constrained by a confining fluid.

The experiment will follow given stress paths. A series of steps will be conducted to approximate the paths by changing axial load and confining pressure; it may also be necessary to alter pore-pressure. While the transition between steps will be relatively quick, stress conditions will then be held constant for several weeks in order to achieve steady flow conditions.

The experimental programme is not fixed and the results and observations from one test will feed into the next. The original plan was to conduct five experiments in order to examine the evolution of aqueous and gaseous permeability in response to changes in effective stress. Specific details of individual test programmes cannot be described due to the evolutionary nature of the research and the need for a flexible experimental programme to be able to adapt to nascent results. However, a general outline plan of activities is provided below for guidance, though test stages may be added or deleted depending on previous results. It should also be noted that the duration of particular tests is an unknown and may result in the deletion of specific tasks. As such, tests will be performed in the order they are listed.

Figure 3-1 shows the position of the Hoek-Brown failure criterion as supplied by Andra for the CoX when plotted in the $q - p$ space. The stress state of Bure is well defined with a confining pressure of 12.5 MPa. A pore pressure of 4.5 MPa is typical, giving a starting effective mean stress of 8 MPa for all stress paths.
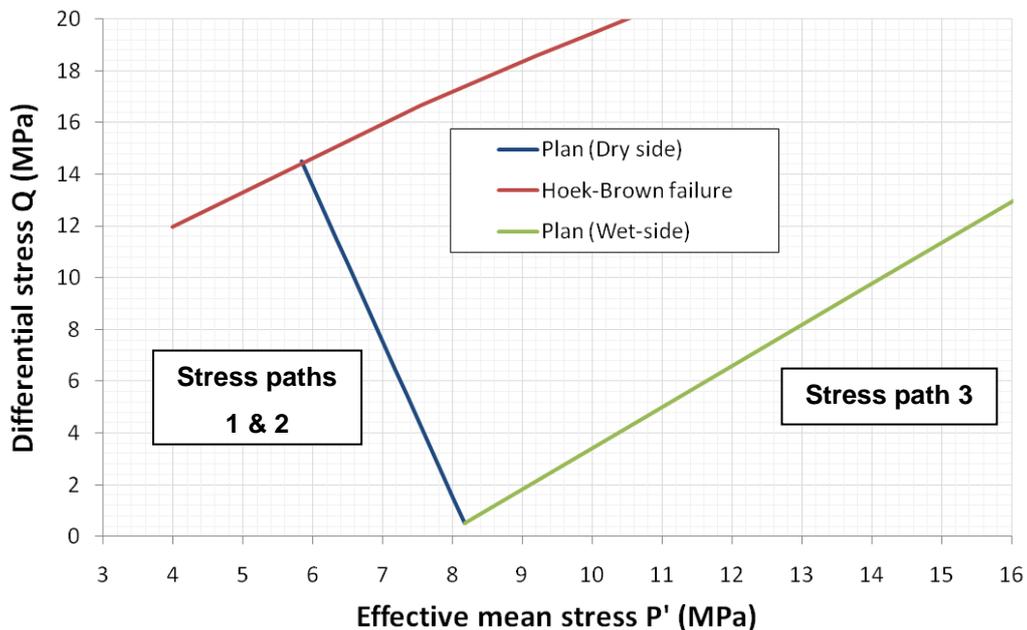
Figure 3-1 Hoek-Brown failure envelope as supplied by Andra and the BGS proposed stress paths.

3.1 STRESS PATH 1 - DRY SIDE DEFORMATION WITH NO POREWATER PRESSURE [TEST REPORTED IN THIS REPORT]

The first test (SPP_CoX-1) was performed with a constant pore-water pressure (drained) and was conducted relatively quickly. This stress-path simulated rapid stress changes during the

construction phase of a repository. Failure was achieved by simultaneously altering both confining pressure and load stress. The test was conducted as follows:

- Specimen was fully resaturated (S_w>0.99) while subject to the original conditions of effective (3D) stress.
- Simultaneous increments in both load and confining pressure were then applied to the specimen (while monitoring volume change) in order to achieve failure.
- Post-test analysis of the core was performed to examine fabric deformation along individual failure planes and to quantify the basic geotechnical properties of the remaining core.
- Full interpretation and modeling of the data (where appropriate) was undertaken.

The aim of this test was to define the location of the Hoek-Brown failure envelope through a number (>13) steps of short duration (3 – 7 days). This information was then used to select 4 – 5 steps for a much more detailed test (StressPath 2).

3.2   STRESS PATH 2 - DRY SIDE DEFORMATION WITH PORE PRESSURE

The second stress-path (test SPP_CoX-2) will be identical to that used in StressPath 1 (test SPP_CoX-1). Stress-path 2 will be driven at a much slower rate than for StressPath 1 with a pressure gradient between the injection and back-pressure filters to initiate flow and measure the evolution in transport properties. It is anticipated that four or five steps will be selected, pausing the stress path and measuring the permeability at key points of the test. This experiment will help to confirm whether or not permeability changes below the failure envelope and whether permeability begins to alter before any other mechanical indicator is observed. Two tests will be performed; one using an aqueous permeant and the other a gaseous one. The test will be conducted as follows:

- Specimen will be fully resaturated ($S_w > 0.99$) while subject to the original conditions of effective (3D) stress.
- The intrinsic permeability of the specimen will be measured by a combination of controlled flow rate and/or constant head methodologies using a synthetic groundwater solution.
- For gas testing: After a period of pore pressure equilibration, gas testing (using H_e as the permeant) will commence using a combination of controlled flow rate and/or constant pressure techniques until a steady stream of gas is observed, thereby determining the initial gas transport parameters.
- Simultaneous increments in both load and confining pressure will then be applied to the specimen (while monitoring volume change) in order to achieve failure.
- The intrinsic permeability of the specimen will be measured at each increment of stress in order to define the change in intrinsic permeability.
- Post-test analysis of the core will be performed to examine fabric deformation along individual failure planes and to quantify the basic geotechnical properties of the remaining core.
- For water testing: The location of any aqueous tracers which may have been used will be investigated at this time.
- Full interpretation and modeling of the data (where appropriate) will be undertaken.

The aim of these two experiments is to examine the role the stress path has on transport properties and defining the onset of any changes in permeability.

3.3   STRESS PATH 3 - WET SIDE DEFORMATION WITH POREWATER PRESSURE

If time permits, a third stress-path (test SPP_CoX-3) will be investigated in order to look at the long-term convergent deformation observed over much longer time scales; this will result in a stress path that induces wet-side deformation. This may result in significantly different processes and permeability evolution from that observed in StressPath 2. The test programme will be identical to that described for StressPath 2, but along a different stress path.

3.4   MODIFICATION TO THE TEST PROGRAMME

The results presented in Section 4 show that Callovo-Oxfordian claystone has a very pronounced time dependent component of deformation. This means that for large 55mm diameter samples it is necessary to have long duration steps of testing. It is anticipated that each step may be three months or more, meaning that each stress path test is likely to be much longer than a year in duration. This means that the five experiments originally proposed may be too ambitious under the time constraints of the FORGE programme. This report describes StressPath 1 test, which is important in order to define the onset of deformation; although this assumes that the CoX is homogeneous, any heterogeneity in the samples will result in a modification of the failure envelope. Following the completion of this test, priority will be given to gas testing of StressPath 2 & 3.

4 Test SPP_CoX-1

The first test, designated SPP_CoX-1, was a relatively quick test in order to determine the location of the Hoek-Brown failure envelope. The stress level at which failure occurs is important in the following gas experiment (SPP_CoX-2), which will follow the same stress path but with five detailed steps designed to observe the changes in permeability during deformation.

The sample was loaded into the SPP apparatus on the 5th May 2010. The axial ram pump was set to a low pressure of 250 kPa so that the ram piston came in contact with the sample end. The axial pump pressure was then increased to 500 kPa to ensure that the sample and pistons were in direct contact. The first stage of the experiment consisted of a swelling stage at a confining pressure of 11.5 MPa, axial load of 12.5 MPa and pore-water pressure of 4.5 MPa (see Table 4-4). In order to achieve these starting conditions eight steps were undertaken over a period of one hour:

1. Axial load of 3 MPa, confining pressure of 2 MPa

2. Axial load of 6 MPa, confining pressure of 5 MPa

3. Axial load of 8 MPa, confining pressure of 7 MPa

4. Introduction of pore-water pressure of 1 MPa to drain circuits (central filter first followed by outer guard rings). All circuits successfully drained.

5. Axial load of 10 MPa, confining pressure of 9 MPa

6. Pore pressure raised to 2 MPa

7. Axial load of 12.5 MPa, confining pressure of 11.5 MPa

8. Pore pressure raised to 4.5 MPa on both the injection and back pressure circuits.

The slow progression to the starting pressure meant that the sample was not overloaded or damaged; or at least damage was minimised. Once the starting stress had been achieved this was considered to be a time of zero.

Table 4-4 shows the test history. The supplied Hoek-Brown failure envelope shows that CoX should fail at a confining pressure of 5.5 MPa and axial load of 20 MPa (with 4.5 MPa porewater pressure); step 15 in Table 4-4. The designated stress-path has one additional stage to ensure that failure is achieved. The Andra document (Andra 2005[1,2]) shows that CoX has a variable strength. To ensure that failure is achieved steps $17 - 23$ will take the stress-path beyond the variability in strength for CoX. It is hoped that failure will occur prior to step 16 to deliver a continuous linear stress-path.

The original plan allowed three to four days per step. It was anticipated that steps could be progressed at 9am on Monday morning and 5:30pm on Thursday; approximately 3.5 days. This would allow two steps a week and a total test of 8 weeks. However, as will be shown, four days per step was not sufficient and after the first few steps it was decided to allow seven days per step. It should be noted that this time was insufficient, but was a balance between achieving equilibrium and completing the test within a satisfactory timescale.

Step	Confining pressure (MPa)	Pore Pressure (MPa)	Axial load (MPa)	Differential load (MPa)	Differential stress Q (MPa)	Effective mean stress P' (MPa)	Start time (day)	End time (day)
Swell	11.5	4.5	12.5	1.0	1.0	7.33	0	15.1
1	12.5	4.5	13.0	0.5	0.5	8.17	15.1	17.9
2	12.0	4.5	13.5	1.5	1.5	8.00	17.9	22.1
3	11.5	4.5	14.0	2.5	2.5	7.83	22.1	26.9
4	11.0	4.5	14.5	3.5	3.5	7.67	26.9	35.1
5	10.5	4.5	15.0	4.5	4.5	7.50	35.1	41
6	10.0	4.5	15.5	5.5	5.5	7.33	41.0	15.9
7	9.5	4.5	16.0	6.5	6.5	7.17	45.9	50.1
8	9.0	4.5	16.5	7.5	7.5	7.00	50.1	60.9
9	8.5	4.5	17.0	8.5	8.5	6.83	60.9	67.9
10	8.0	4.5	17.5	9.5	9.5	6.67	67.9	73.9
11	7.5	4.5	18.0	10.5	10.5	6.50	73.9	80.9
12	7.0	4.5	18.5	11.5	11.5	6.33	80.9	88.0
13	6.5	4.5	19.0	12.5	12.5	6.17	88.0	94.9
14	6.0	4.5	19.5	13.5	13.5	6.00	94.9	101.9
15	5.5	4.5	20.0	14.5	14.5	5.83	101.9	108.9
16	5.0	4.5	20.5	15.5	15.5	5.67	108.9	123.2

Table 4-4 Summary of experimental history for test SPP_CoX-1 showing step number, axial stress and confining stress. Stages in parenthesis denote stages that have not been conducted to date, stages in italics are deviations from the ideal stress path if the Hoek-Brown failure envelope is seen to be poorly defined.

4.1 SWELLING STAGE

The first step of testing lasted 15 days and was designed to allow the test to equilibrate with the synthetic porewater fluid and naturally swell. The system was setup with a confining pressure of 11.5 MPa, axial load of 12.5 MPa and porewater pressure of 4.5 MPa. The results of this stage can be seen in Figure 4-1. As shown in Figure 4-1a, the radial strain measurements of the sample deformation performed well. It can be seen that radial strain of the CoX sample is heterogeneous; with radial 1 showing the most deformation and recording more than twice the displacement seen of radial 2, which showed the least strain. Figure 4-1b compares the strains recorded (axial, radial and volumetric). It can be seen that the small strains recorded are comparable and confirm that the SPP apparatus performs well. The sign of the strain shows that the overall sample volume is increasing as the sample swelled.

Figure 4-1c shows the flow of the four ISCO pumps of the SPP apparatus (confining, axial, injection and back-pressure circuits). It can be seen that all four pumps took approximately 8 days to achieve the usual low flows (<5 µl/hr) expected for stable conditions. Initially the flow from the porewater pressure system shows an outflow of fluid. The asymptote of these curves suggest that the outflow of water is related to the time-dependent compression seen in the sample.

The two highlighted events (day 8.1 and day 10.95) correspond to a weekend where power to BGS Keyworth was shutdown and the laboratory was switched to a generator. This had a consequence on the air-conditioning in the environmental room of the laboratory, which can be seen to have an effect on the flow of the confining and axial flows. However, there is no indication of any effect on the test sample.

a

b

c
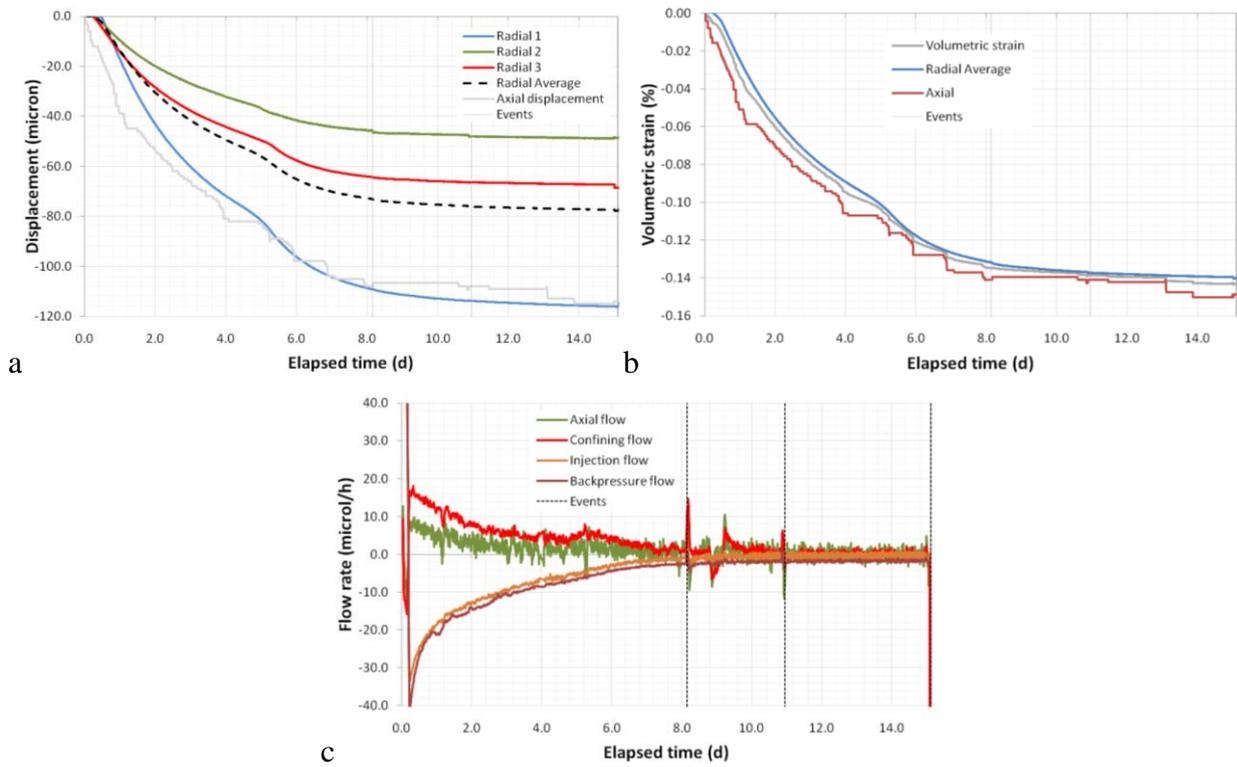
Figure 4-1 Swelling stage of the experiment. A) radial and axial displacements. B) Comparing strains. C) Flow of all four ISCO pumps during the swelling of the sample.

4.2 COMPLETE TEST HISTORY

Figure 4-2 shows the stress-path followed during the complete test history for SPP_CoX-1. As can be seen a straight stress-path has been achieved with 16 steps following the swelling stage up to failure, which resulted in deviation of the stress path. The position of the Hoek-Brown failure envelope shows the expected stress conditions for inducing failure.
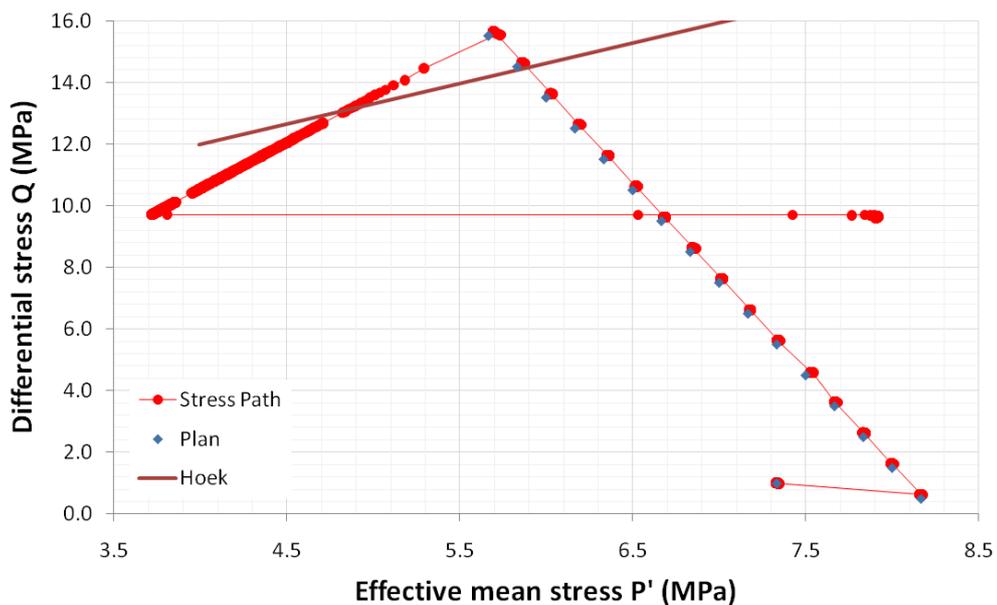
Figure 4-2 Stress path followed during test SPP_CoX-1.

35

4.2.1 Observations of strain measured directly

The SPP apparatus has been designed to more accurately measure the strain of the sample in the apparatus during deformation. Figure 4-3 shows the displacements of the axial and three radial displacement sensors. As can be seen, following the dilation of the sample during the swelling stage, the first step of the stress path resulted in time dependent contraction of the sample showing in all three radial displacements. The second step of testing shows very little displacement in the radial plane. From step 3 onwards (day 22.07), each successive step shows an increasing time-dependent characteristic with increasing dilation seen of the radial plane. The anisotropy seen in the radial displacements during swelling continues throughout the test history with radial 1 showing twice the displacement of radial 3.
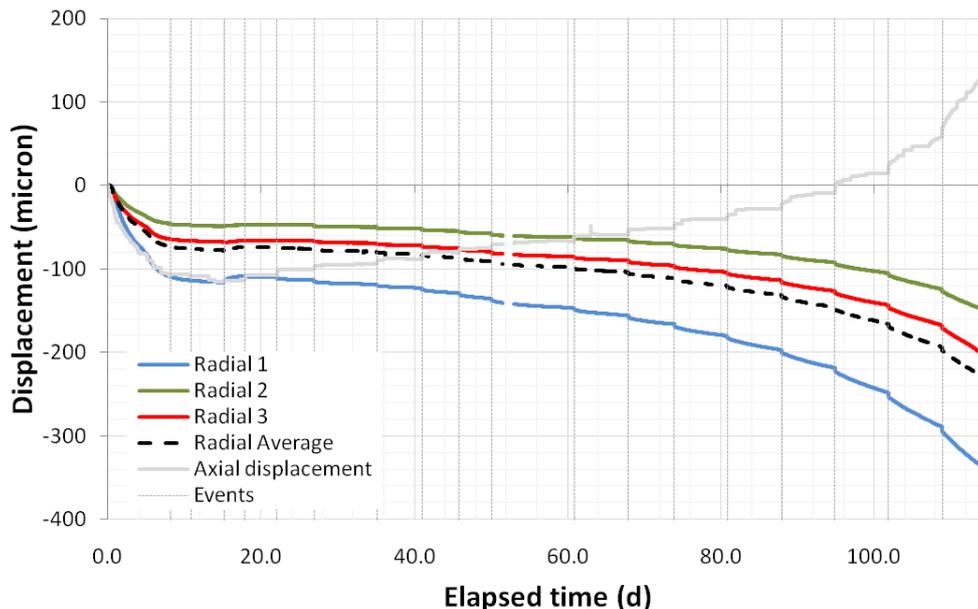
Figure 4-3 Axial and radial displacements measured during test SPP_CoX-1.

Following the swelling stage, where the sample was seen to lengthen, the overall change in axial displacement has been a sample shortening (see Figure 4-3 and Figure 4-4). The resolution of the axial displacement LVDT means that the detail is not as well defined as for radial displacements. The axial displacement setup is prone to "stick-slip", which is believed to be a characteristic of the apparatus and not representative of sample deformation. The axial measurement system is also more sensitive to temperature variations within the laboratory, as seen about day 63.

Figure 4-5 shows the strain recorded for the complete test history. Volumetric strain (ε_v) has been calculated from the average of the three radial strains (ε_{rad}) and axial strain (ε_{ax}) [$\varepsilon_v = 2\ \varepsilon_{rad} + \varepsilon_{ax}$]. Good agreement is seen between the strains recorded in the axial and radial directions during the swelling stage of the test, showing that swelling is homogeneous. The first two steps of the test resulted in an overall contraction of the sample volume. From stage three onwards it is seen that radial deformation dominates and that the overall sample volume increases.

It is evident that the recorded displacements are highly time-dependent. Figure 4-6a and Figure 4-6b show the time dependent nature of all displacements and average of radial displacement respectively. For each step change in the stress-path displacements have been reset to zero to highlight the time-dependency. As can be seen, step one and two are anomalous compared with the rest of the steps. During step 1 radial displacement shows that the sample contracts, while no change in axial displacement is seen. During step 2 very little time-dependent deformation is observed and the sample does not contract or expand in response to this stress change.
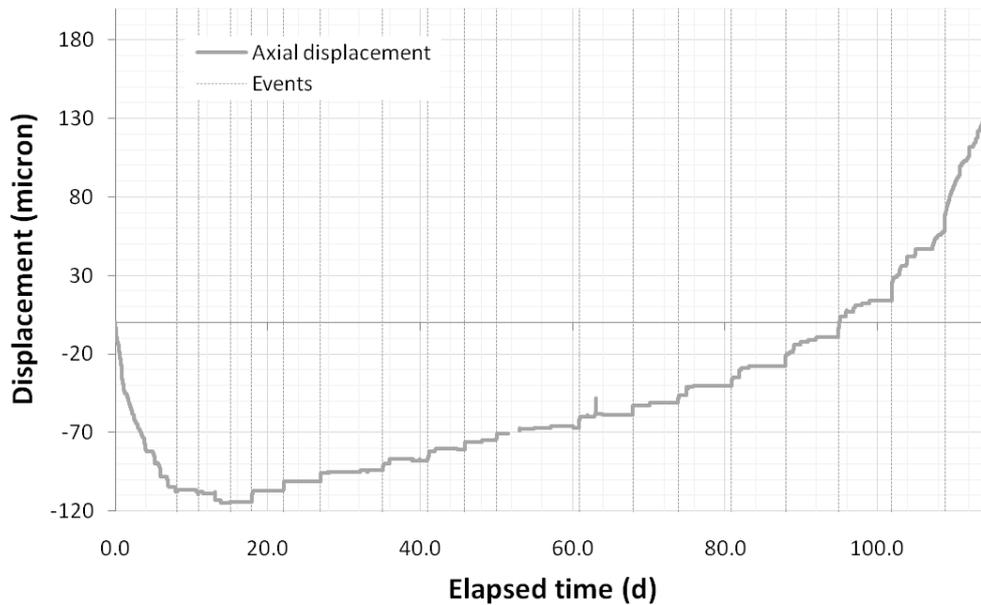
Figure 4-4 Axial displacement in more detail for test SPP_CoX-1.
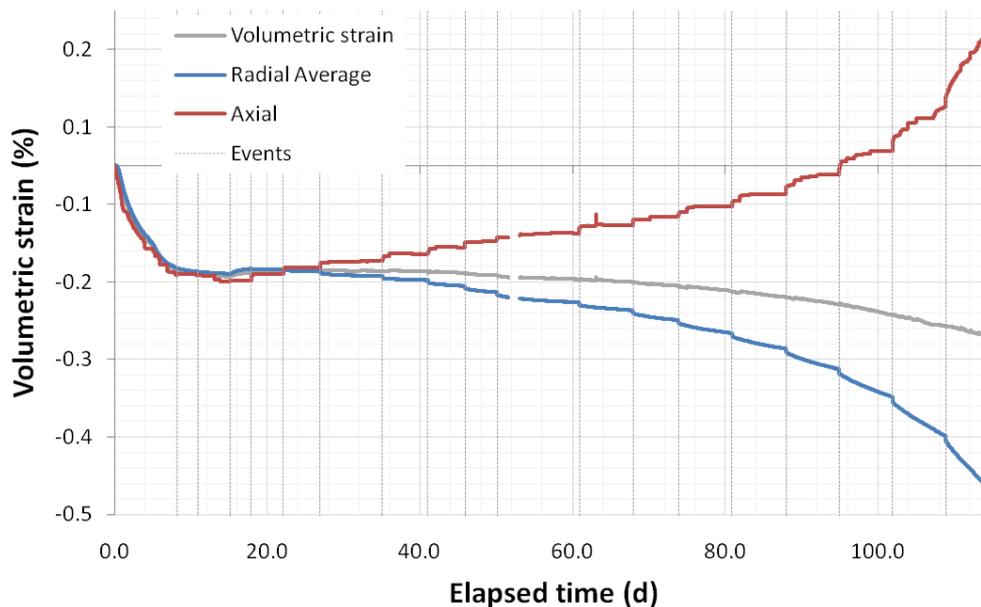
Figure 4-5 Strain observed during test SPP_CoX-1.

Following step 2, all consecutive steps are seen to have an increasing time-dependent component in radial displacement and consistent axial component. It can be clearly seen that asymptote had not been reached in any of the steps and would take a considerable time to be achieved.

Figure 4-6c shows the average radial displacement for all steps plotted as a function of the elapsed time of each step. This clearly shows that the time-dependent component of deformation generally increases as the stress-path develops. However, this not always the case; it was decided to hold step 7 for an increased 11 days to observe the influence this would have on the time-dependency. All steps up to 7 have an increasing curve; the extended duration of step 7 means that step 8 has a decreased curve. Steps 8 to 10 show increasing curves. This shows that the increasing curve is a consequence of the non-attainment of an asymptote, at least in part.

a).

b).

c).
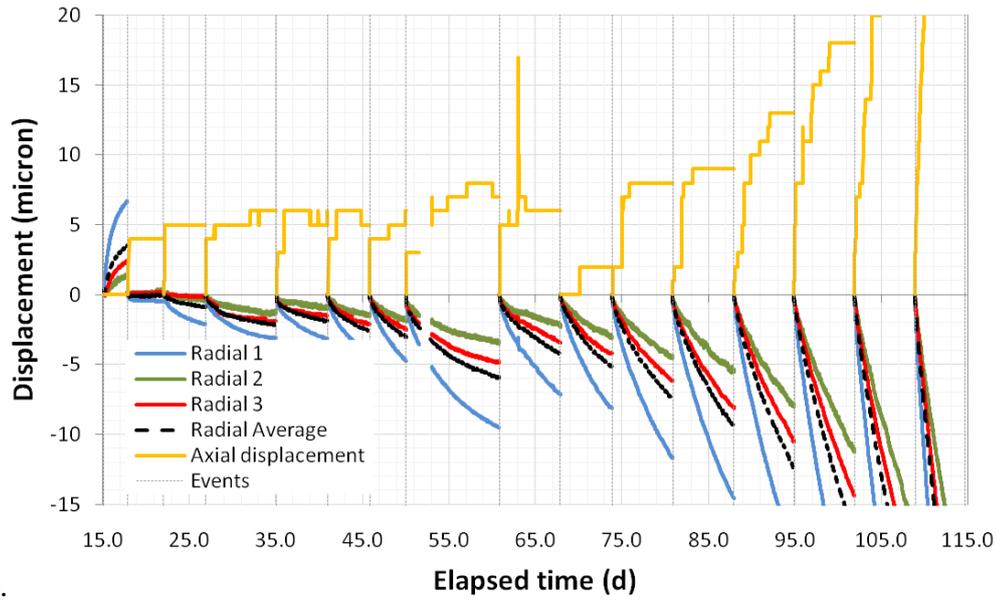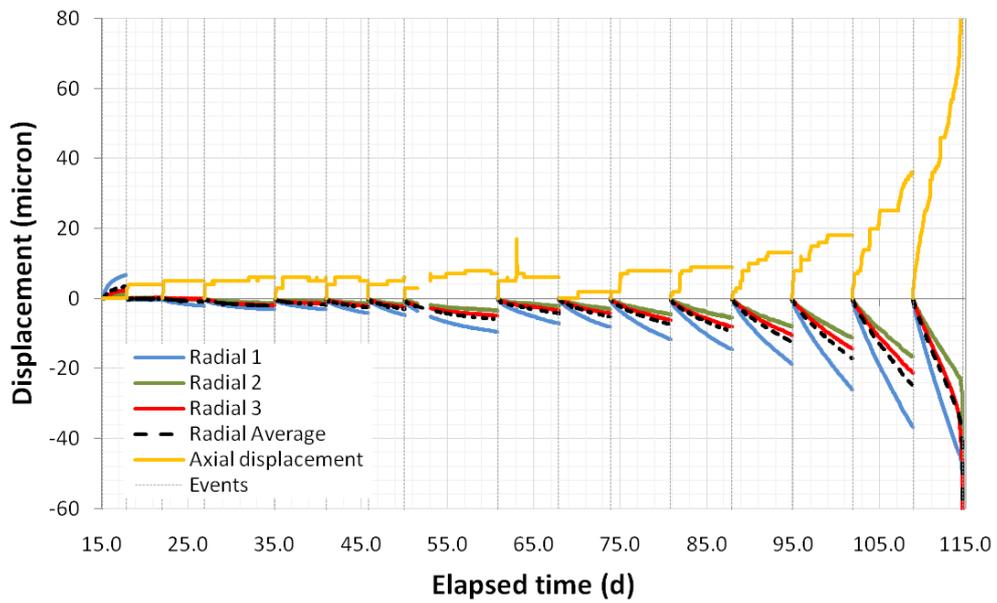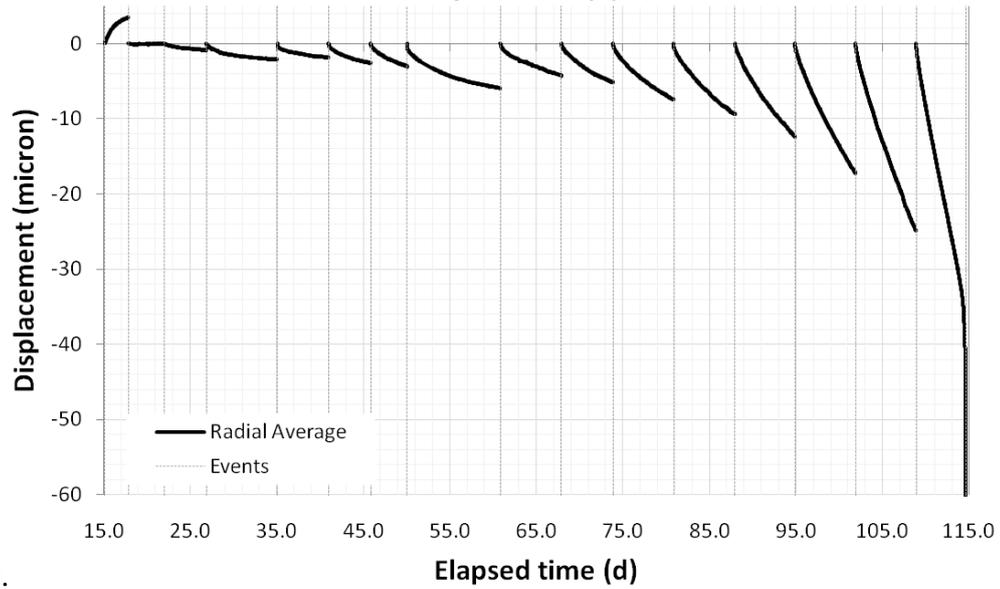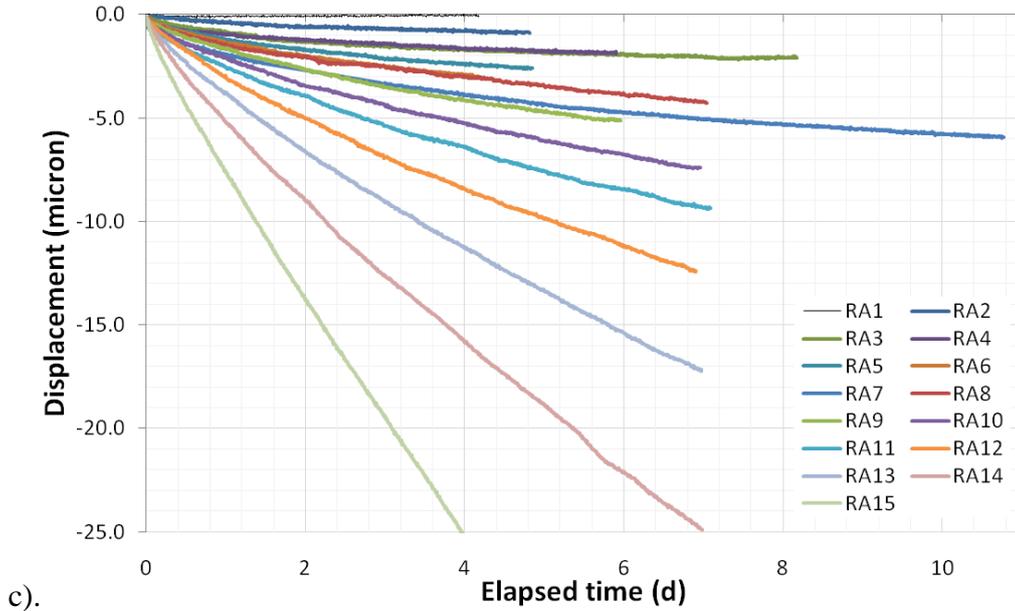
Figure 4-6 Radial displacement observed during test SPP_CoX-1. A) Time-dependent radial and axial displacement. B) Time-dependent average radial displacement. C) Time-dependent radial displacement for each step shown for the elapsed time of each step.

4.2.2 Observations of pump flow

Figure 4-6 shows the flow-rate of all four ISCO pumps that operate the SPP rig. As can be seen, all four pumps took approximately 10 days to equilibrate at the start of the test. The injection and backpressure flow systems showed an outflow as the sample swelled. This soon equilibrated to a low flow smaller than 5 μl/hr. It can be noted that axial flow, which generally has the greatest degree of "noise", becomes more noisy after a temperature fluctuation seen within the environmental room of the laboratory at day 62. Following this time, the temperature of the room was less stable than usual and this is reflected in the noisy flow data.
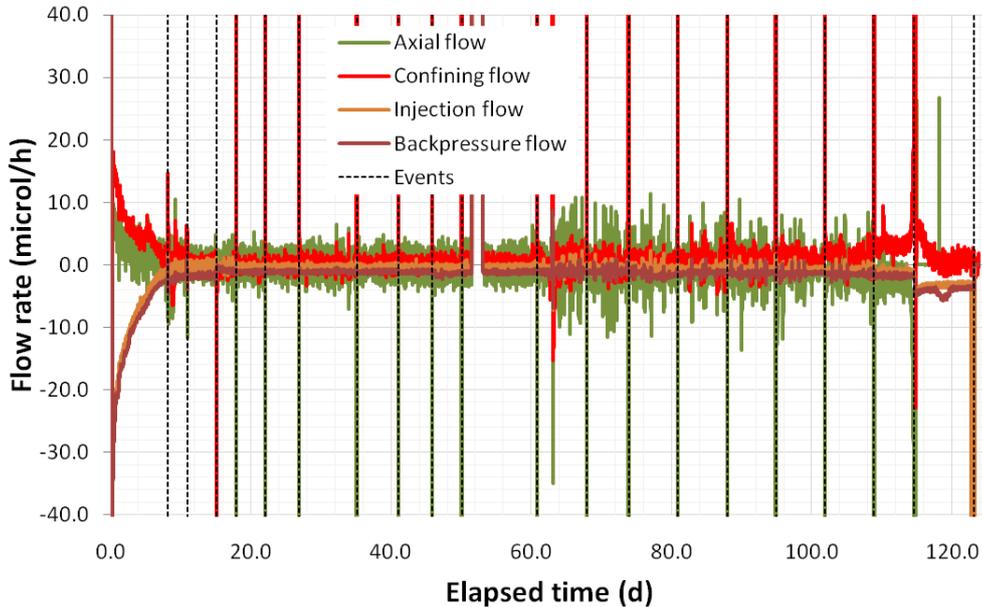
Figure 4-7 Flow rate of all four ISCO pumps used to operate the SPP.

39
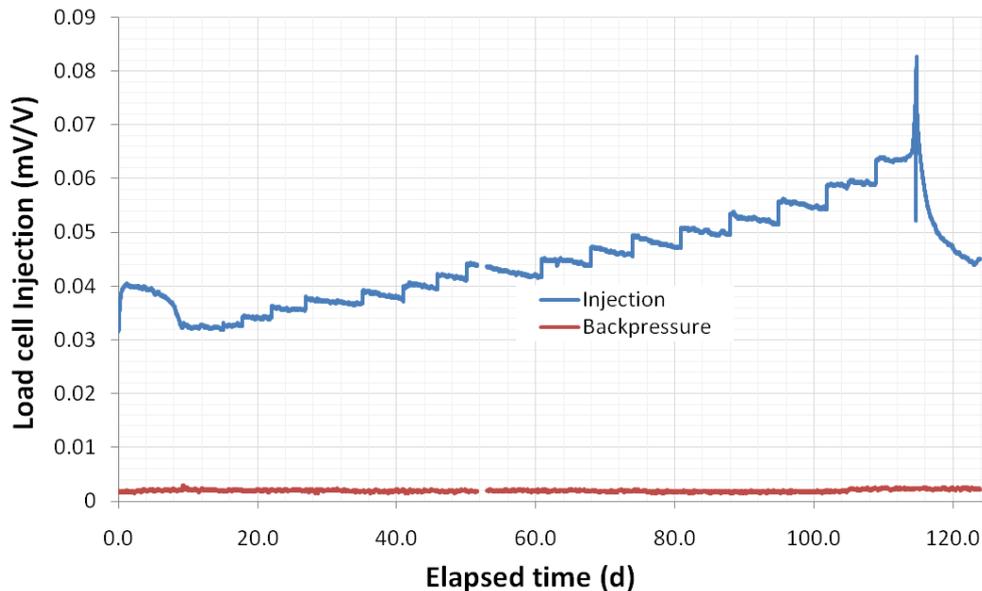
Figure 4-8 Result of axial load cells located at either end of the sample.

4.2.3 Observations of axial load cells

The SPP apparatus has two load cells located in both load platens and these are in direct contact with the sample. Figure 4-8 shows the result for the load cells; it should be noted that this is uncalibrated data in mV/V. It is immediatly obvious that the load cell of the backpressure system is not working. It is expected that the load cells would show a constant and stepped load in keeping with the constant load delivered by the axial load system. However, during the swelling phase of the experiment it can be seen that the load increased and then slowly decayed to the original starting load of 0.032 mV/V. The cause of this is not known. During the stress-path it can be seen that load has generally increased. However, this has occured in a "saw-tooth" manner, with each successive load increase being followed by a slow load decline. The cause of this feature is not known and may be associated with the time-dependent nature of fluid flow through the sample.

Following the completion of test SPP_CoX-1 the load cells will be calibrated and their behaviour in the presence of porewater will be investigated before starting test SPP_CoX-2G.

4.2.4 Observations of porewater pressure

Following the success of the guard-ring pore pressure sensors in the long-term test of CoX (Harrington *et al.*, 2010), pore pressure sensors were added to the injection and back pressure guard rings following the swelling phase of the experiment. It was not possible to calibrate the pressure sensors at that time, so the pressure that both sensors were recording were assumed to be the same as the pore pressure measured in the injection and back pressure pumps (4.5 MPa). Once the transducers were added to the circuit the guard rings were isolated. The pressure in the back pressure ring increased and peak 300 kPa above the pressure seen at the point of isolation. The injection circuit increased by over 1.5 MPa and peaked before decaying. The levels at which the pressure peaked may be the result of an incorrect assumption of pressure at the time of isolation and calibration of the sensors post-experiment will investigate this.
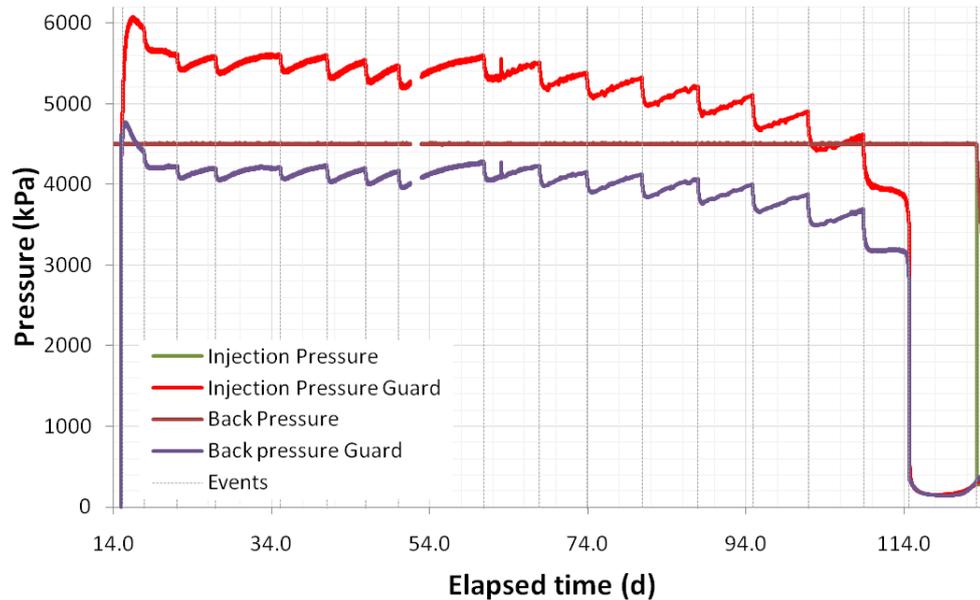
Figure 4-9 Results of the guard-ring porewater pressure during test SPP_CoX-1.

What can be seen is that from step 3 onwards (day 22.07) the behaviour of the guard-ring pressure has been consistent. For each pressure step confining pressure decreases and axial load increases, this results in a rapid lowering of pore pressure of 200 – 300 kPa over several hours, which is followed by a slow increase of pressure. In all steps it can be seen that the pore pressure had not reached asymptote and so it is not clear as to what level the pore pressure stabilises. It can be seen that as the time-dependent strain becomes more pronounced this is resulting in longer times for pore pressure to equilibrate. It is an interesting observation that pore pressure initially drops as axial load increases and confining pressure decreases. This could be the result of pore fluid being drawn into the sample by dilation, or possibly into the guard ring itself. The lowering of confining pressure may be resulting in the expansion of volume of available pore space between the sample and the jacket, resulting in a pressure drop. Therefore the exact cause of this pressure response is unclear.

4.2.5 Observations of temperature

The temperature within the environmental room of the laboratory has been kept within the specified ± 0.5º C throughout the experiment. There have been two temperature spikes caused by maintenance of the air-conditioning unit of the laboratory at day 9 and 62. The latter of these has caused fluctuations in axial displacement and following this time the variation of temperature has become slightly noisy. It should e noted that the greatest variation is observed in the SPP vessel and not the laboratory room. This suggests that one or more of the ISCO pumps is operating more regularly and that this is generating localised heat. The temperature fluctuations are not deemed to be problematic.
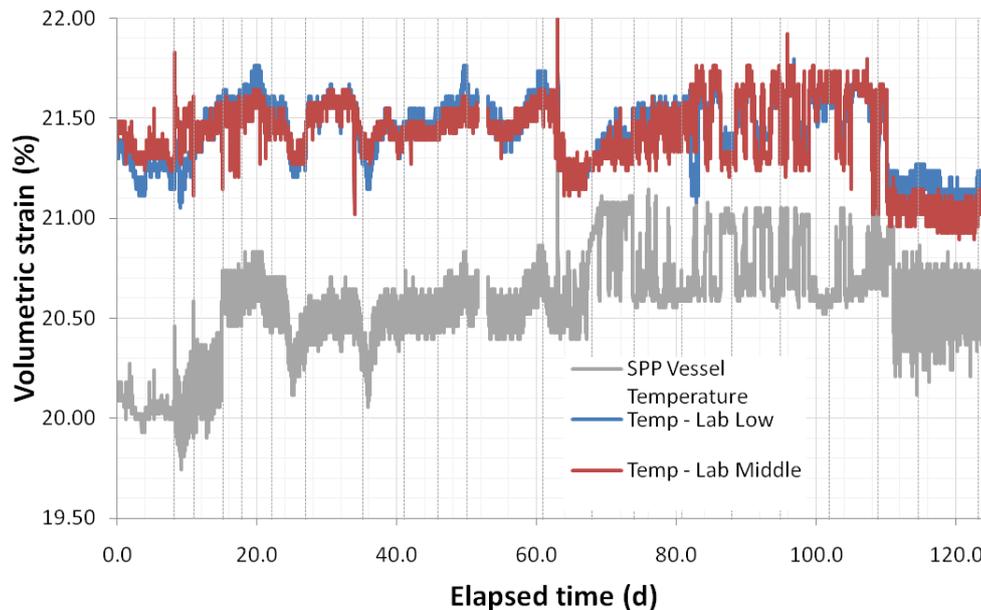
Figure 4-10 Temperature within the environmental room of the TPRL during test SPP_CoX-1.

4.3 INDIVIDUAL TEST STAGES

The general observations of Section 4.2 will be further expanded upon with this section for observations of each individual test stage.

4.3.1 Step 1; Day 15.1 – 17.9; σ_1 = 13.0 MPa, $\sigma_{2,3}$ = 12.5 MPa

The first step of the stress path began at day 15.1 and lasted nearly 3 days; the results are shown in Figure 4-11. As can be seen in Figure 4-11b, there was no recorded axial displacement during this stage of deformation, whereas axial displacements were all showing that the sample was contracting. Considerable heterogeneity is observed in radial displacement with 6.7, 2.4 and 1.4 µm of displacement occurring in Radial 1, 3 and 2 respectively. Figure 4-11c shows the average radial displacement. This shows that initially sample contraction was linear and after 0.6 days slowly decreased. The nature of the curvature suggests that an asymptote might have been reached if the step was continued for a further 4 or 5 days. Figure 4-11d shows the evolution of pore pressure within the guard-rings. The back-pressure guard ring can be seen to evolve much more quickly than the injection one. A peak in pressure is achieved in less than 0.5 days for the back-pressure system, compared with approximately 1.5 days for the injection side. It can also be seen that the back-pressure reduced at a much faster rate the injection side once peak had been achieved. The reason for these differences is unclear.
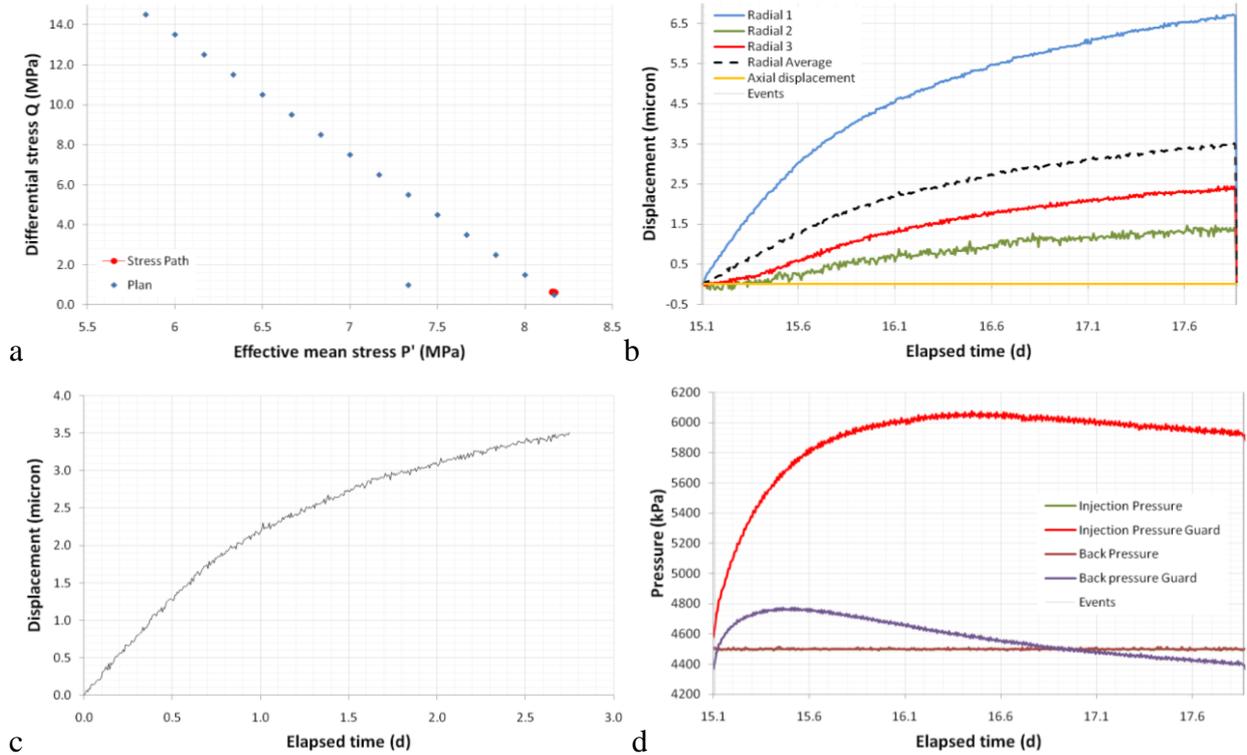
Figure 4-11 Results for step 1 of test SPP_CoX-1. A). Location of the stress-path. B) Axial and radial displacement results. C) Average radial displacement. D) Evolution of porewater pressure in the guard ring assembly.
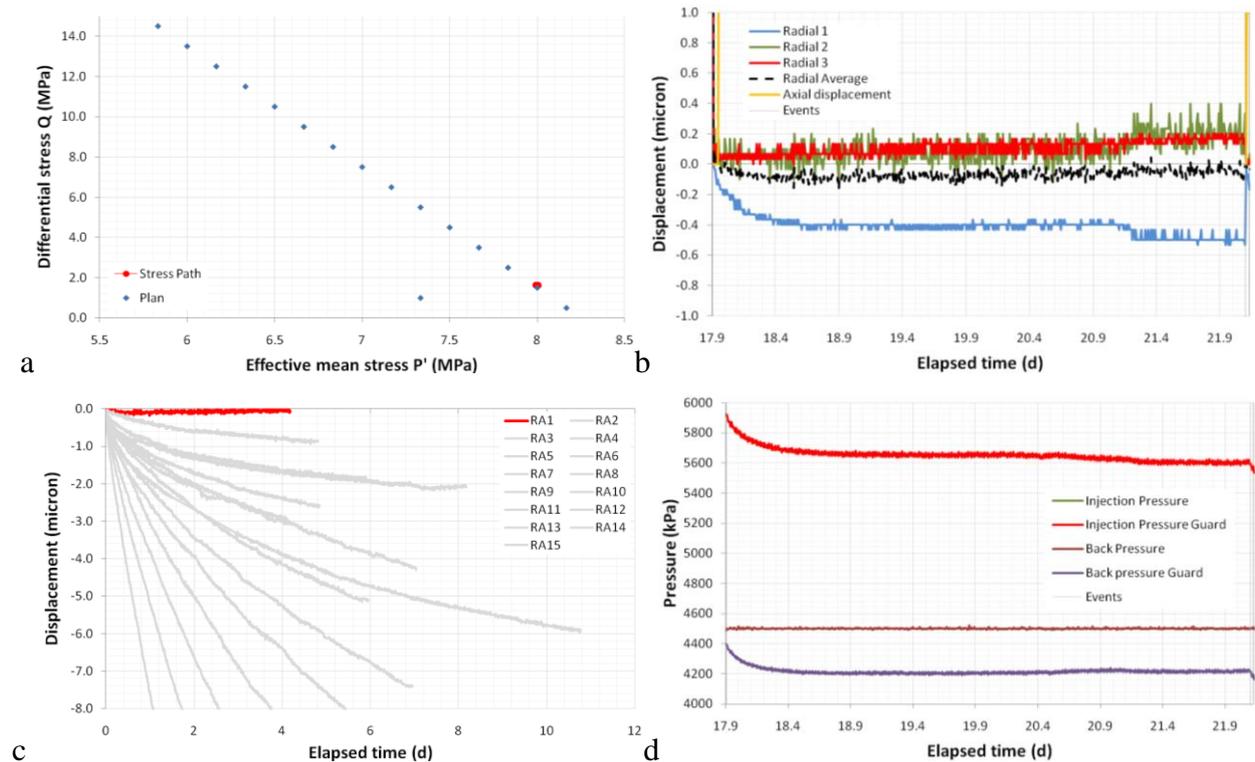
Figure 4-12 Results for step 2 of test SPP_CoX-1. A). Location of the stress-path. B) Axial Radial displacement results. C) Average radial displacement in comparison to other test steps. D) Evolution of porewater pressure in the guard ring assembly.

4.3.2 Step 2; Day 17.9 – 22.1; σ_1 = 13.5 MPa, $\sigma_{2,3}$ = 12.0 MPa

Step 2 of the stress path lasted approximately 4.2 days and gave some interesting results, as seen in Figure 4-12. The change in stress state resulted in stable deformation, with little time-dependency observed during the stage (see Figure 4-12b). It can even be seen that the observed anisotropy of the radial displacement means that radial 1 has resulted in dilational time-dependency, whereas radial 2 and 3 have resulted in contractional time-dependency. Generally it can be observed that average radial displacement is close to zero during this stage. The apparent lack of significant time-dependent deformation results in a rapid loss in guard-ring pore pressure (Figure 4-12d), which is followed by a gradual decline in pressure. This is in contrast to the observations of subsequent stages.

4.3.3 Step 3; Day 22.1 – 26.9; σ_1 = 14.0 MPa, $\sigma_{2,3}$ = 11.5 MPa

The third step of the stress-path lasted nearly five days and the results are shown in Figure 4-13. It can be seen that this step is the first to show considerable time-dependent radial deformation in a dilatational sense. As with the previous stage, considerable anisotropy is observed (Figure 4-13b), with time-dependent displacements of 2.1, 0.3 and 0.1 µm in radial 1, 2 and 3 respectively. The average of radial displacement can be seen to not have achieved asymptote and would have taken considerable time to reach that state. The evolution of pore pressure within the guard-rings (Figure 4-13d) shows that over the first 0.5 days of the stage the pore pressure in both injection and back-pressure guard rings decreased by approximately 200 kPa and for the remainder of the stage slowly increased to a level similar to that at the start of the stage. The fact that pore pressure increased during this stage and did not in the previous step suggests that there is a connection between the time dependency seen in radial deformation and pore pressure. It is uncertain whether the time dependent flow of fluid is resulting in a component of creep in deformation, or if the creep is causing the porewater to flow.
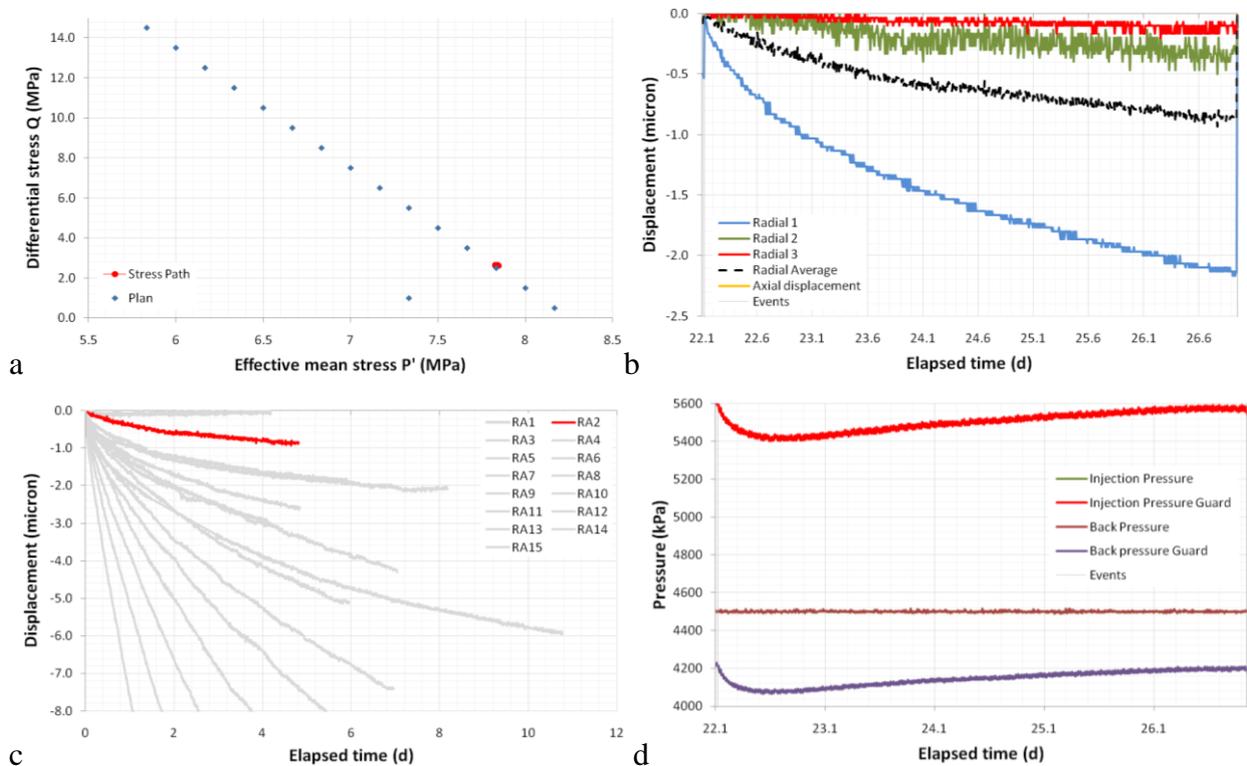
Figure 4-13 Results for step 3 of test SPP_CoX-1. A). Location of the stress-path. B) Radial displacement results. C) Average radial displacement in comparison to other test steps. D) Evolution of porewater pressure in the guard ring assembly.

4.3.4   Step 4; Day 26.9 – 35.1; σ_1 = 14.5 MPa, $\sigma_{2,3}$ = 11.0 MPa

The forth step of the stress path was run for 8 days and the results are shown in Figure 4-14. It can be seen that once again time-dependency is seen in radial displacement, but in contrast to the previous step the degree of anisotropy has reduced; by the end of the step radial displacements were 3.1, 1.9 and 1.3 μm for radial 1, 3 and 2 respectively (Figure 4-14b). Radial 3 showed an anomalous result during this step, a behaviour that had not been seen in previous steps. At day 28.2 a step change in radial displacement was observed and at day 33.7 another step-change occurred; however, this step was less instantaneous than the first. It can be seen the length of the stage meant that asymptote of displacement had been achieved. The evolution of pore pressure (Figure 4-14d) also reached asymptote. As with the previous step, the first 0.5 days showed a gradual pressure decline of approximately 200 kPa; which was followed by a slow recovery. The porewater pressure in both the injection and back-pressure guard rings recovered to the same level as at the start of the stage. This suggests that the time-dependency is of the order of 7 – 14 days in length and is not an indication of long-term creep.
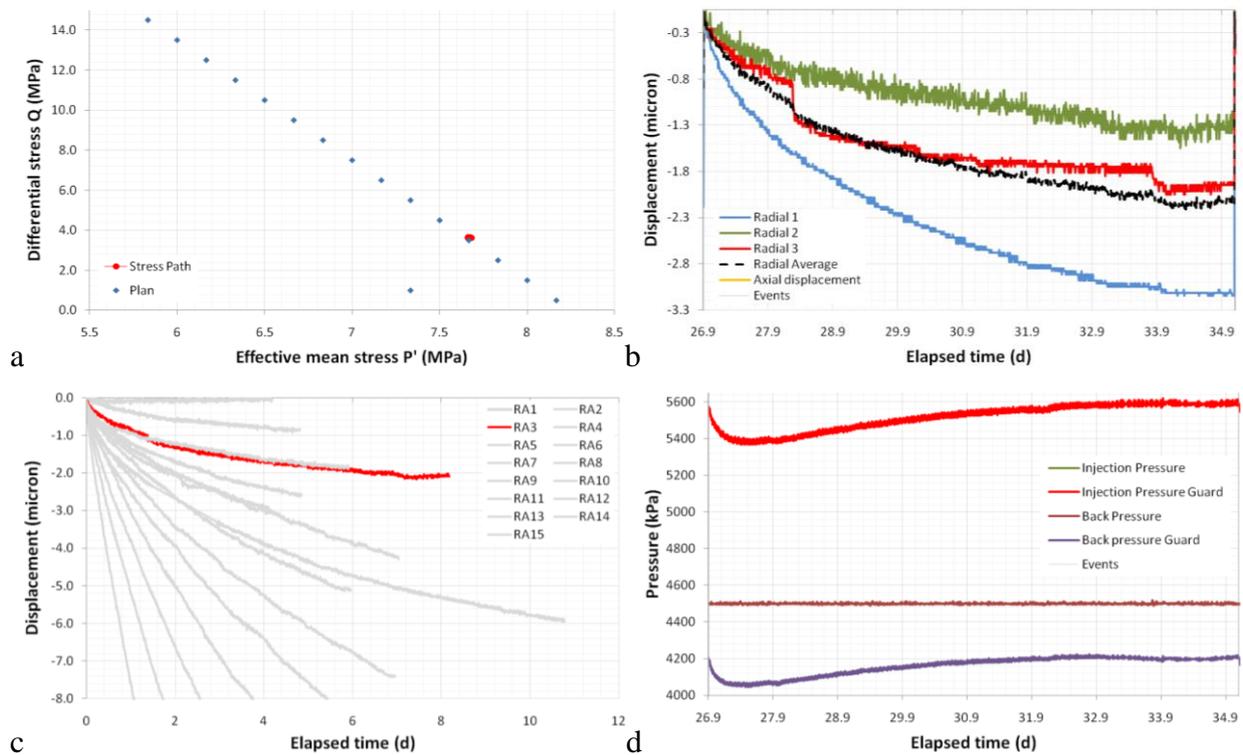
Figure 4-14   Results for step 4 of test SPP_CoX-1. A). Location of the stress-path. B) Radial displacement results. C) Average radial displacement in comparison to other test steps. D) Evolution of porewater pressure in the guard ring assembly.

4.3.5   Step 5; Day 35.1 – 41.0; σ_1 = 15.0 MPa, $\sigma_{2,3}$ = 10.5 MPa

The fifth stage was approximately 6 days long and the results are shown in Figure 4-15. The behaviour of radial 3 displacement was similar in this stage as to step 4 with three step changes. It may be observed that a step change has occurred in radial 1, although this is less clear. As with previous steps, considerable anistropy is observed with radial displacement of 3.2, 1.5 and 0.9 µm of displacement in radial 1, 3 and 2 respectively (see Figure 4-15b). It can be seen that asymptote has not been achieved by the end of the step and it could be a considerable time until radial 1 reaches steady state. Figure 4-15c shows a very important result. It can be seen that the time-dependent deformation of radial displacement plots on top of the previous step. This suggests that a certain amount of the time dependent deformation is as a result of the slow expulsion of fluid from the sample. If asymptote is not achieved then the next step has a greater curvature. This suggests that the time-dependent deformation is created by slow fluid expulsion as well as creep of the CoX.

a

b

c
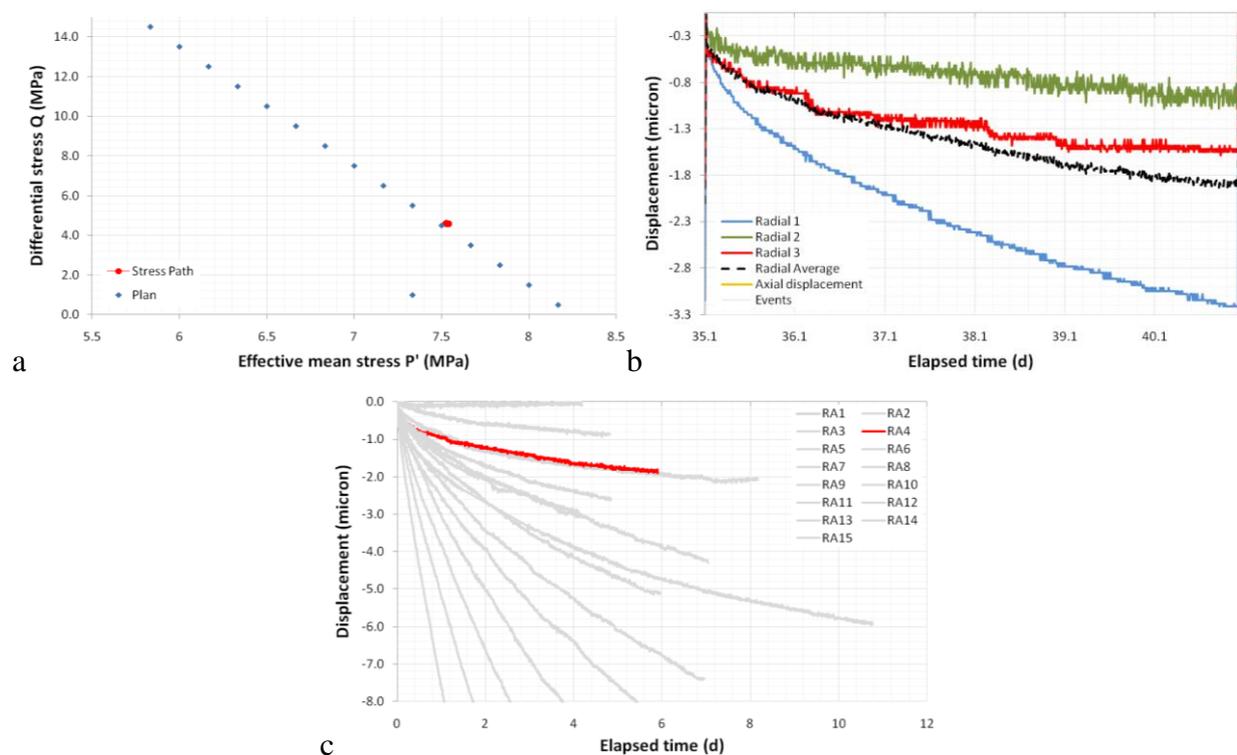
Figure 4-15   Results for step 5 of test SPP_CoX-1. A). Location of the stress-path. B) Radial displacement results. C) Average radial displacement in comparison to other test steps.

Step 6; Day 41.0 – 45.9; σ_1 = 15.5 MPa, $\sigma_{2,3}$ = 10.0 MPa

The sixth stage was approximately 4 days long and the results are shown in Figure 4-16. As with the previous two steps, radial displacement 1 shows a step change. Overall the sample shows considerable anisotropy with 4.2, 2.1 and 1.4 µm of displacement in radial 1, 3 and 2 respectively (see Figure 4-16b). Figure 4-16c shows that the curvature of time-dependent displacement has increased compared with the previous step, which strengthens the hypothesis that if asymptote is not achieved it influences the following step. Figure 4-16d shows the evolution of porewater pressure in the guardrings and as with previous steps, showed a 300 kPa drop in the first 0.5 days, followed by a slow recovery. By the end of the step the two pressure transducers are approximately 50 – 100 kPa below their starting level.
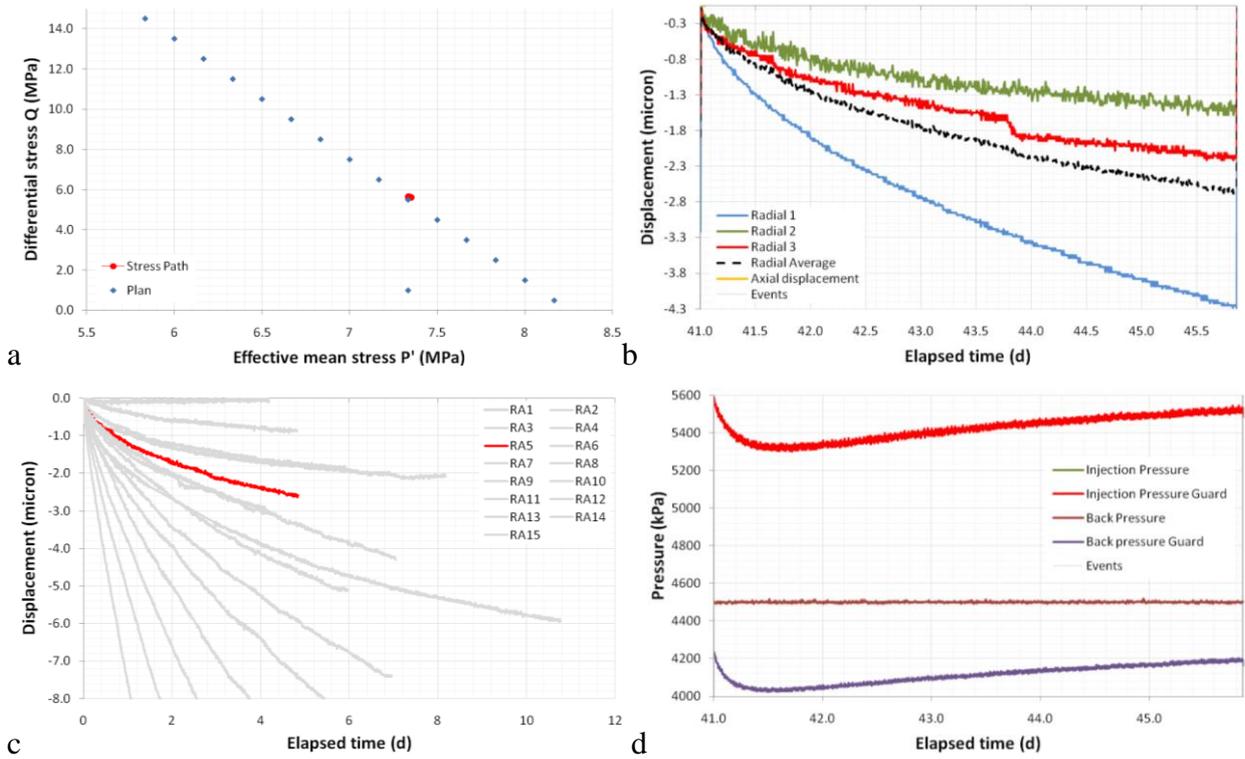
Figure 4-16 Results for step 6 of test SPP_CoX-1. A). Location of the stress-path. B) Radial displacement results. C) Average radial displacement in comparison to other test steps. D) Evolution of porewater pressure in the guard ring assembly.
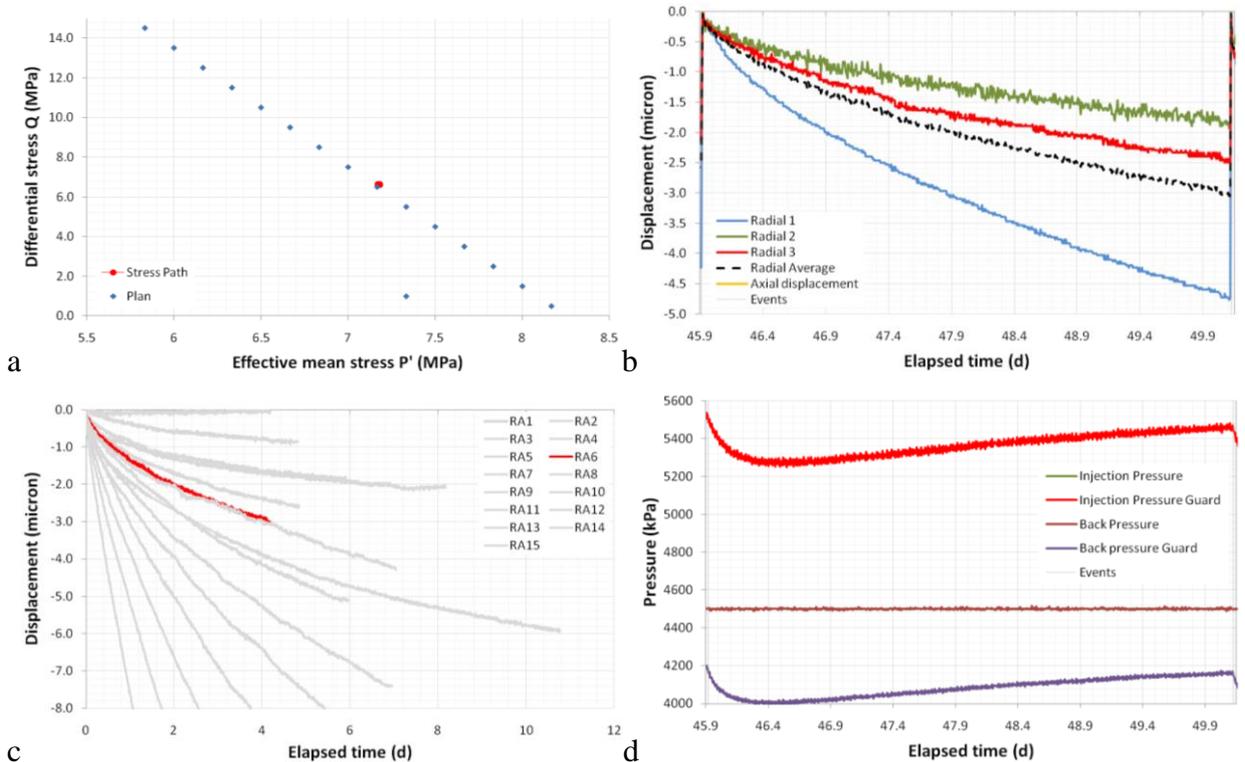
Figure 4-17 Results for step 7 of test SPP_CoX-1. A). Location of the stress-path. B) Radial displacement results. C) Average radial displacement in comparison to other test steps. D) Evolution of porewater pressure in the guard ring assembly.

4.3.6 Step 7; Day 45.9 – 50.1; σ_1 = 16.0 MPa, $\sigma_{2,3}$ = 9.5 MPa

The seventh stage was approximately 4 days long and the results are shown in Figure 4-17. It can be seen that no stepped changes in radial 3 occurred, but anisotropy has continued in radial

displacement (see Figure 4-17b) with 4.7, 2.5 and 1.9 µm of displacement in radial 1, 3, and 2 respectively. Figure 4-17c shows that step 7 has an increased slope compared to step 6. The evolution of porewater pressure shows similar results to the previous steps, with 200 kPa loss in back pressure and 300 kPa in injection (Figure 4-17d). At the end of the stage the porewater pressure had still not recovered and was approximately 50 kPa lower than when the step began.

4.3.7 Step 8; Day 50.1 – 60.9; σ_1 = 16.5 MPa, $\sigma_{2,3}$ = 9.0 MPa

The eighth stage was approximately 11 days long and the results are shown in Figure 4-18. This step was prolonged so that full asymptote and steady state was achieved. However,as the results show even after 11 days the sample was far from reaching steady state. As seen in Figure 4-18 there was a problem with the logging computer which failed to log data for approximately two days; this had no effect on the experiment and is just a loss of data logging. Figure 4-18b shows that the sample showed time-dependency in radial displacement and considerable anisotropy, with 9.5, 4.8 and 3.4 µm of displacement in radial 1, 3 and 2 respectively. Figure 4-18c shows that the curvature of time-dependency for step 8 has increased since step 7 and that symptote has not been achieved, and would not be reached with 5 – 7 days. Figure 4-18d shows the evolution of porewater pressure in the guardrings. Common to the previous steps a 200 kPa drop is seen within 0.5 days, followed by a slow recovery. As this step was much longer than the previous step the pore pressure at the end of the step is greater than at the start in both injection and back pressure guard rings. This is because of the failure to reach asymptote and full recovery of the previous steps.
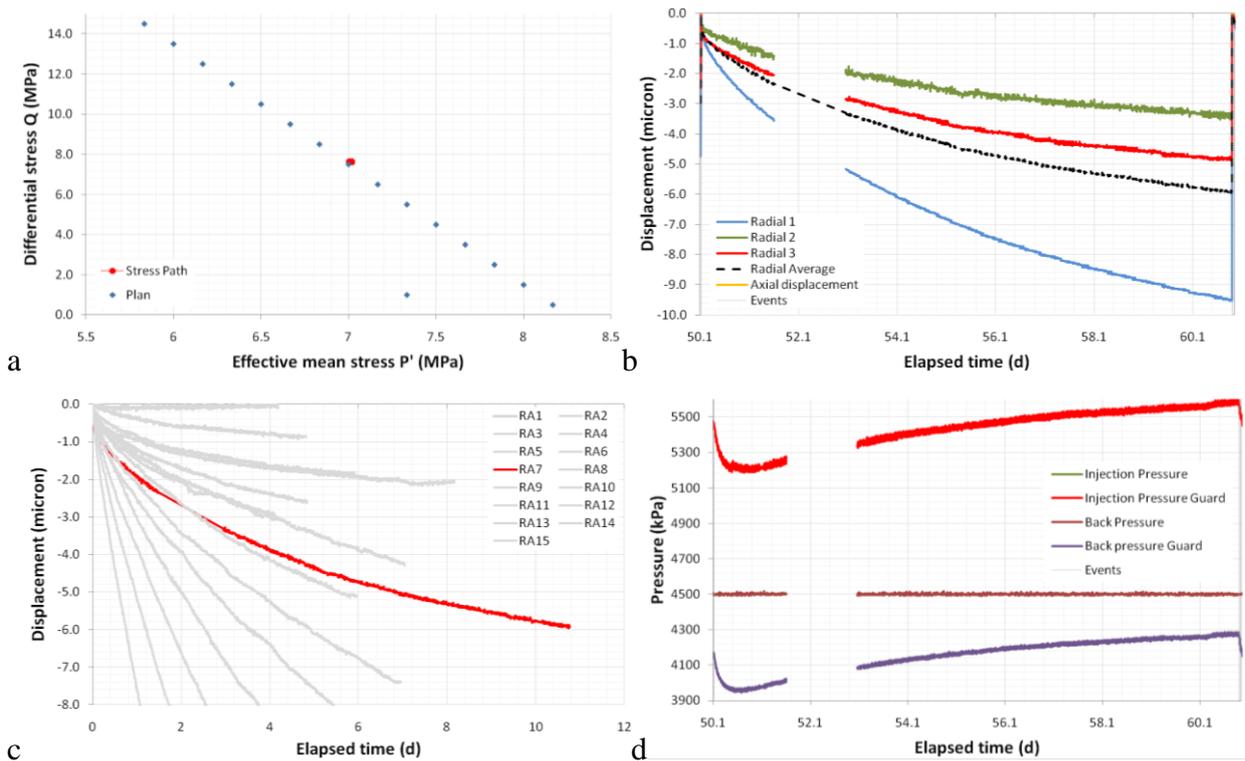
Figure 4-18   Results for step 8 of test SPP_CoX-1. A). Location of the stress-path. B) Radial displacement results. C) Average radial displacement in comparison to other test steps. D) Evolution of porewater pressure in the guard ring assembly.

4.3.8 Step 9; Day 60.9 – 67.9; σ_1 = 17.0 MPa, $\sigma_{2,3}$ = 8.5 MPa

The nineth stage was approximately 7 days long and the results are shown in Figure 4-19. The data for step 9 when compared to the previous steps shows much less stability following a temperature spike of 1° C at day 63.1. The variation in temperature of the pressure vessel has influenced many of the recorded channels. The temperature spike has effected the radial displacement readings. It is noted that radial 1 shows a positive influence, but radial 2 and 3 both

show a negative spike (Figure 4-19b). Radial displacement had not reached asymptote by the end of the step and show anisotropy. Radial 1, 2 and 3 show 7.1, 2.3, and 3.5 μm of displacement respectively. Figure 4-19c shows that the curvature of the time-dependent displacement has reduced following the extended operation of the previous step. The curvature has resulted in the same level as step 7.
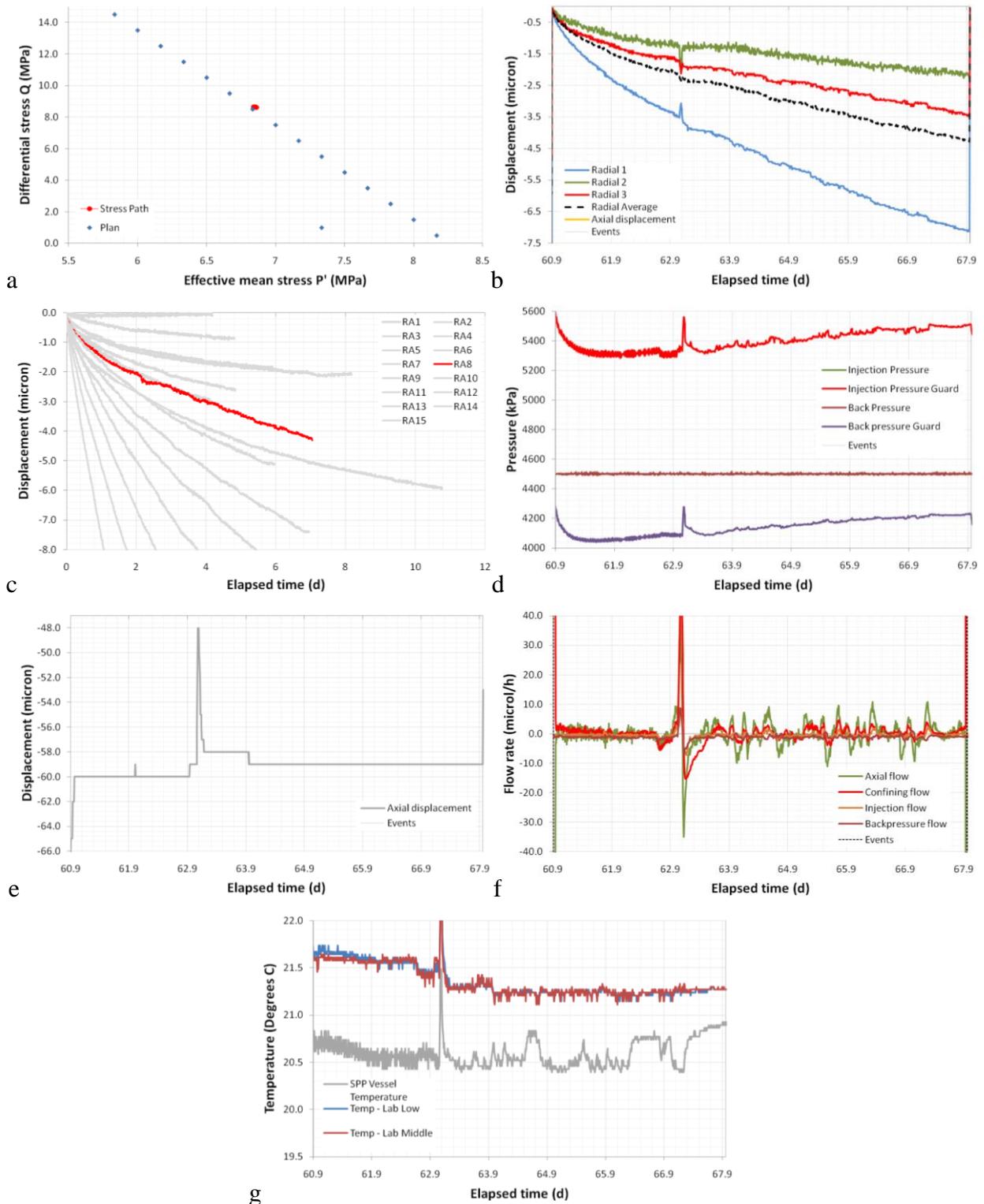
Figure 4-19   Results for step 9 of test SPP_CoX-1. A). Location of the stress-path. B) Radial displacement results. C) Average radial displacement in comparison to other test steps. D) Evolution of porewater pressure in the guard ring assembly. E) Axial displacement. F) Flow rate of all four ISCO pumps. G). Laboratory temperature.

49

The evolution of porewater pressure in the guardrings (Figure 4-19d) shows similar behaviour as the previous steps. A 200 kPa drop occurred in the first 0.5 days of the step, followed by a slow recovery. The pressure of the guardrings was affected by the temperature disturbance and the result following this time is not as steady as previously achieved. Figure 4-19e and f shpw the influence the temperature disturbance has had on axial displacement and flow respectively.

4.3.9   Step 10; Day 67.9 – 73.9; σ_1 = 17.5 MPa, $\sigma_{2,3}$ = 8.0 MPa

The tenth stage was approximately 6 days long and the results are shown in Figure 4-20. All channels show similar results to previous steps. Considerable anisotropy is seen in radial displacement with 8.1, 4.2 and 3.1 μm of displacement seen in radial 1, 3 and 2 respectively. Figure 4-20c shows that the curvature of displacement for step 10 has increased in comparison with step 9. The evolution of porewater pressure in the guardrings (Figure 4-20d) shows the characteristic pressure drop followed by pressure recovery. Figure 4-20e shows the result for laboratory temperature which shows instability in SPP vessel temperature. The variations in temperature correlate with disturbances seen in guard pressures and radial displacements.
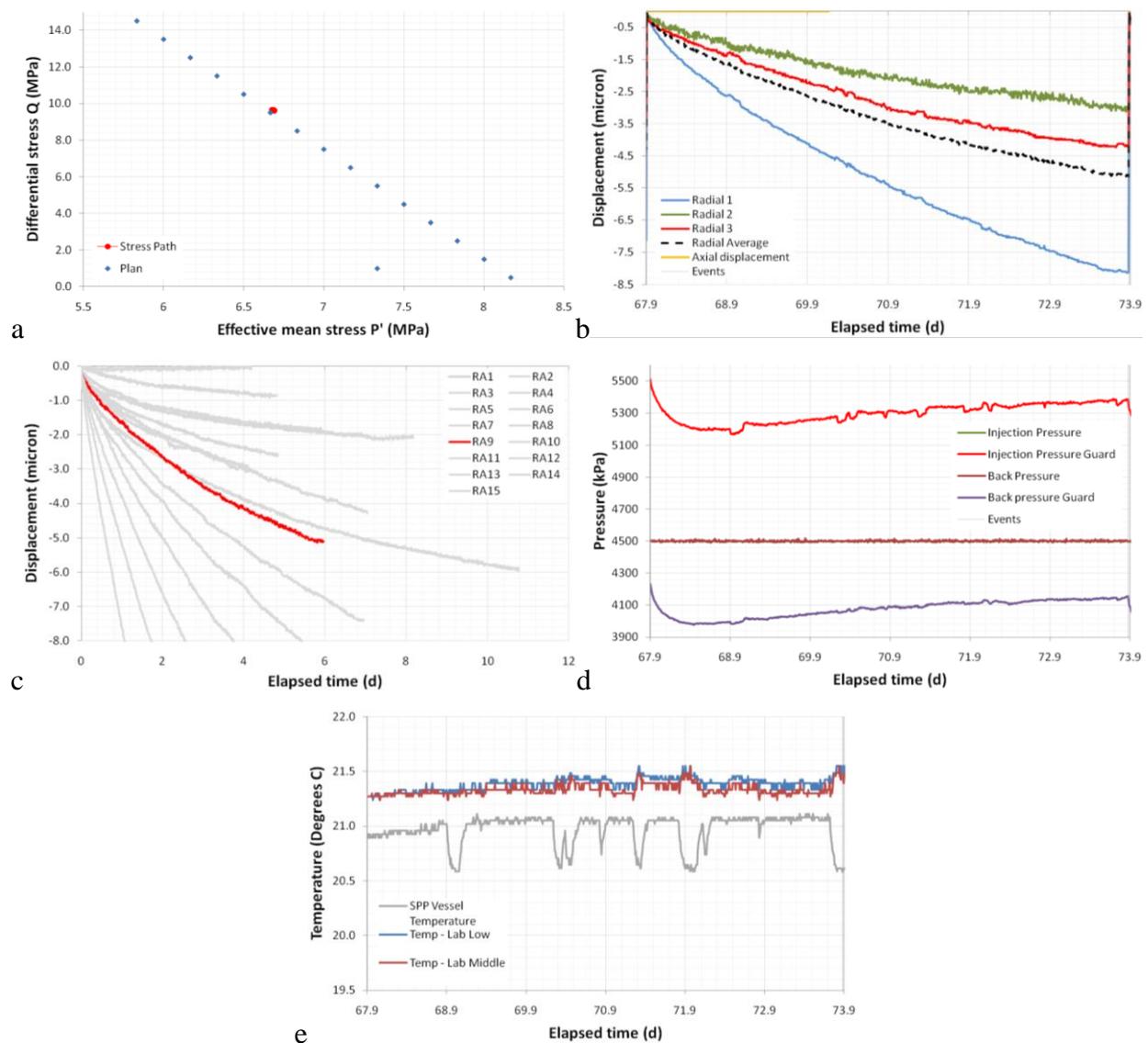
Figure 4-20   Results for step 10 of test SPP_CoX-1. A). Location of the stress-path. B) Radial displacement results. C) Average radial displacement in comparison to other test steps. D) Evolution of porewater pressure in the guard ring assembly. E) Temperature readings within the laboratory.

4.3.10 Step 11; Day 73.9 – 80.9; σ_1 = 18.0 MPa, $\sigma_{2,3}$ = 7.5 MPa

The eleventh stage was approximately 7 days long and the results are shown in Figure 4-21. All channels show similar results to previous steps. Considerable anisotropy is seen in radial displacement with 11.7, 6.1 and 4.5 µm of displacement seen in radial 1, 3 and 2 respectively (Figure 4-21b). Figure 4-21c shows that the curvature of displacement for step 11 has increased in comparison with step 10. The evolution of porewater pressure in the guardrings (Figure 4-21d) shows the characteristic pressure drop followed by pressure recovery. As with previous steps, the porewater pressure had not fully recovered and had not reached asymptote.
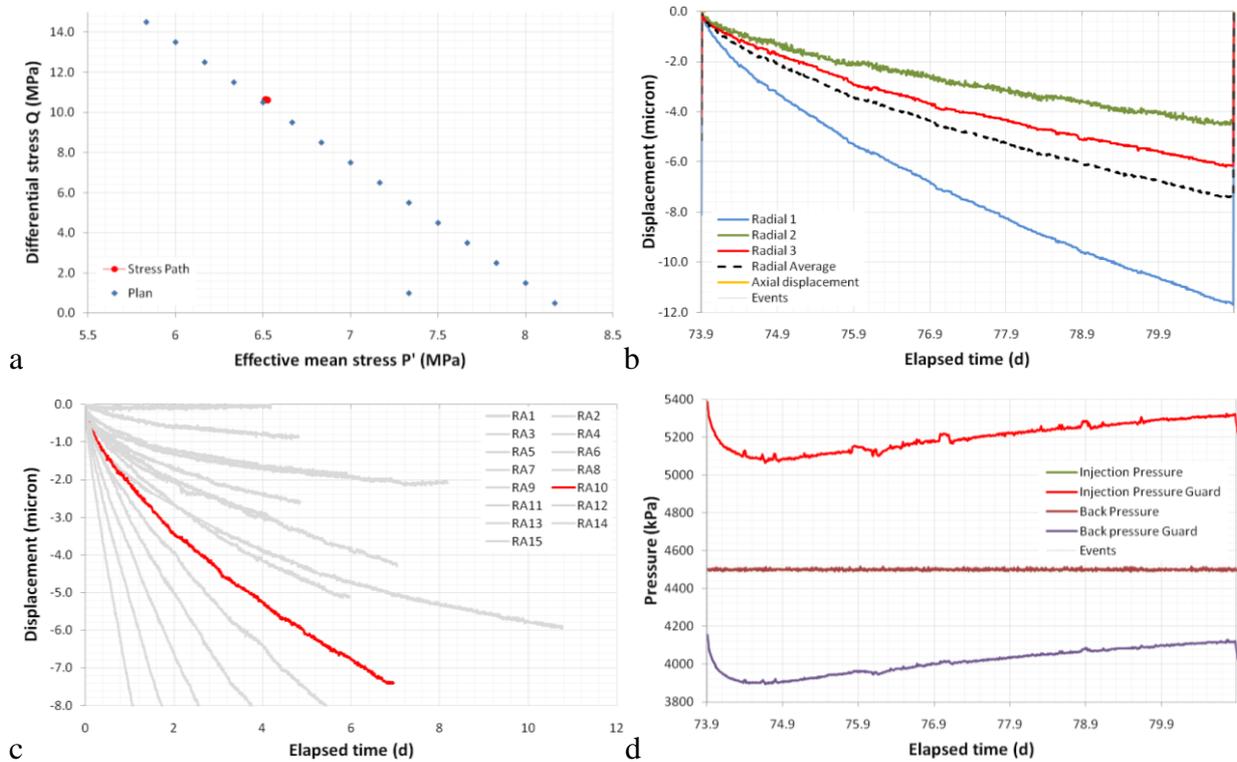
Figure 4-21　　Results for step 11 of test SPP_CoX-1. A). Location of the stress-path. B) Radial displacement results. C) Average radial displacement in comparison to other test steps. D) Evolution of porewater pressure in the guard ring assembly.

4.3.11 Step 12; Day 80.9 – 88.0; σ_1 = 18.5 MPa, $\sigma_{2,3}$ = 7.0 MPa

The twelth stage was approximately 7 days long and the results are shown in Figure 4-22. All channels show similar results to previous steps. Considerable anisotropy is seen in radial displacement with 14.5, 8.1 and 5.5 µm of displacement seen in radial 1, 3 and 2 respectively (Figure 4-22b). Figure 4-22c shows that the curvature of displacement for step 12 has increased in comparison with step 11. The evolution of porewater pressure in the guardrings (Figure 4-22d) shows the characteristic pressure drop followed by pressure recovery. As with previous steps, the porewater pressure had not fully recovered and had not reached asymptote.

4.3.12 Step 13; Day 88.0 – 94.9; σ_1 = 19.0 MPa, $\sigma_{2,3}$ = 6.5 MPa

The thirteenth stage was approximately 7 days long and the results are shown in Figure 4-23. All channels show similar results to previous steps. Considerable anisotropy is seen in radial displacement with 18.5, 10.4 and 8 µm of displacement seen in radial 1, 3 and 2 respectively (Figure 4-23b). Figure 4-23c shows that the curvature of displacement for step 13 has increased in comparison with step 12. The evolution of porewater pressure in the guardrings (Figure 4-23d) shows the characteristic pressure drop followed by pressure recovery. As with previous steps, the porewater pressure had not fully recovered and had not reached asymptote.
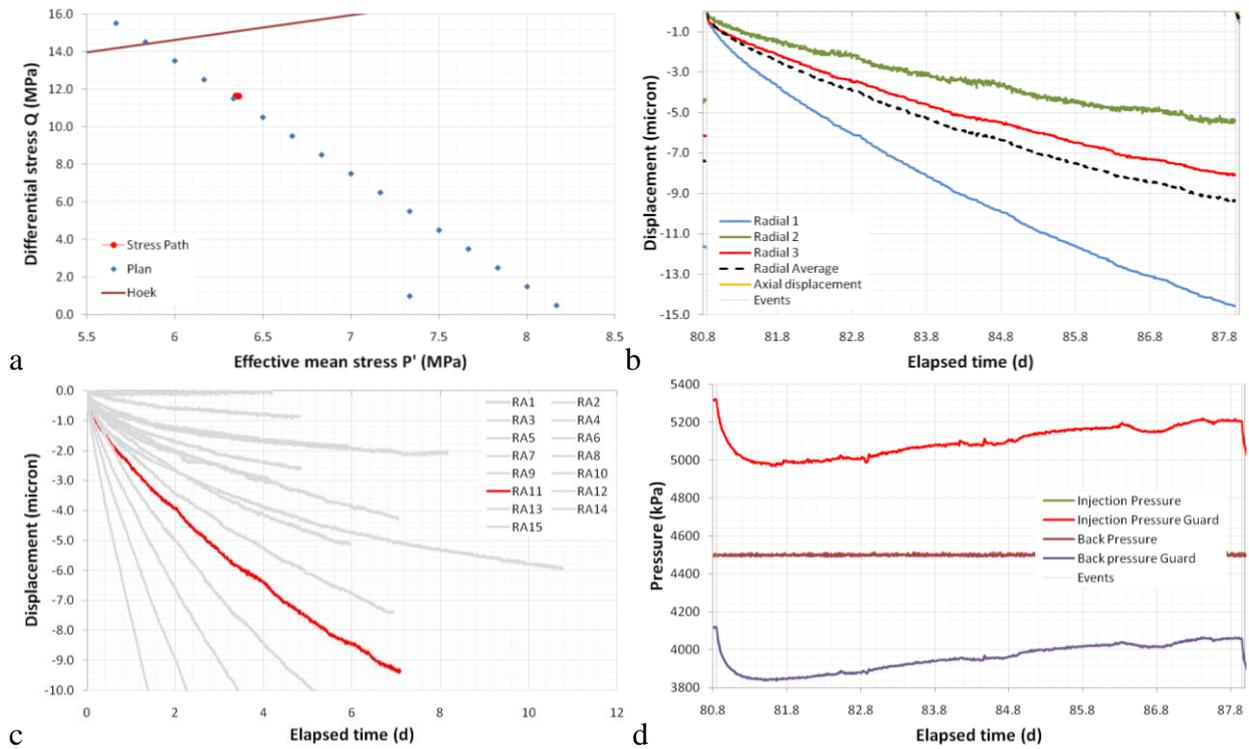
Figure 4-22 Results for step 12 of test SPP_CoX-1. A). Location of the stress-path. B) Radial displacement results. C) Average radial displacement in comparison to other test steps. D) Evolution of porewater pressure in the guard ring assembly.
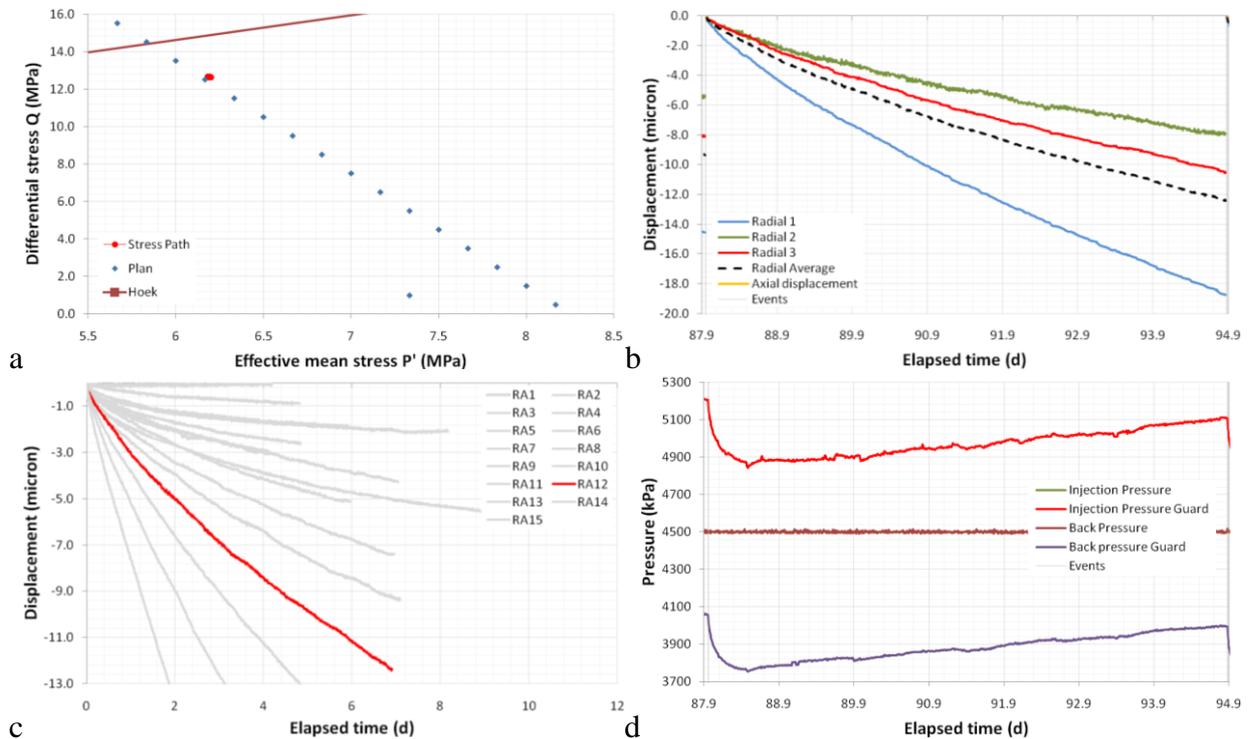
Figure 4-23 Results for step 13 of test SPP_CoX-1. A). Location of the stress-path. B) Radial displacement results. C) Average radial displacement in comparison to other test steps. D) Evolution of porewater pressure in the guard ring assembly.

4.3.13 Step 14; Day 94.9 – 101.9; σ_1 = 19.5 MPa, $\sigma_{2,3}$ = 6.0 MPa

The fourteenth stage was approximately 7 days long and the results are shown in Figure 4-24. All channels show similar results to previous steps. Considerable anisotropy is seen in radial displacement with 25.5, 14.1 and 11 μm of displacement seen in radial 1, 3 and 2 respectively (Figure 4-24b). Figure 4-24c shows that the curvature of displacement for step 14 has increased in comparison with step 13. The evolution of porewater pressure in the guardrings (Figure 4-24d) shows the characteristic pressure drop followed by pressure recovery. As with previous steps, the porewater pressure had not fully recovered and had not reached asymptote.
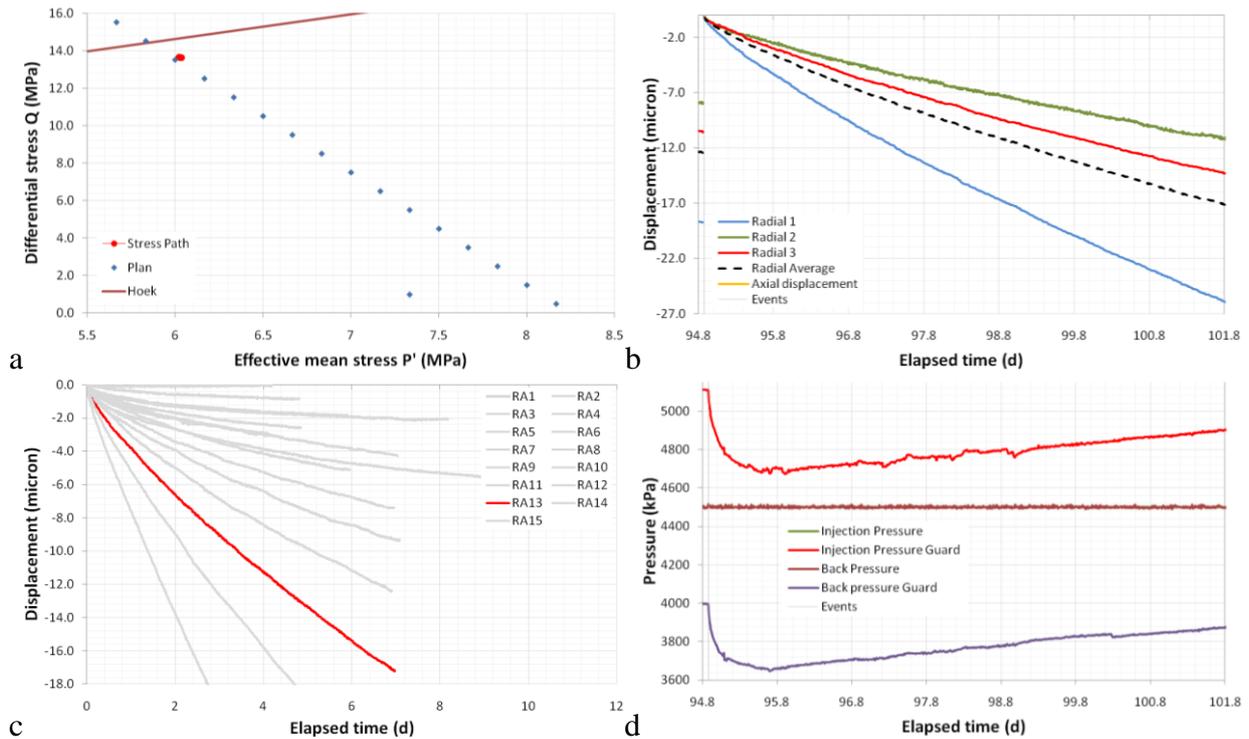
Figure 4-24 Results for step 14 of test SPP_CoX-1. A). Location of the stress-path. B) Radial displacement results. C) Average radial displacement in comparison to other test steps. D) Evolution of porewater pressure in the guard ring assembly.

4.3.14 Step 15; Day 101.9 – 108.9; σ_1 = 20.0 MPa, $\sigma_{2,3}$ = 5.5 MPa

The fifteenth stage was approximately 7 days long and the results are shown in Figure 4-25. All channels show similar results to previous steps. Considerable anisotropy is seen in radial displacement with 36.4, 21.1 and 16.5 μm of displacement seen in radial 1, 3 and 2 respectively and 36 μm of displacement seen in axial displacement (Figure 4-25b). Figure 4-25c shows that the curvature of displacement for step 15 has increased in comparison with step 14. The evolution of porewater pressure in the guardrings (Figure 4-25d) shows the characteristic pressure drop followed by pressure recovery. As with previous steps, the porewater pressure had not fully recovered and had not reached asymptote. After day 107.3 the pressure response in the pressure guard changes characteristic with high frequency oscillations, this may be in response to 0.3° C oscillations observed in the temperature of the pressure vessel. However, the frequency of the pressure oscillations is much higher than that seen in the temperature.
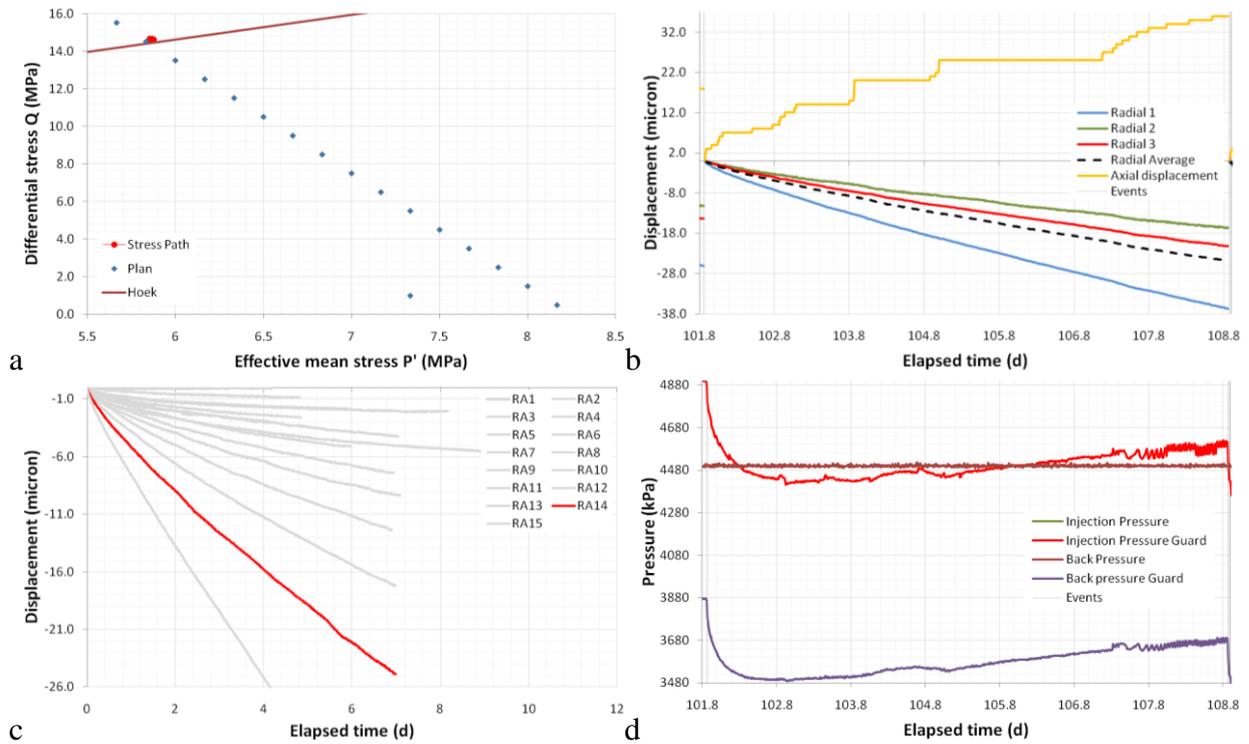
Figure 4-25   Results for step 15 of test SPP_CoX-1. A). Location of the stress-path. B) Axial and radial displacement results. C) Average radial displacement in comparison to other test steps. D) Evolution of porewater pressure in the guard ring assembly.

4.3.15 Step 16; Day 108.9 – 123.2; σ_1 = 20.5 MPa, $\sigma_{2,3}$ = 5.0 MPa

The sixteenth and final stage was approximately 14 days long and the results are shown in Figure 4-26. It can be seen that up to day 114 the deformation response was similar to previous steps. Considerable anisotropy is seen in radial displacement with 43, 31.4 and 21.8 μm of displacement seen in radial 1, 3 and 2 respectively and 64 μm of displacement seen in axial displacement at day 114 (Figure 4-26b). After this time the deformation accellerated and by day 114.5 all displacement sensors had reached their maximum displacement. Figure 4-26c shows that the curvature of displacement for step 16 has increased in comparison with step 15. The evolution of porewater pressure in the guardrings (Figure 4-26) shows the characteristic pressure drop; However this is followed by a plateau in pressure, with pressure reducing as the deformation accellerated. Figure 4-26e shows the response recorded in the injection load cell. As displacement started to accellerate the load increased. At the point of sample failure the load reduced and quickly rose again and reached a peak. At this point the hydraulic ram stopped and the response after this time is the slow reduction of load as a result of creep along the formed fracture.
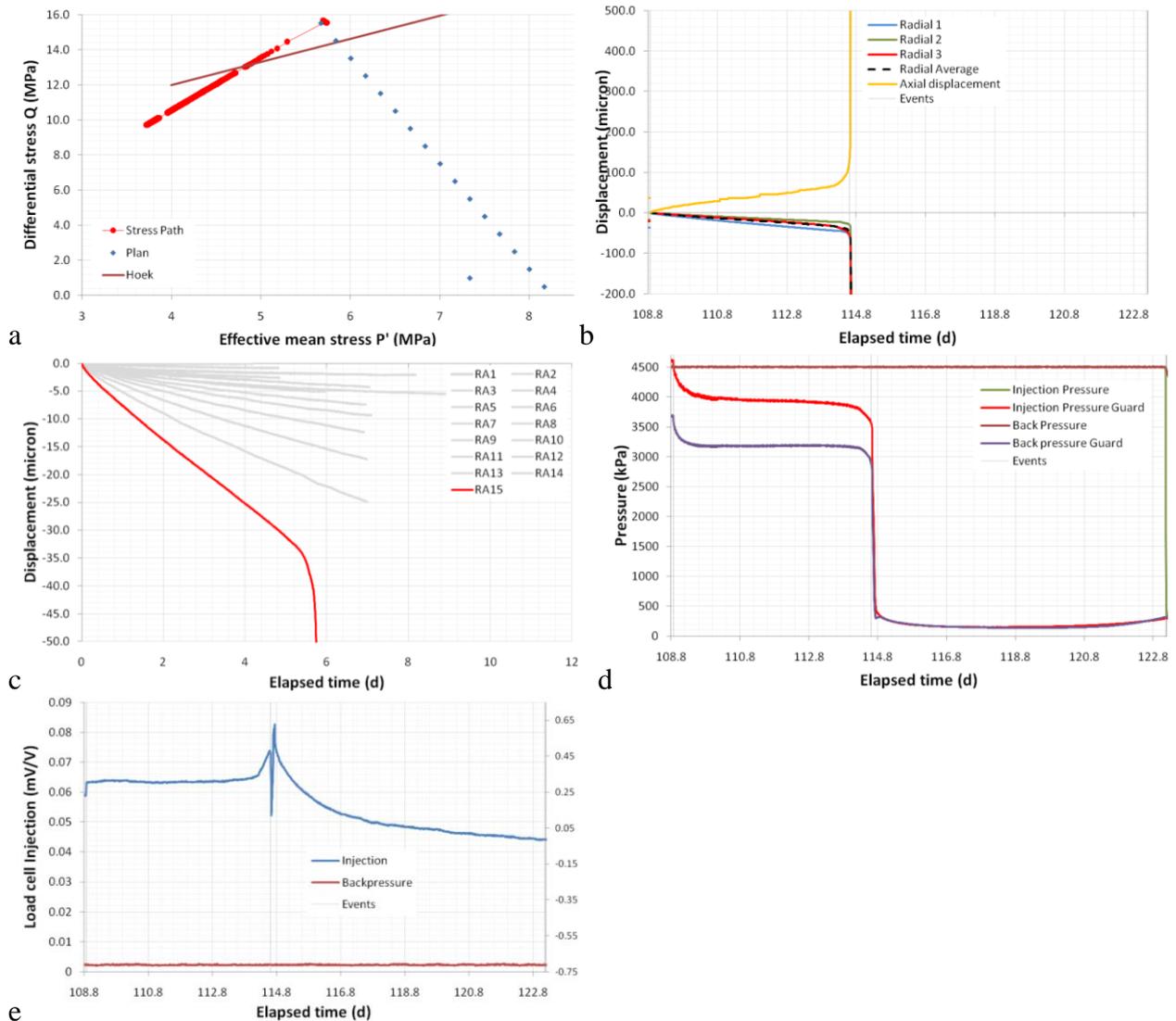
Figure 4-26 Results for step 16 of test SPP_CoX-1. A). Location of the stress-path. B) Axial and radial displacement results. C) Average radial displacement in comparison to other test steps. D) Evolution of porewater pressure in the guard ring assembly. E) Axial load recorded at the end of the test sample during deformation.

4.3.16 Step 16 up to failure; Day 108.9 – 114.6; σ_1 = 20.5 MPa, $\sigma_{2,3}$ = 5.0 MPa

Figure 4-27 shows in detail the 5.5 days of results up unto the point of sample failure for stage 16. Considerable anisotropy is seen in radial displacement with 43, 31.4 and 21.8 μm of displacement seen in radial 1, 3 and 2 respectively (Figure 4-27a) and 64 μm of displacement seen in axial displacement at day 114 (Figure 4-27b). After this time the deformation accellerated; it can be seen that axial displacement showed the first increase in deformation rate, soon followed by radial 3. By day 114.5 all displacement sensors had reached their maximum displacement. The evolution of porewater pressure in the guardrings (Figure 4-27c) shows the characteristic pressure drop; However this is followed by a plateau in pressure, with pressure reducing as the deformation accellerated. Figure 4-27d shows the response recorded in the injection load cell. As displacement started to accellerate the load at this location increased, posibly as a result in the reduction of pore pressure. At the point of sample failure the load reduced and quickly rose again and reached a peak. At this point the hydraulic ram stopped and the response after this time is the slow reduction of load as a result of creep along the formed fracture. Figure 4-27e shows the flows recorded by the pumps. At the onset of deformation the axial and confining pumps can be seen to increase in flow in order to maintain constant axial

55

load and confining pressure. No marked change in flow of pore fluid is seen at either the injection or back-pressure sides.
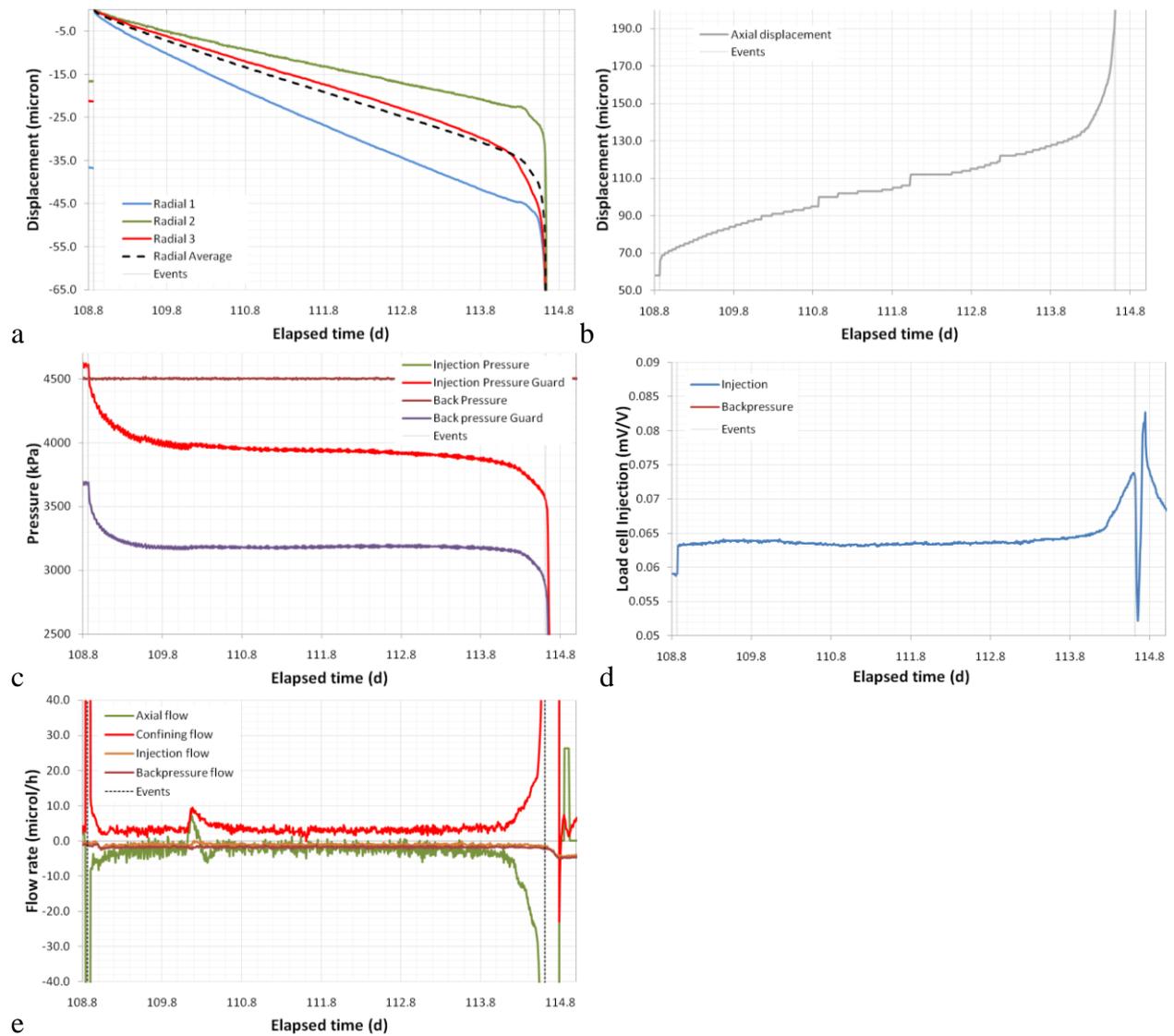
Figure 4-27 Results for step 16 of test SPP_CoX-1 up to the point of sample failure. A). Radial displacement results. B) Axial displacement results. C) Evolution of porewater pressure in the guard ring assembly. E) Axial load recorded at the end of the test sample during deformation.

4.3.17 Step 16 post failure; Day 114.6 – 123.2; σ_1 = 20.5 MPa, $\sigma_{2,3}$ = 5.0 MPa

Considerable changes are seen after sample failure. At the point of failure the axial ram was advanced by the ISCO pump operating at constant pressure. Once the full stroke of the pump had been achieved the axial system stopped and the sample slowly reacted to the constant strain and confining pressure. Pore pressure was continued at constant pressure of 4.5 MPa.

As seen in Figure 4-28a, the axial load on the sample reduced slowly with time from 20.6 MPa to 14.7 MPa over nearly 9 days. This resulted in the stresspath modifying as seen in Figure 4-28b. The slow reduction in load is also shown in the load cell at the injection end of the sample, as seen in Figure 4-28c. This shows that slow creep was occuring. This could possibly be through time-dependent volumetric strain, but is likely to be slow creep along the formed fracture surface. Figure 4-28d shows the change in volume of the confining pressure system and is an indicator of volumetric strain of the sample; suggesting that the sample underwent time-dependent volumetric strain.

Figure 4-28e and f show the change in pore pressure as measured at the guard-rings. The onset of failure saw the pressure at these points reduce and rapidly drop as the sample failed. However, it can be seen that the initial drop of 3-4 MPa was followed by a slow decrease, with a minimum pressure achieved in 2.5 and 5.5 days for the injection and backpressure guard-rings respectively. Unexpectadely it can be seen that pore pressure at the guardring started to rise after reaching minimum. The injection guardring reached a minimum of 145 MPa and recovered to 295 MPa by the end of the experiment. The back-pressure guard ring reached a minimum of 140 MPa and recovered to 325 MPa at the end of the test. Sadly there was not time to continue the experiment, therefore it is not known how much pressure would have recovered. The initial drop in pressure is likely to be the result of the dilatancy created by the fracture/fault running through the sample. The pore fluid at the guardrings drained into this increased porosity network resulting in a reduction in pore pressure. This effect was very localised as there was not a significant increase in flow at the nearby injection and back-pressure filters (Figure 4-28g). The flow into the formed fault zone resulted in a highly anisotropic pore pressure distribution within the sample, which in time started to recover.
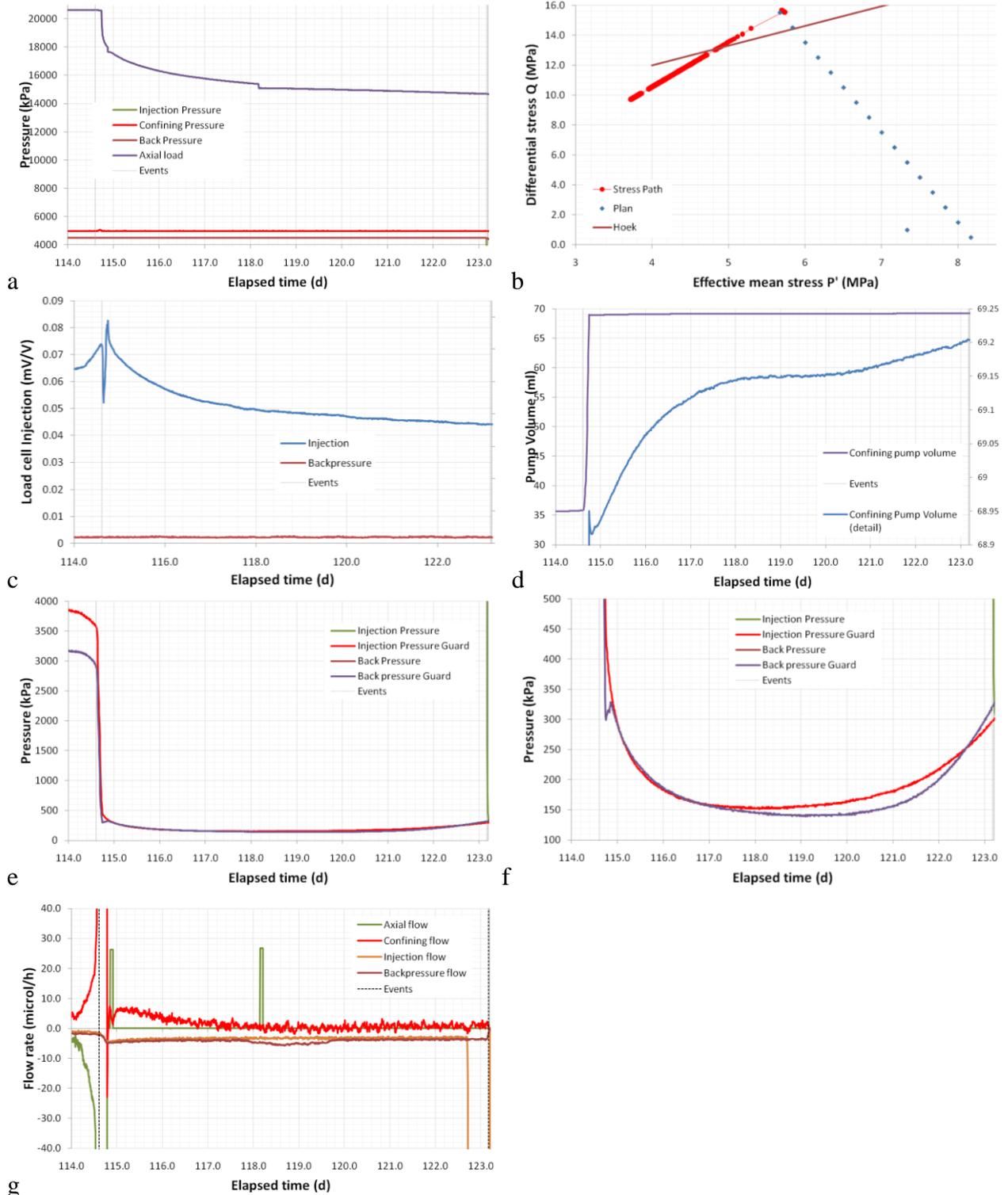
Figure 4-28 Results for step 16 of test SPP_CoX-1 after the sample had failed. A). Axial load on the sample can be seen to reduce once the axial ram had stopped. B). Location of the stress-path. C). Slow reduction in load recorded on the injection platen. D). Change in volume of the confining pressure system suggesting volumetric creep of the sample. E) and F). Pore-pressure measured in guardrings at both end of the samples. G). Flow rate as measured by the four ISCO pumps that operate the SPP.

58

5 Post-test observations

The stress-path permeameter (SPP) apparatus is designed with a 56 mm diameter end that should allow samples to be loaded and removed without the dismantling of the apparatus. However, considerable strain was experienced by the sample and it was not possible to extract the sample from the apparatus without loosening the tie-rods and dismantling the sample. On removing the sample it was evident that the sample had undergone considerable deformation (see Figure 5-1a).

The Hoek sleeve that jackets the test sample within the apparatus did not split and accommodated considerable deformation. The test sample can be seen to have deformed through the formation of a fracture/fault oriented approximately 30° to the length of the sample. It is observed that this fracture appears to intersect both corners of the sample (Figure 5-1b and c) and this may be the result of edge effects created by friction acting along the ends of the sample between rock and steel platten. On closer inspection a series of fractures parallel to the main fracture can be seen, as well as a series of conjugate fractures (see Figure 5-1d). This suggests that the deformation is complex.

The test sample was measured using the BGS built SHRINKiT (Figure 5-2); an apparatus designed to measure soil shrinkage. The apparatus consists of a rotating turntable, on which the test specimen is mounted, and a vertical height gauge, on which a laser rangefinder is mounted. Both are controlled by stepper motors. A third stepper motor operates a release mechanism to allow weighing of the specimen. The system effectively 'scans' the specimen's surface allowing its co-ordinates to be accurately recorded, along with its weight. From this information the volume of the specimen can be determined, the accuracy being a function of the number of points measured. Test specimens in the diameter range 60mm to 100mm and the height range 60mm to 130mm may be tested; however the equipment worked successfully on the 56 mm diameter samples used in this experiment. The apparatus is able to measure up to 3,600 xyz points on the specimen's surface. SHRINKiT works by measuring xyz along the length of the sample, the sample is then rotated and re-measured. For the test sample xyz data was recorded for 25 intervals along the sample length every 3° around the sample circumference. Due to limitations in rotation it is not possible to measure between 354 - 360°. Therefore SHRINKiT was able to measure 3,025 discrete xzy locations on the sample surface. The sample was also weighed by SHRINKiT.

The results from SHRINKiT are output as a text file, which was inported into Microsoft Excel and reformatted so as to plot the circumference of the sample at 25 intervals along the sample length, nine circumferences are shown in Figure 5-3. These plots show that for all 25 intervals the sample had increased in diameter. It is clear to see the fracture that runs through the sample and either side of this feature two circular samples are observed, as expected.
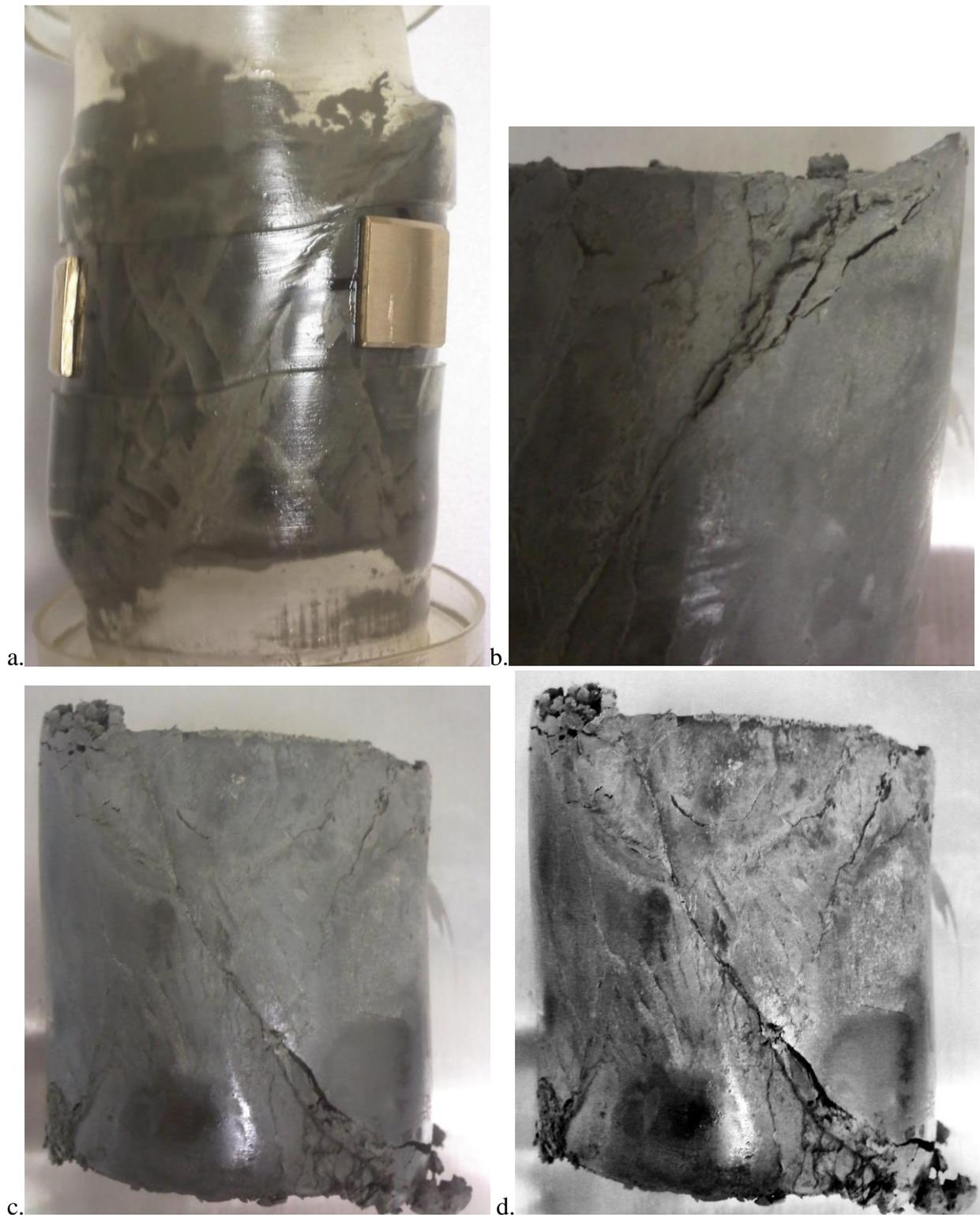
Figure 5-1 Post-test photos of test sample SPP_CoX-1. A). Jacketed sample, showing considerable deformation. B) Detail of the fracture, clearly showing that the formed fracture intersected the corner of the sample. C) Photograph of the entire test sample clearly showing the main fracture surface. D) Enhanced image of photo (c) clearly showing a series of parallel features on the sample surface and a conjugate series of fractures.

Figure 5-2 The automated SHRINKiT, shrinkage limit apparatus.
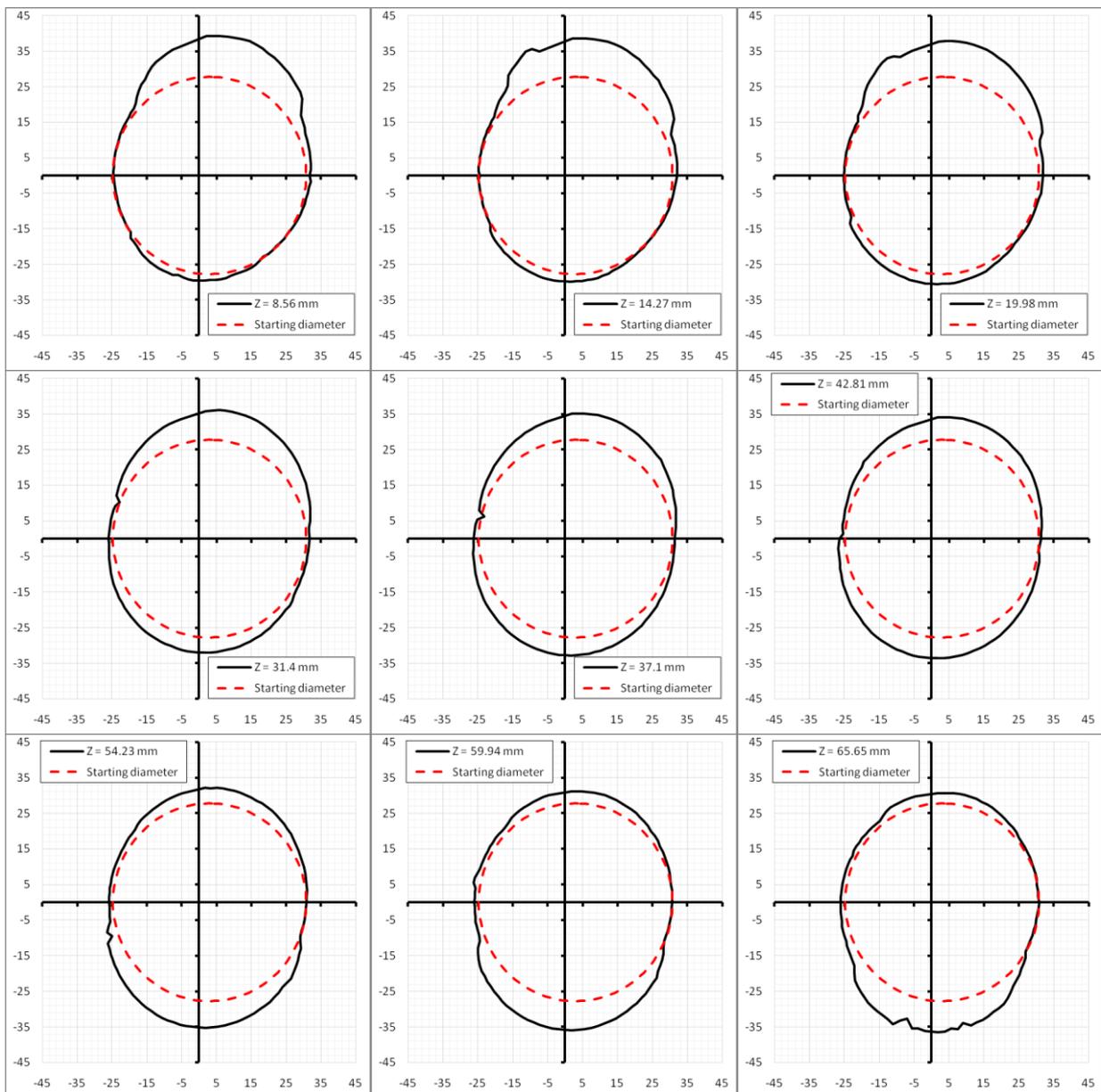
Figure 5-3 Results from Shrinkit giving the dimensions of the final sample at 25 different levels through the sample (9 shown). Elevation of Z = 0 is the top of the sample. These plots clearly show the deformation at each level when compared with the size of the starting material.

6 Discussion

The stress-path permeameter was seen to perform very well during the first test. The radial displacement data has been invaluable in understanding the deformation of the sample during the stress-path history the sample was subjected to.

Many of the observations noted show that the Callovo-Oxfordian claystone is highly time-dependent in its deformation. During the initial stage of the test the sample swelled and the apparatus successfully measured this deformation. During the successive stages the sample deformed quickly to the change in stress state and showed considerable time-dependent creep during all stages of the test. As the test went on the amount of creep observed increased. However, during each step equilibrium had not been achieved so this may be superposition of deformation from stage to stage. This hypothesis is strengthened by the observations of stages three and seven. Stage three achieved equilibrium and the amount of creep observed in stage four are similar. This shows that creep is present in the sample even after equilibrium has been achieved. During stage seven the sample was held constant for a prolonged period of time and as a consequence the following stage (eight) showed less creep. It is possible that a certain component of the observed creep is caused by pore pressure, which due to the low permeability of the sample takes time to homogenise within the sample. A secondary component of creep is caused by the time-dependent deformation (true creep) of the sample.

There are several implications of the observed creep. For the current experimental study it means that each stage of the test has to be conducted to the point of equilibrium. This may lengthen the time each step has to be conducted and may limit the scope of the full experimental programme. The observed creep also places a question as to whether deformation in CoX is rate-dependent. The time-dependency suggests that heterogeneous pore pressure distributions are created in deforming samples and that failure may result at different stress levels. Therefore a test conducted quickly may predict a weaker strength than one conducted slowly. This suggests that care should be taken when comparing data from different sources that have used different apparatus, different sized samples, drained or undrained conditions etc. This may explain why failure occurred at a stress-state higher than that predicted for CoX by the Hoek-Brown failure criterion. It is also interesting that failure occurred 5.5 days into a constant stress-state step. This begs the question whether ultimate failure would have occurred during the previous stage if it had been left longer, although this is unlikely.

The observed behaviour of pore pressure at the guard rings is intriguing. For all stress steps the pore pressure initially drops and within a day or two reaches a minimum. During each step the axial load is increased and the confining pressure is lowered. It is likely that the pore pressure response is showing that dilation is occurring which is causing fluid to flow away from the corners of the sample. Once the pressure minimum has been reached, in all but one of the steps the pressure begins to rise. This suggests that the deformation at first results in fluid moving away from the sample corners and that with time it is drawn back to the corners. This could either be the fluid expelled from the corners returning or pore fluid from the injection point flowing into the now lower-pressure zone. In the early stages of the test (stage 1-7) it was observed that pore pressure generally returned to that seen at the start of the stage. In later stages it was observed that full pressure recovery was not achieved and over time the pore pressure at the guard-rings reduced. This may be the result of the not conducting each step for sufficiently prolonged time, but may also be indicative of permanent damage occurring to the sample. The observations at the guard ring show that pore pressure distribution within the sample is highly complex.

Considerable anisotropy is observed in radial deformation. At all stages it was observed that Radial 1 showed the most deformation, followed by Radial 3 and Radial 2 respectively. This anisotropy will have influenced the formation of the fault in the sample, however the orientation of the fracture was not recorded with respect to the orientation of Radial 1-3.

7 Summary

The bespoke Stress-path permeameter (SPP) has been constructed in order to follow specific stress paths, whilst allowing volumetric deformation to be monitored during deformation. The apparatus was fully calibrated and shown to perform well. This report describes the first test conducted using the SPP, which has given very good results on the deformation characteristics of Callovo–Oxfordian (CoX) claystone. The radial displacement data has been invaluable in understanding the deformation of the sample during the stress-path history the sample was subjected to.

The Callovo-Oxfordian claystone is highly time-dependent in its deformation. During the initial stage of the test the sample swelled and the apparatus successfully measured this deformation. During the successive stages the sample deformed quickly to the change in stress state and showed considerable time-dependent creep during all stages of the test. As the test went on the amount of creep observed increased. However, during each step equilibrium had not been achieved so this may be superposition of deformation from stage to stage. This hypothesis is strengthened by the observations of stages three and seven, which were prolonged stages and were followed in successive steps by a decrease in time dependent deformation. A certain component of the observed creep is caused by pore pressure, which due to the low permeability of the sample takes time to homogenise within the sample. A secondary component of creep is caused by the time-dependent deformation (true creep) of the sample.

There are several implications of the observed creep. For the current experimental study it means that each stage of the test has to be conducted to the point of equilibrium. This may lengthen the time each step has to be conducted and may limit the scope of the full experimental programme. The observed creep also places a question as to whether deformation in CoX is rate-dependent. The time-dependency suggests that heterogeneous pore pressure distributions are created in deforming samples and that failure may result at different stress levels. Therefore a test conducted quickly may predict a weaker strength than one conducted slowly. This suggests that care should be taken when comparing data from different sources that have used different apparatus, different sized samples, drained or undrained conditions etc. This may explain why failure occurred at a stress-state higher than that predicted for CoX by the Hoek-Brown failure criterion. It is also interesting that failure occurred 5.5 days into a constant stress-state step.

The observed behaviour of pore pressure at the guard rings is intriguing. For all stress steps the pore pressure initially drops and within a day or two reaches a minimum. During each step the axial load is increased and the confining pressure is lowered. It is likely that the pore pressure response is showing that dilation is occurring which is causing fluid to flow away from the corners of the sample. Once the pressure minimum has been reached, in all but one of the steps the pressure begins to rise. This suggests that the deformation at first results in fluid moving away from the sample corners and that with time it is drawn back to the corners. This could either be the fluid expelled from the corners returning or pore fluid from the injection point flowing into the now lower-pressure zone. In the early stages of the test (stage 1-7) it was observed that pore pressure generally returned to that seen at the start of the stage. In later stages it was observed that full pressure recovery was not achieved and over time the pore pressure at the guard-rings reduced. This may be the result of the not conducting each step for sufficiently prolonged time, but may also be indicative of permanent damage occurring to the sample. The observations at the guard ring show that pore pressure distribution within the sample is highly complex.

Considerable anisotropy is observed in radial deformation. At all stages it was observed that Radial 1 showed the most deformation, followed by Radial 3 and Radial 2 respectively. This anisotropy will have influenced the formation of the fault in the sample, however the orientation of the fracture was not recorded with respect to the orientation of Radial 1-3.

References

British Geological Survey holds most of the references listed below, and copies may be obtained via the library service subject to copyright legislation (contact libuser@bgs.ac.uk for details). The library catalogue is available at: http://geolib.bgs.ac.uk.

Adams, B.A., and Wulfsohn, D. (1997) Variation of the critical-state boundaries of an agricultural soil. *European Journal of Soil Science*, **48**, pp.739-748.

Anagnostou, G. (1991) *Untersuchungen zur Statik des Tunnelbaus in quellfähigem Gebirge.* Dissertation **No. 9553**. ETH. Zurich, Switzerland.

ANDRA (2005) Dossier 2005 REFERENCTIEL SITE Meuse/Haute-MARNE. TOME 1, 664p.

ANDRA (2005) Dossier 2005 REFERENCTIEL SITE Meuse/Haute-MARNE. TOME 2, 353p.

Aristorenas, G. V. (1992) *Time-dependent behaviour of tunnels excavated in shale*. PhD Thesis. Massachusetts Institute of Technology. Boston, USA.

Atkinson, J.H. and Bransby, P.L. (1978) *The Mechanics of Soils: An Introduction to Critical State Soil Mechanics*. McGraw-Hill, New York.

Barla, M. (1999) *Tunnels in swelling ground: Simulation of 3-D triaxial tests by triaxial laboratory testing*. PhD Thesis, Technical University of Turin, Italy, 179p.

Barla, G. and Barla, M. (2001) Investigation and modelling of the Brenva Glacier rock avalanche on the Mount Blanc Range. *ISRM Regional Symposium Eurock 2001*, Balkema, Rotterdam, Espoo, Finlandia, 3-7 giugno, 2001

Barla, G. (2001) *Tunnelling under squeezing rock conditions*. Eurosummer-School in Tunnel Mechanics, Innsbruck, 2001. pp.98

Bellwald, P. (1990) *A contribution to the design of tunnels in argillaceous rock*. PhD Thesis. Massachusetts Institute of technology. Boston, USA.

Bonini, M. Barla, M. and Barla, G. (2001) Flac applications to the analysis of swelling behaviour in tunnels. *2nd Flac Symposium on Numerical Modeling in Geomechanics, Lione, 29-31 ottobre, 2001*

Byerlee, J.D. (1967) Frictional characteristics of granite under high confining pressure. *Journal of Geophysical Research*, **72**, pp. 3639-3648.

Cotecchia, F., and Chandler, R.J. (2000) A general framework for the mechanical behaviour of clays. *Géotechnique*, **50**, pp. 431-447.

Cuss, R.J., Rutter, E.H., and Holloway, R.F. (2003[a]) Experimental Observations of the Mechanics of Borehole Deformation in Sandstone. *International Journal of Rock Mechanics and Mining Sciences*, **40**, pp. 747-761.

Cuss, R.J., Rutter, E.H., and Holloway, R.F. (2003[b]) The Application of Critical State Soil Mechanics to the Mechanical Behaviour of Sandstone. *International Journal of Rock Mechanics and Mining Sciences*, **40**, pp. 847-862.

Cuss, R.J. (1999) *An experimental investigation of the mechanical behaviour of sandstones with reference to borehole stability*. Ph.D. thesis, Manchester, UK, University of Manchester.

David, C., Wong, T.F., Zhu, W., and Zhang, J. (1994) Laboratory measurement of compaction-induced permeability change in porous rocks; implications for the generation and maintenance of pore pressure excess in the crust. *Pure and Applied Geophysics,* **143**, pp. 425-456.

Dewhurst, D.N., Aplin, A.C., and Sarda, J.-P. (1999) Influence of clay fraction on pore-scale properties and hydraulic conductivity of experimentally compacted mudstones. *Journal of Geophysical Research*, **104**, pp. 29,261-29,274.

Dewhurst, D.N., Yang, Y., and Aplin, A.C. (1999) Permeability and fluid flow in natural mudstones. In: Aplin, A.C., Fleet, A.J., and Macquaker, J.H.S., eds., *Mud and Mudstones: Physical and Fluid Flow Properties*, Geological Society of London, Special Publications, **158**, pp. 23-43.

Diaz-Rodriguez, J.A., Leroueil, S., and Aleman, J.D. (1992) On yielding of Mexico City clay and other natural clays. *Journal of Geotechnical Engineering American Society of Civil Engineers*, **118**, pp. 481-495.

DiMaggio, F.L., and Sandler, I.S. (1971) Material model for granular soils. *Journal of Engineering Mechanics Division, American Society of Civil Engineers*, **97**, pp. 935-950.

Esteban, L., Bouchez, J., L. and Trouiller, A. (2006) The Callovo-Oxfordian argillites from the eastern Paris Basin: Magnetic data and petrofabrics, *Comptes Rendus Geosciences* **338**, pp 867-881

Gaucher, E., Robelin, C., Matray, J.-M., Négrel, G., Gros, Y., Heitz, J.-F., Vinsot, A., Rebours, H., Cassagnabère, A. and Bouche, A.T. (2004) ANDRA underground research laboratory: interpretation of the mineralogical and

geochemical data acquired in the Callovo-Oxfordian formation by investigative drilling, *Phys. Chem. Earth* **29**, pp. 55–77.

Geogiannopoulos, N.G., and Brown, E.T. (1978) The critical state concept applied to rock. *International Journal of Rock Mechanics and Mining Sciences and Geomechanics Abstracts*, **15**, pp. 1-10.

Harrington, J.F., and Noy, D.J. (2010) Gas and water flow in the Callovo-Oxfordian argillite: Progress 2010. *British Geological Survey Commissioned Report*, CR/10/101. 50pp.

Heiland, J. (2003[a]) Laboratory testing of coupled hydro-mechanical processes during rock deformation. *Hydrogeology Journal*, **11**, pp.122-141.

Hoek, E., and Brown, E.T. (1980) Empirical strength criterion for rock masses: *Journal of the Geotechnical Engineering Division*, **106**, pp. 1013-1036.

Holt RM (1990) Permeability reduction induced by a non-hydrostatic stress field. *SPE Formation Evaluation*, **Dec 1990**, pp. 444–448

Horseman, S.T., Harrington, J.F., Birchall, D.J., Noy, D.J. and **Cuss, R.J.** (2005). Consolidation and rebound properties of Opalinus clay: A long-term, fully-drained test. *British Geological Survey Commissioned Report*. **CR/05/128.** 60 pp (Commercial - In Confidence).

Hudson, J.A., and Harrison, J.P. (1997) *Enginerring rock mechanics: an introduction to the principles*. Oxford, Elsevier Science Ltd.

ITASCA Inc. (1996) *FLAC 3D Fast Lagrangian Analysis of Continua.* Version 1.1, User's manual.

Jones, M.E., Leddra, M.J., and Addis, M.A. (1987) Reservoir Compaction and Sea Floor Subsidence due to Hydrocarbon Extraction. *Offshore Technology Report* **OTH 87 276**, HMSO, London

Jones, M.E. (1994) Mechanical principles of sediment deformation. In: Maltman, A., ed., *The geological deformation of sediments*. London, Chapman and Hall, pp. 37-71.

Katsube, T.J., Boitnott, G.N., Lindsay, P.J., and Williamson, M. (1996) Pore structure evolution of compacting muds from the seafloor, offshore Nova Scotia. In: Anonymous, ed., Eastern Canada and national and general programs. *Current Research - Geological Survey of Canada,* pp. 17-26.

Katsube, T.J., Issler, D.R., and Coyner, K. (1996) Petrophysical characteristics of shale from the Beaufort-Mackenzie Basin, northern Canada; permeability, formation factor, and porosity versus pressure, Interior plains and Arctic Canada. *Current Research - Geological Survey of Canada*. pp. 45-50.

Katsube, T.J. (2000) Shale permeability and pore-structure evolution characteristics. *Geological Survey of Canada*. Ottawa, ON, Canada. Pages: 9.

Keaney, G.M.J., Meredith, P.G., and Murrell, S.A.F. (1998) Laboratory study of permeability evolution in a 'tight' sandstone under non-hydrostatic stress conditions. *Rock Mechanics in Petroleum Engineering*, **1** 8-10 July 1998, Trondheim, Norway, Society of Petroleum Engineers, SPE/ISRM 47265, pp. 329-335.

Kirby, J.M., and O'Sullivan, M.F. (1997) Critical state soil mechanics analysis of the constant cell volume triaxial test. *European Journal of Soil Science*, **48**, pp. 71-78.

Kirby, J.M. (1994) Simulating soil deformation using a critical-state model; I, Laboratory tests. *European Journal of Soil Science*, **45**, pp. 239-248.

Kwon, O., Kronenberg, A.K., Gangi, A.F., and Johnson, B. (2001) Permeability of Wilcox Shale and its effective pressure law. *Journal of Geophysical Research, B, Solid Earth and Planets,* **106**, pp. 19,339-19,353.

Leddra, M.J., Jones, M.E., and Goldsmith, A.S. (1993) Compaction and shear deformation of a weakly-cemented, high porosity sedimentary rock. In: Moon, C.F., ed., *The Engineering Geology of Weak Rock*., **8**: Engineering Geology Special Publication, Geological Society of London, pp. 45-54.

Leddra, M.J., Petley, D.N., and Jones, M.E. (1992) Fabric changes induced in a cemented shale through consolidation and shear. In: Tillerson, J.R. and Wawersik, W.R. eds, *Rock Mechanics, Proceedings of the 33rd U.S. Symposium*, Balkema, Rotterdam.

Loe, N.K., Leddra, N.M., and Jones, M.E. (1992) Strain states during stress path testing of the Chalk. In: *Rock Mechanics. Proceedings of the 33rd U.S. Symposium*, Tillerson, J.R. and Wawersik, W.R.W. (eds.), A.A. Balkema, Rotterdam, pp.927-936.

Maâtouk, A., Leroueil, S., and La Rochelle, P. (1995) Yielding and critical state of a collapsible unsaturated silty soil. *Géotechnique*, **45**, pp. 465-477.

Maltman, A. (1994) *The geological deformation of sediments*. London, United Kingdom, Chapman and Hall, 362 pp.

McLintock, F.A., and Walsh, J.B. (1962) Friction on Griffith cracks in rock under pressure. *Proceedings of the 4th US National Congress on Application Mechanics*, New York.

Menéndez, B., Zhu, W., and Wong, T.F. (1996) Micromechanics of brittle faulting and cataclastic flow in Berea Sandstone. *Journal of Structural Geology*, **18**, pp. 1-16.

Mitchell, R.J. (1970) On the yielding and mechanical strength of Leda clays. *Canadian Geotechnical Journal*, **7**, pp. 297-312.

Morrow, C., Shi, L.Q., and Byerlee, J.D. (1984) Permeability of fault gouge under confining pressure and shear stress. *Journal of Geophysics Research*, **89**, pp. 3193-3200.

Neuzil, C.E., Bredehoeft, J.D. and Wolff, R.G. (1984) Leakage and fracture permeability in the Cretaceous shales confining the Dakota aquifer in South Dakota. In: *Proceedings of First C.V. Theis Conference on Geohydrology* in Dublin, Ohio. Jorgensen, D.G. and Signor, D.C. (eds.). National Water Well Association. pp.113-120.

Ng, R.M.C., and Lo, K.Y. (1985) The measurements of soil parameters relevant to tunnelling in clays. *Canadian Geotechnical Journal,* **22**, pp. 375-391.

Ohnaka, M. (1973) The quantitive effect of hydrostatic confining pressure on the compressive strength of crystalline rocks. *J. Phys. Earth*, **21**, pp. 125-140.

Petley, D.N. (1999) Failure envelopes of mudrocks at high confining pressures, in Macquaker Joe, H.S., ed., *Muds and mudstone; physical and fluid-flow properties*, **158**: Geological Society Special Publications London, United Kingdom, Geological Society of London, pp. 61-71.

Petley, D.N., Jones, M.E., Leddra, M.J., and Loe, N.K. (1992) On changes in fabric and pore geometry due to compaction and shear deformation of weak North Sea sedimentary rocks. *North Sea Oil and Gas Reservoirs III*. London, Graham and Trotman.

Remvik, F., and Skalle, P. (1993) Shale-fluid interaction under simulated downhole conditions, and its effect on borehole stability, in Haimson, B.C., ed., *Rock mechanics in the 1990s*., **30**; 7: *International Journal of Rock Mechanics and Mining Sciences and Geomechanics Abstracts* Oxford-New York, International, Pergamon, pp. 1115-1118.

Rocscience (1998) Examine3D, *User's Manual*. Rocsicence Inc. Univesity of Toronto

Roscoe, K.H. and Burland, J.B. (1968) On the generalised stress-strain behaviour of "wet" clay. In: *Engineering Plasticity*. Heyman, J. and Leckie, F.A. (eds.). Cambridge University Press. pp.535-609.

Roscoe, K.H., Schofield, A., and Wroth, C.P. (1958) On the yielding of soils. *Géotechnique*, **8**, pp. 22-53.

Rouseset, D. and Clauer, N. (2003) Discrete Clay Diagenesis in a Very Low-Permeable Sequence Constrained by an Isotopic (K-Ar and Rb-Sr) Study, *Contributions to Mineralogy and Petrology*, **145**, pp 182-198.

Schofield, A., and Wroth, C.P. (1968) *Critical State Soil Mechanics.* London, McGraw-Hill, 310 pp.

Schofield, A. (1998) Mohr Coulomb error correction. *Ground Engineering*, **31**, pp. 30-32.

Schutjens, P.M.T.M. and de Ruig, H. (1997) The influence of stress path on compressibility and permeability of an overpressurised reservoir sandstone: some experimental data. *Phys Chem Earth,* **22,** pp. 97–103

Shah, K. (1997) An elasto-plastic constitutive model for brittle-ductile transition in porous rocks. *Proceedings of the 29th Symposium on Fatigue and Fracture Mechanics*, ASTM, Standford, California, June 1997.

Steiner, W. (1992) Swelling rocks in tunnels: characterisation and effect of horizontal stresses. *Eurock '92*. pp. 163-168. Thomas Telford. London, U.K.

Tavenas, F., and Leroueil, S. (1977) Effects of stresses and time on yielding of clays . *Proceedings of the 9th International Conference on Soil Mechanics*, Tokyo, 1977.

Vaughan, P.R. (1985) Mechanical and hydraulic properties of in situ residual soils. *First International Conference in Geomechanics of Tropical and Saprolitic Soils*, Brasilia, Brasil.

Walsh, J.B., and Brace, W.F. (1984) The effect of pressure on porosity and the transport properties of rock. *Journal of Geophysical Research. B*, **89**, pp. 9425-9431.

Wenk, H.-R., Voltolini, M., Mazurek, M., Van Loon, L.R. and Vinsot, A. (2008) Preferred Orientations and Anisotropy in Shales: Callovo-Oxfordian Shale (France) and Opalinus Caly (Switzerland), *Clays and Clay Minerals*, **56**, pp 285-306.

Wheeler, S.J., and Sivakumar, V. (1995) An elasto-plastic critical state framework for unsaturated soil. *Géotechnique*, **45**, pp. 35-53.

Wileveau, Y., and Bernier, F. (2008) Similarities in the hydromechanical response of Callovo-Oxfordian clay and Boom Clay during gallery excavation. Physics and Chemistry of the Earth, 33, S343–S349.

Wong, T.-f., David, C., and Zhu, W. (1997) The transition from brittle faulting to cataclastic flow in porous sandstones; mechanical deformation. *Journal of Geophysical Research, B, Solid Earth and Planets*, **102**, pp. 3009-3025.

Zhang, C-L, Rothfuchs, T., Su, K., and Hoteit, N. (2007) Experimental study of the thermo-hydro-mechanical behaviour of indurated clays. *Physics and Chemistry of the Earth*, 32, 957–965.

Zhu, W., and Wong, T.-f. (1997[a]) Shear-enhanced compaction in sandstone under nominally dry and water-saturated conditions. In: Kim, K., ed., *ISRM international symposium, NY Rocks '97. International Journal of Rock Mechanics and Mining Sciences and Geomechanics Abstracts*, **34**, pp. 372.

Zhu, W., and Wong, T.-f. (1997[b]) The transition from brittle faulting to cataclastic flow; permeability evolution. *Journal of Geophysical Research*, *B, Solid Earth and Planets*, **102**, pp. 3027-3041.

Zhu, W., and Wong, T.f. (1994) Permeability evolution related to the brittle-ductile transition in Berea Sandstone. In: Anonymous, ed., *AGU 1994 fall meeting.*, **75; 44 Suppl.**: *Eos*, Transactions, American Geophysical Union. pp. 638.

Zhu, W., Montesi, L.G.J., and Wong, T.-f. (1997) Shear-enhanced compaction and permeability reduction: Triaxial extension tests on porous sandstone. *Mechanics of Materials*, **25**, pp. 199-214.

Zoback, M.D., and Byerlee, J.D. (1975) The effect of microcrack dilatancy on the permeability of Westerly Granite. *Journal of Geophysics Research*, **80**, pp. 752-755.